GAS PHASE SPECTROSCOPY AND COMPUTATIONAL QUANTUM CHEMISTRY OF URANIUM-CONTAINING CATIONS

by

JOSHUA H. MARKS

(Under the Direction of Michael A. Duncan)

ABSTRACT

Uranium containing clusters $U_nO_m^+$ and complexes $U^+(N_2)_n$ are produced in a molecular beam via laser vaporization in a pulsed supersonic expansion. Mass–selected cations are investigated using fixed frequency photodissociation with 355 and 532 nm Nd:YAG harmonics. The most stable structures and stoichiometries are formed as fragment ions during photodissociation. Infrared photodissociation spectra of $U^+(N_2)_n$ are measured with a tunable infrared OPO/OPA. Density functional theory is used to investigate those masses found to be most stable. Computational predictions of infrared spectra are compared to experimental data. Uranium oxide clusters were found to fragment to $UO_2^+(UO_3)_n$ regardless of the identity of the ion photodissociated. Additional fragment cations $(UO_3)_n^+$ are produced only from cluster cations $(UO_3)_n^+$ indicate the stability of the neutral $(UO_3)_n$ cluster or n(UO_3) eliminated. The complex $U^+(N_2)_8$ was found to be a fully coordinated cube. Photodissociation of $U^+(N_2)_n$ with 355 and 532 nm light produced a regular ratio of photon energy to the number of ligands eliminated. This was used to estimate a $U^+–N_2$ bond dissociation energy of 12.1 ± 1.3 kcal/mol, which was found not to vary significantly with complex size. DFT calculations are in good agreement with this bond energy and were able to accurately predict infrared spectra of $U^+(N_2)_8$

and other fully coordinated uranium cation complexes. However, agreement between experiment and theory was found to become poorer as complex size is reduced from n = 8 to 3.

INDEX WORDS: Laser Vaporization, Infrared Spectroscopy, Gas Phase Spectroscopy
Uranium, Quantum Chemistry

GAS PHASE SPECTROSCOPY AND COMPUTATIONAL QUANTUM CHEMISTRY OF URANIUM-CONTAINING CATIONS

by

JOSHUA H. MARKS

B.S., The University of Hartford, 2010

A Dissertation Submitted to the Graduate Faculty of The University of Georgia in Partial Fulfillment of the Requirements for the Degree

DOCTOR OF PHILOSOPHY

ATHENS, GEORGIA

2021

GAS PHASE SPECTROSCOPY AND COMPUTATIONAL QUANTUM CHEMISTRY OF URANIUM-CONTAINING CATIONS

By

JOSHUA H. MARKS

Major Professor: Michael A. Duncan

Committee: Gary E. Douberly
Geoffrey D. Smith

Electronic Version Approved:

Ron Walcott
Dean of the Graduate School
The University of Georgia
May 2021

TABLE OF CONTENTS

CHAPTER 1

INTRODUCTION AND REVIEW

The earliest substantial effort to study the chemistry of the actinide elements was during the Manhattan Project.[1–5] This resulted in the production of the first nuclear power sources, atomic bombs, and hundreds of millions of gallons of so–called radioactive sludge. This waste material is stored to this day, together with that generated by all nuclear reactors since. The environmental impact and remediation of this waste motivates research into the chemistry of actinide elements.[6–14] The use of actinides as nuclear fuel requires research into their unique chemical properties.[15–18] These metals are also the only known elements that have f orbitals that extend sufficiently to participate in bonding, leading to a great deal of interest in the field of actinide synthesis.[19–35] This leads to unique chemistry that is not possible for any other elements, such as the formation of complexes like the η^8 actinocene complexes. The relatively low radioactivity of thorium and depleted uranium allow for their safe use in laboratory research. The unique catalytic and reactive properties of these two elements are areas of active research with mass spectrometry.[36–62] Spectroscopy on ions containing these elements is practically unexplored compared to what is known about the transition metals.[56–113] Safety is not a concern for computational treatment of these molecules and is duly a popular method of study.[114–142] High quality gas–phase spectroscopy is necessary for benchmarking theory but has been applied to fewer than two dozen systems.[87–113] This dissertation presents the gas phase chemistry, mass spectrometry, and spectroscopy of uranium bearing cations.

The participation of f orbitals in chemistry is unique to the early actinides. The lanthanides contain partially occupied valence f orbitals, but their relatively small radius relative to the d orbitals hinders their participation in chemical bonding. The same is true of the late actinides. The elements with atomic number 94, plutonium, and larger all exhibit contraction of the f orbitals below the d orbitals in both spatial extent and relative energy.[40] This results in 23 elements that behave roughly the same as a trivalent transition metal such as scandium. The only f–block elements that have f orbitals that participate in chemical bonding are actinium, thorium, protactinium, uranium, and neptunium. Of these only thorium and uranium are abundant and can be worked with safely. The chemistry and catalytic properties of molecules containing uranium and thorium have been the subject of condensed phase synthesis and spectroscopy research.[19–35] The gas–phase chemistry of these molecules has also been investigated with mass spectrometry.[36–62] Spectroscopic study of molecules containing uranium and thorium has largely been accomplished with matrix isolation or gas–phase electronic spectroscopy of ions.[63–100] A small number of infrared spectra have been published of ions.[102–120]

Early research by Schwarz and coworkers showed the remarkable reactivity of uranium ions.[36] Uranium cation was found to cyclotrimerize three ethylene molecules to form benzene in a collision induced dissociation (CID) experiment. Tandem mass spectrometry experiments by Gibson and coworkers have investigated the gas–phase reactions of actinide ions with oxygen and various organic molecules.[38–50] CID mass spectrometry experiments by Armentrout and coworker have studied the bond strength and reactivities of thorium and uranium carbides, nitrides, and oxides.[56–60] This research has found that the actinide–carbon, nitrogen, and oxygen bonds are largely ionic in nature, though the degree of covalency is a matter of active research.

Infrared spectroscopy in matrix isolation has been conducted by Andrews.[63–78] It has been shown that in a cryogenic matrix uranyl coordinates to five noble gas ligands in a pentagonal bipyramid structure.[65,69–71] Electronic spectroscopy of small actinide containing molecules has been measured by and Wang and coworkers.[81–86] Related photoelectron spectroscopy on diatomic and triatomic actinide containing molecules has been conducted by Heaven and coworkers.[87–100] The large number of excited states possible for these molecules hampers assignment of electronic and photoelectron spectra except in the cases of molecules with closed shell singlet electronic structures, such as uranyl. Gas–phase infrared spectra obtained by van Stipdonk, Oomens, Gibson, and coworkers represent the majority of such data published.[102–111] The complexation and solvation of the ubiquitous uranyl complex has been the major focus of these researchers. The low resolution of the spectra obtained with a free electron laser limits the accuracy with which the structure of the studied molecules can be determined.

Given their radioactivity and toxicity, computational quantum chemistry is a much safer and popular method of studying the chemistry of actinides.[121–144] Computational treatment of actinides is challenging due to their high mass, nuclear charge, and number of electrons. Relativistic effects and spin–orbit coupling are stronger in actinides than lighter elements. Further challenges are posed by the presence of partially occupied f orbitals which result in multireference electronic states. Numerical grid integration error is introduced by the convoluted shape of the f orbitals. The reliability of density functional theory (DFT) has been the subject of intense debate; this is of particular interest in transition metal complexes. The difficulties posed by partially occupied d and f orbitals are similar, and DFT has been found to perform well for transition metal complexes and clusters under certain conditions. In the case of mildly

multireference electronic states DFT is expected to outperform single reference ab initio quantum chemistry in both accuracy and computational cost.[114,115,117–119]

One approach to the computational treatment of actinides is to incorporate the effects of relativity, spin–orbit coupling, and multireference electronic states into the Hamiltonian.[125,130,132,133,139,143,144] The resulting calculations use a variety of relativistic all–electron Hamiltonians such as the Douglas–Kroll–Hess Hamiltonian in combination with multireference methods with complete active space multiconfiguration SCF (CASSCF). Such calculations are too expensive to apply to molecules containing more than two or three atoms. Research by Dixon and coworkers,[118] Peterson and coworkers,[57,59,85,96,99,100,116,141] and Gagliardi and coworkers[74–77,91,132,133,143,144] use these methods to examine the electronic structure of actinides. This research has also helped confirm the closed–shell ionic nature of uranyl and its isoelectronic uranium dinitride.

A variety of approximations are used to apply quantum chemistry to larger systems. Effective core potentials (ECP), also known as a pseudopotentials (PP), replace 30 to 60 core electrons with a single, highly detailed, and fictitious orbital computed to include relativistic effects implicitly. This speeds up calculations substantially but introduces correlation error between the core and valence electrons. The core electrons are the most strongly affected by relativistic effects. Calculations including ECPs do not need to treat relativistic effects explicitly, which speeds up calculations at the cost of accuracy. High field spin–orbit coupling is better described as spin–spin coupling due to interactions of spin states with differing multiplicity. The effects of angular momentum coupling can be treated with expensive multiconfigurational methods such as CASSCF but are neglected for larger molecules where such a calculation is intractable. Researchers such as Dolg and Cao have recently produced new

ECPs that offer an improvement in accuracy for low–cost calculations.[128,129] These methods have been used to examine larger molecules with multiple ligands coordinated to an actinide or actinyl ion. [125–127]

A better understanding of the fundamental chemistry of actinides is the primary motivation behind research presented in this dissertation. There is a lack of experimental data that can be used to verify the result of quantum chemistry calculations. Fixed–frequency photodissociation of uranium oxide cluster cations is used to determine the most stable stoichiometric ratios. The molecular formulas determined to result in stable clusters with mass spectrometry are examined with theory to investigate their likely structure.[62] In a second experiment the chemistry of U^+ with N_2 is explored with fixed–frequency photodissociation at a variety of wavelengths. Infrared spectra of the observed $U^+(N_2)_n$ complexes are compared to predicted spectra to yield insight into the structure of these molecules and to evaluate the performance of commonly used computational methods.

REFERENCES

1. Katz. J. J.; Rabinowitch, E. *The Chemistry of Uranium the Element, Its Binary and Related Compounds*, Dover Publications, Inc.: New York, **1961**.
2. Katz. J. J.; Seaborg, G. T.; Morss, L. R. *The Chemistry of the Actinide Elements, 2nd ed*, Chapman and Hall: London, **1986**.
3. Aspinall, H. C. *Chemistry of the f–Block Elements*, Gordon and Breach: Amsterdam, **2001**.

4. Konings, R. J. M.; Morss, L. R.; Fuger. J. *The Chemistry of the Actinide and Transactinide Elements, 3rd ed.,* edited by L. R. Morss, N. M. Edelstein, and J. Fuger Springer: Dordrecht, **2006**.

5. Cotton, S. *Lanthanide and Actinide Chemistry*, John Wiley & Sons, Ltd.: Chichester, **2006**.

6. Lottermoser, B. *Mine Wastes: Characterization, Treatment and Environmental Impact*, Springer: London, **2007**.

7. Morris, D. E.; Allen, P. G.; Berg. J. M.; Chisholm–Brause, C. J.; Conradson, S. D.; Donohoe, R. J.; Hess, N. J.; Musgrave. J. A.; Tait, C. D. Speciation of Uranium in Fernald Soils by Molecular Spectroscopic Methods: Characterization of Untreated Soils. *Environ. Sci. Technol.* **1996**, *30*, 2322–2331.

8. National Research Council, *Science and Technology for Environmental Cleanup at Hanford*, National Academy Press: New York, **2001**.

9. Gephart, R. E. A Short History of Waste Management at the Hanford Site. *Phys. Chem. Earth* **2010**, *35*, 298–306.

10. Maher, K.; Bargar. J. R.; Brown, G. E., Jr. Environmental Speciation of Actinides. *Inorg. Chem.* **2013**, *52*, 3510–3532.

11. Potocki, M.; Mayewski, P. A.; Kurbatov, A. V.; Simoes. J. C.; Dixon, D. A.; Goodwin, I.; Carleton, A. M.; Handley, M. J.; Jana, R.; Korotkikh, E. V. Recent Increase in Antarctic Peninsula Ice Core Uranium Concentrations. *Atmos. Environ.* **2016**, *140*, 381–385.

12. Steinhauser, G. Anthropogenic Radioactive Particles in the Environment. *J. Radioanal. Nucl. Chem.* **2018**, *318*, 1629–1639.

13. Reynolds. J. G.; Cooke, G. A.; Page. J. S.; Warrant, R. W. Uranium–Bearing Phases in Hanford Nuclear Waste. *J. Radioanal. Nucl. Chem.* **2018**, *316*, 289–299.

14. Kashcheev, V. A.; Chernikov, M. A.; Shadrin, A. Y. Radwaste Characteristics in Uranium–Plutonium Nuclear Fuel Production. *At. Energy* **2020**, *128*, 95–102.

15. Matthews, R. B.; Chidester, K. M.; Hoth, C. W.; Mason, R. E.; Petty, R. L. Fabrication and Testing of Uranium Nitride Fuel for Space Power Reactors. *J. Nucl. Mater.* **1988**, *151*, 345–356.

16. Rogozkin, B. D.; Stepennova, N. M.; Bergman, G. A.; Proshkin, A. A. Thermochemical Stability, Radiation Testing, Fabrication, and Reprocessing of Mononitride Fuel. *At. Energy* **2003**, *95*, 835–844.

17. Streit, M.; Ingold, F. Nitrides as a Nuclear Fuel Option. *J. Eur. Ceram. Soc.* **2005**, 25, 2687–2692.

18. Allen, D. J.; Blair, S. R.; Millerr, M. G.; Nelson, M. E.; Evaluation of Non–Oxide Fuel for Fission–Based Nuclear Reactors on Spacecraft. *Nucl. Technol.* **2019**, *205*, 755–765.

19. Evans, W. J.; Kozimor, S. A.; Ziller. J. W. Molecular Octa–Uranium Rings with Alternating Nitride and Azide Bridges. *Science* **2005**, *309*, 1835–1838.

20. Szabò, Z.; Toraishi, T.; Vallet, V.; Grenthe, I. Solution Coordination Chemistry of Actinides: Thermodynamics, Structure and Reaction Mechanisms, *Coord. Chem. Rev.* **2006**, *250*, 784–815.

21. Cocalia, V. A.; Gutowski, K. E.; Rogers, R. D. The Coordination Chemistry of Actinides in Ionic Liquids: A Review of Experiment and Simulation. *Coord. Chem. Rev.* **2006**, *250*, 755–764.

22. Fox, A. R.; Bart, S. C.; Meyer, K.; Cummins, C. C. Towards Uranium Catalysts. *Nature* **2008**, *455*, 341–349.

23. Fox, A. R.; Cummins, C. C. Uranium–Nitrogen Multiple Bonding: The Case of a Four–Coordinate Uranium(VI) Nitridoborate Complex. *J. Am. Chem. Soc.* **2009**, *131*, 5716–5717.

24. Thomson, R. K.; Cantat, T.; Scott, B. L.; Morris, D. E.; Batista, E. R.; Kiplinger. J. L. Uranium Azide Photolysis Results in C–H Bond Activation and Provides Evidence for a Terminal Uranium Nitride. *Nat. Chem.* **2010**, *2*, 723–729.

25. Fortier, S.; Wu, G.; Hayton, T. W. Synthesis of a Nitrido–Substituted Analogue of the Uranyl Ion, $[N{=}U{=}O]^{+}$. *J. Am. Chem. Soc.* **2010**, *132*, 6888–6889.

26. Hayton, T. W. Recent Developments in Actinide–Ligand Multiple Bonding. *Chem. Commun.* **2013**, *49*, 2956–2973

27. King, D. M.; Tuna, F.; McInnes, E. J. L.; McMaster, J.; Lewis, W.; Blake, A. J.; Liddle, S. T. Synthesis and Structure of a Terminal Uranium Nitride Complex. *Science* **2012**, *337*, 717–720.

28. King, D. M.; Tuna, F.; McInnes, E. J. L.; McMaster, J.; Lewis, W.; Blake, A. J.; Liddle, S. T. Isolation and Characterization of Uranium(VI)–Nitride Triple Bond. *Nat. Chem.* **2013**, *5*, 482–488.

29. King, D. M.; Liddle, S. T. Progress in Molecular Uranium–Nitride *Chemistry. Coord. Chem. Rev.* **2014**, *2*, 266–267.

30. Liddle, S. T. The Renaissance of Non–Aqueous Uranium Chemistry. *Angew. Chem. Int. Ed.* **2015**, *54*, 8604–8641.

31. Qiu, J.; Burns, P. C.; Clusters of Actinides with Oxide, Peroxide, or Hydroxide Bridges. *Chem. Rev.* **2013**, *113*, 1097–1120.

32. Cleaves, P. A.; Kefalidis, C. E.; Gardner, B. M.; Tuna, F.; McInnes, E. J. L.; Lewis, W.; Maron, L.; Liddle, S. T. Terminal Uranium(V/VI) Nitride Activation of Carbon Dioxide and Carbon Disulfide: Factors Governing Diverse and Well–Defined Cleavage and Redox Reactions. *Chem. Eur. J.* **2017**, *23*, 2950–2959.

33. Cowie, B. E.; Purkis. J. M.; Austin, J.; Love. J. B.; Arnold, P. L. Thermal and Photochemical Reduction and Functionalization Chemistry of the Uranyl Dication, $[U^{VI}O_2]^{2+}$. *Chem. Rev.* **2019**, *119*, 10595–10637.

34. Rudel, S. S.; Deubner, H. L.; Müller, M.; Karttunen, A. J.; Kraus, F. Complexes Featuring a Linear [N≡U≡N] Core Isoelectronic to the Uranyl Cation. *Nat. Chem.* **2020**, *12*, 962–967.

35. Wang, P.; Douair, I.; Zhao, Y.; Wang, S.; Zhu, J.; Maron, L.; Zhu, C. Facile Dinitrogen and Dioxygen Cleavage by a Uranium (III) Complex: Cooperativity Between the Non–Innocent Ligand and the Uranium Center. *Angew. Chem. Int. Ed.* **2021**, *60*, 473–479.

36. Heinemann, C.; Cornehl, H. H.; Schwarz, H. Hydrocarbon Activation by "Bare" Uranium Cations: Formation of a Cationic Uranium–Benzene Complex from Three Ethylene Units. *J. Organomet. Chem.* **1995**, *501*, 201–209.

37. Marçalo, J.; Leal. J. P.; de Matos, A. P.; Marshall A. G. Gas–Phase Actinide Ion Chemistry: FT–IRC/MS Study of the Reactions of Thorium and Uranium Metal and Oxide Ions with Arenes. *Organometallic*s **1997**, *16*, 4581–4589.

38. Gibson. J. K. Gas–Phase *f*–Element Organometallic Chemistry: Reactions of Cyclic Hydrocarbons with Th^+, U^+, ThO^+, UO^+, and Lanthanide Ions, Ln^+. *Organometallics* **1997**, *16*, 4214–4222.

39. Gibson. J. K. Gas–Phase Transuranium Chemistry: Reactions of Actinide Ions with Alcohols and Thiols. *J. Mass Spectrom.* **1999**, *34*, 1166–1177.

40. Gibson. J. K.; Gas–Phase Chemistry of Actinide Ions: Probing the Distinctive Character of the 5f Elements, *Int. J. Mass. Spectrom*. **2002**, *214*, 1–21.

41. Santons, M.; Marçalo, J.; de Matos, A. P.; Gibson. J. K.; Haire, R. G. Gas–Phase Oxidation Reactions of Neptunium and Plutonium Ions Investigated via Fourier Transform Ion Cyclotron Resonance Mass Spectrometry. *J. Phys. Chem. A* **2002**, *106*, 7190–7194.

42. Gibson. J. K.; Haire, R. G.; Santos, M.; Marçalo, J.; Matos, A. P. Oxidation Studies of Dipositive Actinide Ions, An^{2+} (An = Th, U, Np, Pu, Am) in the Gas Phase: Synthesis and Characterization of the Isolated Uranyl, Neptunyl, and Plutonyl Ions UO_2^{2+}(g), NpO_2^{2+}(g), and PuO_2^{2+}(g). *J. Phys. Chem. A* **2005**, *109*, 2768–2781.

43. Gibson. J. K.; Marçalo. J. New Developments in Gas–Phase Actinide Ion Chemistry. *Coord. Chem. Rev.* **2006**, *250*, 776–783.

44. Marçalo, J.; Gibson. J. K. Gas–Phase Energetics of Actinide Oxides: An Assessment of Neutral and Cation Monoxides and Dioxides from Thorium to Curium. *J. Phys. Chem. A* **2009**, *113*, 12599–12606.

45. Infante, I.; Kovacs, A.; La Macchia, G.; Shabi, A R. M.; Gibson. J. K.; Gagliardi, L. Ionization Energies for the Actinide Mono– and Dioxides Series, from Th to Cm: Theory Versus Experiment. *J. Phys. Chem. A* **2010**, *114*, 6007–6015.

46. Rutkowski, P. X.; Michelini, M. del C.; Gibson. J. K. Proton Transfer in Th(IV) Hydrate Clusters: A Link to Hydrolysis of $Th(OH)_2^{2+}$ to $Th(OH)_3^{+}$ in Aqueous Solution. *J. Phys. Chem. A* **2013**, *117*, 451–459.

47. van Stipdonk, M. J.; O'Malley, C.; Plaviak, A.; Martin, D.; Pestok, J.; Mihm, P. A.; Hanley, C. G.; Corcovilos, T. A.; Gibson. J. K.; Bythell, B. J. Dissociation of Gas–Phase, Doubly–Charged Uranyl–Acetone Complexes by Collisional Activation and Infrared Photodissociation. *Int. J. Mass Spectrom.* **2016**, *396*, 22–34.

48. Lucena, A. F.; Bandeira, N. A. G.; Pereira, C. C. L.; Gibson. J. K.; Marçalo. J. Synthesis, Structure and Bonding of Actinide Disulphide Dications in the Gas Phase. *Phys. Chem. Chem. Phys.* **2017**, *19*, 10685–10694.

49. Gibson. J. K.; de Jong, W. A.; Dau, P. D.; Gong, Y. Heptavalent Actinide Tetroxides NpO_4^- and PO_4^-: Oxidation of Pu(V) to Pu(VII) by Adding an Electron to PuO_4. *J. Phys. Chem. A* **2017**, *121*, 9156–9162.

50. Dau, P. D.; Dau, P. V.; Rao, L.; Kovács, A.; Gibson. J. K. A Uranyl Peroxide Dimer in the Gas Phase. *Inorg. Chem.* **2017**, *56*, 4186–4196.

51. Gresham, G. L.; Gianotto, A. K.; Harrington, P. de B.; Cao, L.; Scott, . R.; Olson. J. E.; Appelhans, A. D.; van Stipdonk, M. J.; Groenewold, G. S. Gas–Phase Hydration of U(IV), U(V) and U(VI) Monocations. *J. Phys. Chem. A* **2003**, *107*, 8530–8538.

52. van Stipdonk, M. J.; Chien, W.; Anbalagan, V.; Bulleigh, K.; Hanna, D.; Groenewold, G. S. Gas–Phase Complexes Containing the Uranyl Ion and Acetone. *J. Phys. Chem. A* **2004**, *108*, 10448–10457.

53. van Stipdonk, M. J.; Chien, W.; Bulleigh, K.; Wu, Q.; Groenewold, G. S. Gas–Phase Uranyl–Nitrile Complex Ions. *J. Phys. Chem. A* **2006**, *110*, 959–970.

54. Groenewold, G. S.; Cossel, K. C.; Gresham, G. L.; Gianotto, A. K.; Appelhans, A. D.; Olson. J. E.; van Stipdonk, M. J.; Chen, W. Binding of Molecular Oxygen to Di– and Tri–Ligated $[UO_2]^+$. *J. Am. Chem. Soc.* **2006**, *126*, 3075–3084.

55. Rios, D.; Rutkowski, P. X.; Shuh, D. K.; Bray, T. H.; Gibson. J. K.; van Stipdonk, M. J. Electron Transfer Dissociation of Dipositive Uranyl and Plutonyl Coordination Complexes. *J. Mass. Spectrom.* **2011**, *46*, 1247–1254.

56. Armentrout, P. B.; Beauchamp. J. L. Collision–Induced Dissociation of UO^+ and UO_2^+. *Chem. Phys.* **1980**, *50*, 21–25.

57. Cox, R. M.; Citir, M.; Armentrout, P. B.; Battey, S. R.; Peterson, K. A. Bond Energies of ThO^+ and ThC^+: A Guided Ion Beam and Quantum Chemical Investigation of the Reactions of Thorium Cation with O_2 and CO. *J. Chem. Phys.* **2016**, *144*, 184309–15.

58. Cox, R. M.; Armentrout, P. B.; de Jong, W. A. Reactions of $Th^+ + H_2$, D_2 and HD Studied by Guided Ion Beam Tandem Mass Spectrometry and Quantum Chemical Calculations. *J. Phys. Chem. B* **2016**, *120*, 1601–1614.

59. Cox, R. M.; Kafle, A.; Armentrout, P. B.; Peterson, K. A. Bond Energy of ThN^+: A Guided Ion Beam and Quantum Chemical Investigation of the Reactions of Thorium Cation with N_2 and NO. *J. Chem. Phys.* **2019**, *151*, 034304–16.

60. Kafle, A.; Nwokolo, C.; Sanchez, L.; Armentrout, P. B. Threshold Collision–Induced Dissociation of Hydrated Thorium (IV) Trihydroxy Cation: Spectroscopy of the Ground Theoretical Investigation of the Binding Energies for $Th(OH)_3^+(H_2O)_n$ Complexes (n = 1–4). *J. Phys. Chem. A* **2020**, *124*, 3090–3100.

61. Pillai, E. D.; Molek, K. S.; Duncan, M. A. Growth and Photodissociation of $U^+(C_6H_6)_n$ (n = 1–3) and $UO_m^+(C_6H_6)$ (m = 1,2) Complexes. *Chem. Phys. Lett.* **2005**, *405*, 247–251.

62. Marks, J. H.; Khan, P.; Vasiliu, M.; Dixon, D. A.; Duncan, M. A. Photodissociation and Theory to Investigate Uranium Oxide Cluster Cations. *J. Phys. Chem. A* **2020**, *124*, 1940–1953.

63. Green, D.W.; Reedy, G.T. The Identification of UN in Ar matrices. *J. Chem. Phys*., **1976**, *65*, 2921–2922.

64. Hunt, R. D.; Yustein. J. T.; Andrews, L. Matrix Infrared Spectra of NUN Formed by the Insertion of Uranium Atoms into Molecular Nitrogen. *J. Chem. Phys.* **1993**, *98*, 6070–6074.

65. Hunt, R. D.; Andrews, L. Reactions of Pulsed–Laser Evaporated Uranium Atoms with Molecular Oxygen: Infrared Spectra of UO, UO_2, UO_3, UO_2^+, UO_2^{2+}, and UO_3–O_2 n solid argon. *J. Chem. Phys.* **1993**, *98*, 3690–3696.

66. Kushto, G.P.; Souter, P.F.; Andrews, L.; Neurock, M. A. Matrix Isolation FT–IR and Quasirelativistic Density Functional Theory Investigation of the Reaction Products of Laser–Ablated Uranium Atoms with NO, NO_2 and N_2O. *J. Chem. Phys.*, **1997**, *106*, 5894–5903.

67. Zhou, M.; Andrews, L.; Li, J.; Bursten, B. E. Reaction of Laser–Ablated Uranium Atoms with CO: Infrared Spectra of the CUO, CUO^-, OUCCO, $(\eta^2–C_2)UO_2$, and $U(CO)_x$ (x = 1−6) Molecules in Solid Neon. *J. Am. Chem. Soc.* **1999**, *121*, 9712–9721.

68. Zhou, M.; Andrews, L., Infrared Spectra and Pseudopotential Calculations for NUO^+, NUO, and NThO in solid neon. *J. Chem. Phys.*, **1999**, *111*, 11044–11049.

69. Zhou, M.; Andrew, L.; Ismail, N.; Marsden, C. Infrared Spectra of UO_2, UO_2^+, and UO_2^- in Solid Neon. *J. Phys. Chem. A* **2000**, *104*, 5495–5502.

70. Li, J.; Bursten, B. E.; Andrews, L.; Marsden, C. J. On the Electronic Structure of Molecular UO_2 in the Presence of Ar Atoms: Evidence for Direct U–Ar Bonding. *J. Am. Chem. Soc.* **2004**, *126*, 3424–3425.

71. Wang, X.; Andrews, L.; Li, J.; Bursten, B. E. Significant Interaction Between Uranium and Noble–Gas Atoms: Coordination of the UO_2^+ Cation by Ne, Ar, Kr, and Xe Atoms. *Angew. Chem. Int. Ed.* **2004**, *43*, 2554–2557.

72. Wang X.; Andrews, L.; Li. J. Experimental and Theoretical Investigations of IR Spectra and Electronic Structures of the $U(OH)_2$, $UO_2(OH)$, and $UO_2(OH)_2$ Molecules, *Inorg. Chem.* **2006**, *45*, 4157–4166.

73. Andrews, L.; Wang, X.; Lindh, R.; Roos, B.O.; Marsden, C.J., Simple NUF_3 and PUF_3 Molecules with Triple Bonds to Uranium. *Angew. Chem. Int. Ed.*, **2008**, *47*, 5366–5370.

74. Wang, X.; Andrews, L.; Vlaisavljevich, B.; Gagliardi, L. Combined Triple and Double Bonds to Uranium: The N≡U═N–H Uranimine Nitride Molecule Prepared in Solid Argon. *Inorg. Chem.* **2011**, *50*, 3826–3831.

75. Andrews, L.; Wang, X.; Gong, Y.; Vlaisavljevich, B.; Gagliardi, L. Infrared Spectra and Electronic Structure Calculations for the NUN(NN)1–5 and NU(NN)1–6 Complexes in Solid Argon. *Inorg. Chem.* **2013**, *52*, 9989–9993.

76. Pereira, C. C. L.; Maurice, R.; Lucena, A. F.; Hu, S.; Gonçalves, A. P.; Marçalo, J.; Gibson. J. K.; Andrews, L.; Gagliardi, L. Thorium and Uranium Carbide Clusters in the Gas Phase: Similarities and Differences Between Thorium and Uranium, *Inorg. Chem.* **2013**, *52*, 10968–10975.

77. Andrews, L.; Wang, X.; Gong, Y.; Kushto, G. P.; Vlaisavljevich, B.; Gagliardi, L Infrared Spectra and Electronic Structure Calculations for NN Complexes with U, UN and NUN in Solid Argon, Neon and Nitrogen. *J. Phys. Chem. A* **2014**, *118*, 5289–5303.

78. Vent–Schmidt, T.; Andrews, L.; Riedel, S. Reactions of Laser–Ablated U Atoms with HF: Infrared Spectra and Quantum Chemical Calculations of HUF, UH and UF in Noble Gas Solids. *J. Phys. Chem. A* **2015**, *119*, 2253–2261.

79. Sankaran, K.; Sundararajan, K.; Viswanathan, K.S. A Matrix Isolation FTIR Investigation of Laser–Ablated Uranium Oxide in Argon and Nitrogen Matrices. *Bull. Mater. Sci.*, **1999**, *22*, 785–790

80. Sankaran, K.; Sundararajan, K.; Viswanathan, K.S. Matrix Isolation Infrared Studies of the Reactions of Laser–Ablated Uranium with N_2: Reactions Beyond Insertion into N_2. *J. Phys. Chem. A*, **2001**, *105*, 3995–4001.

81. Dau, P. D.; Su, J.; Liu, H.–T.; Huang, D.–L.; Wei, F.; Li, J.; Wang, L.–S. Photoelectron Spectroscopy and Theoretical Studies of UF_5^- and UF_6^-. *J. Chem. Phys.* **2012**, *136*, 194304–9.

82. Li, W.–L.; Su, J.; Jian, T.; Lopez, G. V.; Hu, H.–S.; Cao, G.–J.; Li, J.; Wang, L.–S. Strong Electron Correlation in UO_2^-: A Photoelectron and Relativistic Quantum Chemistry Study. *J. Chem. Phys.* **2014**, *140*, 094306–9.

83. Czekner, J.; Lopez, G. V.; Wang, L.–S. High Resolution Photoelectron Imaging of UO^- and UO_2^- and the Low–Lying Electronic States and Vibrational Frequencies of UO and UO_2. *J. Chem. Phys.* **2014**, *141*, 244302–8.

84. Su, J.; Dau, P. D.; Liu, H.–T.; Huang, D.–L.; Wei, F.; Schwarz, W. H. E.; Li, J.; Wang, L.–S. Photoelectron Spectroscopy and Theoretical Studies of Aqueous Uranium

Hexachlorides in Different Oxidation States: UCl_6^{q-} (q = 0–2). *J. Chem. Phys.* **2015**, *142*, 134308–13.

85. Roy, S. K.; Jian, T.; Lopez, G. V.; Li, W.–L.; Su, J.; Bross, D. H.; Peterson, K. A.; Wang, L.–S.; Li. J. A Combined Photoelectron Spectroscopy and Relativistic Ab Initio Studies of the Electronic Structures of UFO and UFO^+. *J. Chem. Phys.* **2016**, *144*, 084309–11.

86. Su, J.; Li, W.–L.; Lopez, G. V.; Jian, T.; Cao, G. J.; Li, W.–L.; Schwarz, W. H. E.; Wang, L.–S.; Li. J. Probing the Electronic Structure and Chemical Bonding of Mono–Uranium Oxides with Different Oxidation States: UO_x^- and UO_x (x = 3–5). *J. Phys. Chem. A* **2016**, *120*, 1084–1096.

87. Han, J.; Kaledin, L. A.; Goncharov, V.; Komissarov, A. V.; Heaven, M. C. Accurate Ionization Potentials of UO and UO_2: A Rigorous Test of Relativistic Quantum Chemistry Calculations. *J. Am. Chem. Soc.* **2003**, *125*, 7176–7177.

88. Han, J.; Goncharov, V.; Kaledin, L. A.; Komissarov, A. V.; Heaven, M. C. Electronic Spectroscopy and Ionization Potential of UO_2 in the Gas Phase. *J. Chem. Phys*. **2004**, *120*, 5155–5163.

89. Lue, C. J.; Jin, J.; Ortiz, M. J.; Rienstra–Kiracofe. J. C.; Heaven, M. C. Electronic Spectroscopy of UO_2 Isolated in a Solid Ar Matrix. *J. Am. Chem. Soc.* **2004**, *126*, 1812–1815.

90. Goncharov, V.; Han, J.; Kaledin, L. A.; Heaven, M. C. Ionization Energy Measurements and Electronic Spectra for ThO. *J. Chem. Phys*. **2005**, *122*, 204311–6.

91. Gagliardi, L.; Heaven, M. C.; Krogh. J. W.; Roos, B. O. The Electronic Spectrum of the UO_2 Molecule. *J. Am. Chem. Soc.* **2005**, *127*, 86–91.

92. Goncharov, V.; Heaven, M. C. Spectroscopy of the Ground and Low–Lying Excited States of ThO^+. *J. Chem. Phys.* **2006**, *124*, 064312–7.

93. Goncharov, V.; Kaledin, L. A.; Heaven, M. C. Probing the Electronic Structure of UO^+ with High–Resolution Photoelectron Spectroscopy. *J. Chem. Phys.* **2006**, *125*, 133202–8.

94. Heaven, M. C. Probing Actinide Electronic Structure Using Fluorescence and Multiphoton Ionization Spectroscopy. *Phys. Chem. Chem. Phys.* **2006**, *8*, 4497–4509.

95. Merritt. J. M.; Han, J.; Heaven, M. C. Spectroscopy of the UO_2^+ Cation and the Delayed Ionization of UO_2. *J. Chem. Phys.* **2008**, *125*, 084304–8.

96. Barker, B. J.; Antonov, I. O.; Heaven, M. C.; Peterson, K. A. Spectroscopic Investigations of ThF and ThF^+. *J. Chem. Phys.* **2012**, *136*, 104305–9.

97. Heaven, M. C.; Barker, B. J.; Antonov, I. O. Spectroscopy and Structure of the Simplest Actinide Bonds. *J. Phys. Chem. A* **2014**, *118*, 10867–10881.

98. Steimle, T. C.; Zhang, R.; Heaven, M. C.; The Pure Rotational Spectrum of Thorium Monosulfide, ThS. *Chem. Phys. Lett.* **2015**, *639*, 304–306.

99. VanGundy, R. A.; Bartlett. J. H.; Heaven, M. C.; Battey, S. R.; Peterson, K. A. Spectroscopic and Theoretical Studies of ThCl and $ThCl^+$. *J. Chem. Phys.* **2017**, *146*, 054307–8.

100. Battey, S. R.; Bross, D. H.; Peterson, K. A.; Persinger, T. D.; VanGundy, R. A.; Heaven, M. C. Spectroscopic and Theoretical Studies of UN and UN^+. *J. Chem. Phys.* **2020**, *152*, 094302–10.

101. Liu, G.; Zhang, C.; Ciborowski, S. M.; Asthana, A.; Cheng, L.; Bowen, K. H. Mapping the Electronic Structure of the Uranium (VI) Dinitride. *J. Phys. Chem. A* **2020**, *124*, 6486–6492.

102. Groenewold, G. S.; Gianotto, A. K.; Cossel, K. C.; van Stipdonk, M. J.; Moore, D. T.; Polfer, N.; Oomens, J.; de Jong, W. A.; Visscher, L. Vibrational Spectroscopy of Mass–Selected $[UO_2(ligand)_n]^{2+}$ Complexes in the Gas Phase: Comparison with Theory. *J. Am. Chem. Soc.* **2006**, *128*, 4802–4813.

103. Groenewold, G. S.; Oomens, J.; de Jong, W. A.; Gresham, G. L.; McIlwain, M. E.; van Stipdonk, M. J.; Vibrational Spectroscopy of Anionic Nitrate Complexes of UO_2^{2+} and Eu^{3+} Isolated in the Gas Phase. *Phys. Chem. Chem. Phys.* **2008**, *10*, 1192–1202.

104. Groenewold, G. S.; van Stipdonk, M. J.; de Jong, W. A.; Oomens, J.; Gresham, G. L.; McIlwain, M. E.; Gao, D.; Siboulet, B.; Visscher, L.; Kullman, M.; Polfer, N. Infrared Spectroscopy of Dioxouranium(V) Complexes with Solvent Molecules: Effect of Reduction. *ChemPhysChem* **2008**, 9, 1278–1285.

105. Groenewold, G. S.; de Jong, W. A.; Oomens, J.; van Stipdonk, M. J.; Variable Denticity in Carboxylate Binding to the Uranyl Coordination Complexes. *J. Am. Soc. Mass Spectrom.* **2010**, *21*, 719–727.

106. Groenewold, G. S.; van Stipdonk, M.J.; Oomens, J.; de Jong, W. A.; McIlwain, M. E. Vibrational Spectra of Discrete UO_2^{2+} Halide Complexes in the Gas Phase. *Int. J. Mass Spectrom.* **2010**, *297*, 67–75.

107. Groenewold, G. S.; van Stipdonk, M. J.; Oomens, J.; de Jong, W. A.; McIlwain, M. E.; The Gas Phase *Bis*–Uranyl Nitrate Complex $[(UO_2)_2(NO_3)_5]^-$: Infrared Spectrum and Structure. *Int. J. Mass Spectrom.* **2011**, *308*, 175–180.

108. Gibson. J. K.; Hu, H.–S.; van Stipdonk, M. J.; Berden, G.; Oomens, J.; Li. J. Infrared Multiphoton Dissociation of Uranyl and 3–oxa–glutaramide: An Extreme Red–Shift of the $[O=U=O]^{2+}$ Asymmetric Stretch. *J. Phys. Chem. A* **2015**, *119*, 3366–3374.

109. Dau, P. D.; Rios, D.; Gong, Y.; Michelini, M. del C.; Marçalo, J.; Shuh, D. K.; Mogannam, M.; van Stipdonk, M. J.; Corcovilos, T. A.; Martens, J.; Berden, G. Oomens, J.; Redlich, B.; Gibson. J. K. Synthesis and Hydrolysis of Uranyl, Neptunyl, and Plutonyl Gas–Phase Complexes Exhibiting Discrete Actinide–Carbon Bonds. *Organometallics* **2016**, *35*, 1228–1240.

110. Hu, S.–X.; Gibson. J. K.; Li, W.–L.; van Stipdonk, M. J.; Martens, J.; Berden, G.; Redlich, B.; Oomens, J.; Li. J. Electronic Structure and Characterization of a Uranyl di–15–crown–5 Complex with an Unprecedented Sandwich Structure. *Chem. Comm.* **2016**, *52*, 12761–12764.

111. de Jong, W. A.; Dau, P. D.; Wilson, R. E.; Marçalo, J.; Van Stipdonk, M. J.; Corcovilos, T. A.; Berden, G.; Martens, J.; Oomens, J.; Gibson. J. K. Revealing Disparate Chemistries of Protactinium and Uranium: Synthesis of the Molecular Uranium Tetroxide Anion, UO_4^-. *Inorg. Chem.* **2017**, *56*, 3686–3694.

112. Ricks, A. M.; Gagliardi, L.; Duncan, M. A. Infrared Spectroscopy of Extreme Coordination: The Carbonyls of U^+ and UO_2^+. *J. Am. Chem. Soc.* **2010**, *132*, 15905–15907.

113. Ricks, A. M.; Gagliardi, L.; Duncan, M. A. Oxides and Superoxides of Uranium Detected by IR Spectroscopy in the Gas Phase. *J. Phys. Chem. Lett.* **2011**, *2*,1662–1666.

114. Harvey. J. N. DFT Computation of Relative Spin–State Energetics of Transition Metal Compounds, *Structure and Bonding* **2004**, *112*, 151–184.

115. Cramer, C. J.; Truhlar, D. J. Density Functional Theory for Transition Metals and Transition Metal Chemistry. *Phys. Chem. Chem. Phys.* **2009** , *11*, 10757–10816.

116. Li, S.; Hennigan. J. M.; Dixon, D. A.; Peterson, K. A. Accurate Thermochemistry for Transition Metal Oxide Clusters. *J. Phys. Chem. A* **2009**, *113*, 7861–7877.

117. Cohen, A. J.; Mori–Sanchez, P.; Yang, W. Challenges for Density Functional Theory. *Chem. Rev.* **2012**, *112*, 289–320.

118. Burke, K. Perspective on Density Functional Theory. *J. Chem. Phys.* **2012**, *136*, 150901–9.

119. Shil, S.; Bhattacharya, D.; Sarkar, S.; Misra, A. Performance of the Widely Used Minnesota Density Functionals for the Prediction of Heat of Formations, Ionization Potentials of Some Benchmarked First Row Transition Metal Complexes. *J. Phys. Chem. A* **2013**, *117*, 4945–4955.

120. Swart, M.; Costas, M. *Spin States in Biochemistry and Inorganic Chemistry: Influence on Structure and Reactivity*, John Wiley and Sons: Chichester, U.K., **2016**.

121. Pepper, M.; Bursten, B. E.; The Electronic Structure of Actinide–Containing Molecules: A Challenge to Applied Quantum Chemistry. *Chem. Rev.* **1991**, *91*, 719–741.

122. Hay, P. J.; Martin, R. L. Theoretical Studies of the Structures and Vibrational Frequencies of Actinide Compounds Using Relativistic Effective Core Potentials with Hartree–Fock and Density Functional Methods: UF_6, NpF_6 and PuF_6. *J. Chem. Phys.* **1998**, *109*, 3875–3881.

123. Schreckenbach, G.; Hay, P. J.; Martin, R. L. Density Functional Calculations on Actinide Complexes: Survey of Recent Progress and Application to $[UO_2X_4]^{2-}$ (X = F, Cl, OH) and AnF_6 (An = U, Np, Pu). *J. Comput. Chem.* **1999**, *20*, 70–79.

124. Prodam, I. D.; Scuseria, G. E.; Martin, R. L. Covalency in The Actinide Dioxides: Systematic Study of the Electronic Properties Using Screened Hybrid Density Functional Theory. *Phys. Rev. B* **2007**, *76*, 033101–4.

125. Dolg, M. Relativistic Effective Core Potentials, in *Relativistic Electronic Structure Theory. Part 1. Fundamentals*, edited by P. Schwerdtfeger, Elsevier: Amsterdam, **2002**.

126. Cao, X.; Dolg, M. Relativistic Energy–Consistent Ab Initio Pseudopotentials as Tools for Quantum Chemical Investigations of Actinide Systems. *Coord. Chem. Rev.* **2006**, *250*, 900–910.

127. Dolg, M.; Cao, X.; Accurate Relativistic Small–Core Pseudopotentials for Actinides. Energy Adjustment for Uranium and First Applications to Uranium Hydride. *J. Phys. Chem. A* **2009**, *113*, 12573–12581.

128. Dolg, M.; Cao, X. Accurate Relativistic Small–Core Pseudopotentials for Actinides. Energy Adjustment for Uranium and First Applications to Uranium Hydride. *J. Phys. Chem. A*, **2009**, *113*, 12573–12581.

129. Weigand, A.; Cao, X.; Hangele, T.; Dolg, M. Relativistic Small–Core Pseudopotentials for Actinium, Thorium, and Protactinium. *J. Phys. Chem. A* **2014**, *118*, 2519–2530.

130. Majumdar, D.; Balasubramanian, K.; Nitsche, H. A Comparative Theoretical Study of Bonding in UO_2^{++}, UO_2^{+}, UO_2, UO_2^{-}, OUCO, $O_2U(CO)_2$ and UO_2CO_3. *Chem. Phys. Lett.* **2002**, *361*, 143–151.

131. Han, Y.–K.; Hirao, K. Density Functional Studies of UO_2^{2+} and AnF_6 (An = U, Np, and Pu) Using Scalar–Relativistic Effective Core Potentials. *J. Chem. Phys.* **2000**, *113*, 7345–7350.

132. Gagliardi, L.; Roos, B.; Malmquist, P.–Å.; Dyke. J. On the Electronic Structure of the UO_2 Molecule. J. *Phys. Chem. A* **2001**, *105*, 10602–10606.

133. Gagliardi, L.; Roos, B. Multiconfigurational Quantum Chemical Methods for Molecular Systems Containing Actinides. *Chem. Soc. Rev.* **2007**, *36*, 893–903.

134. Cao, Z.; Balasubramanian, K. Theoretical Studies of $UO_2(H_2O)_n^{2+}$, $NpO_2(H_2O)_n^{+}$, and $PuO_2(H_2O)_n^{2+}$ Complexes (n = 4–6) in Aqueous Solution and Gas Phase. *J. Chem. Phys.* **2005**, *123*, 114309–12.

135. Petit, L.; Joubert, L.; Maldivi, P.; Adamo, C. A Comprehensive Theoretical View of the Bonding in Actinide Molecular Complexes. *J. Am. Chem. Soc.* **2006**, *128*, 2190–2191.

136. Iché–Tarrat, N.; Marsden, C. J. Examining the Performance of DFT Methods in Uranium Chemistry: Does Core Size Matter for a Pseudopotential? *J. Phys. Chem. A* **2008**, *112*, 7632–7642.

137. Ruipérez, F. Danilo, C.; Réal, F.; Flament, J.–P.; Vallet, V.; Wahlgren, U. An Ab Initio Study of the Electronic Structure of UO_2^{+} and $[UO_2(CO_3)_3]^{5-}$. *J. Phys. Chem. A* **2009**, *113*, 1420–1428.

138. Tecmer, P.; Gomes, A. S. P.; Ekström, U.; Visscher, L. Electronic Spectroscopy of UO_2^{2+}, NUO^{+}, and NUN: An Evaluation of Time–Dependent Density Functional Theory for Actinides. *Phys. Chem. Chem. Phys.* **2011**, *13*, 6249–6259.

139. Wang, D.; van Gunsteren, W. F.; Chai, Z. Recent Advances in Computational Actinoid Chemistry. *Chem. Soc. Rev.* **2012**, *41*, 5836–5865.

140. Wen, X.–D.; Martin, R. L.; Henderson, T. M.; Scuseria, G. E. Density Functional Theory Studies of the Electronic Structure of Solid State Actinide Oxides. *Chem. Rev.* **2013**, *113*, 1063–1096.

141. Bross, D. H.; Parmar, P.; Peterson, K. A. Multireference Configuration Interaction Calculations of the First Six Ionization Potentials of the Uranium Atom. *J. Chem. Phys.* **2015**, 143, 184308–7.

142. Yong, Y.; Liu, H.; Zhang, P. Structural and Electronic Properties of U_nO_m (n = 1–3, m = 1–3n) Clusters: A Theoretical Study Using Screened Hybrid Density Functional Theory. *J. Chem. Phys.* **2016**, *144*, 184304–11.

143. Kovács, A.; Konings, R. J. M.; Gibson. J. K.; Infante, I.; Gagliardi, L. Quantum Chemical Calculations and Experimental Investigations of Molecular Actinide Oxides. *Chem. Rev.* **2015**, *115*, 1725–1759.

144. Stoneburner, S. J.; Truhlar, D. G.; Gagliardi, L. Transition Metal Spin–State Energetics by MC–PDFT with High Local Exchange. *J. Phys. Chem. A* **2020**, *124*, 1187–1195.

CHAPTER 2

EXPERIMENTAL AND THEORETICAL METHODS

EXPERIMENTAL APPARATUS

Pulsed supersonic expansion into a vacuum chamber is accomplished with the use of a series 9 General Valve (Parker Hannifin Corp.). The expansion gas is generally a rare gas mixed with a low concentration of a ligand of interest. Alternatively, ligands which are available a compressed gas can be used pure in an expansion, i.e. carbon monoxide, carbon dioxide, nitrogen. Laser vaporization of a metal rod produces a plasma that mixes with the expanding gas. This initially creates a hot reactive gas mixture where complexes may react before rapidly cooling due to the supersonic expansion. The extent of reaction between the metal and gas can be controlled by confining the gas and plasma using metal blocks to contain the metal rod and expansion gas, the varieties of which are detailed in Figure 2.1 and have been discussed in prior publications.[1] Channels bored through these cluster sources allow for the metal rod, laser, and gas to pass through. By varying the diameter and length of the channel through which the gas flows the degree of clustering can be controlled. The standard cluster source simply has a gas channel of consistent diameter bored through with a growth channel after the metal rod to force the gas and metal plasma to interact before expansion and cooling. The diameter and length of the gas channel are decreased and increased, respectively, to promote clustering at the cost of signal and cooling. The cutaway source allows expansion at the point where the metal plasma and gas first mix, resulting in fewer reactions and a colder expansion. The offset source allows the expansion gas and metal plasma to expand before mixing, resulting in the coldest expansion.

The molecules formed in the source move with uniform velocity through a skimmer to form a molecular beam and pass into a differentially pumped mass spectrometer chamber.

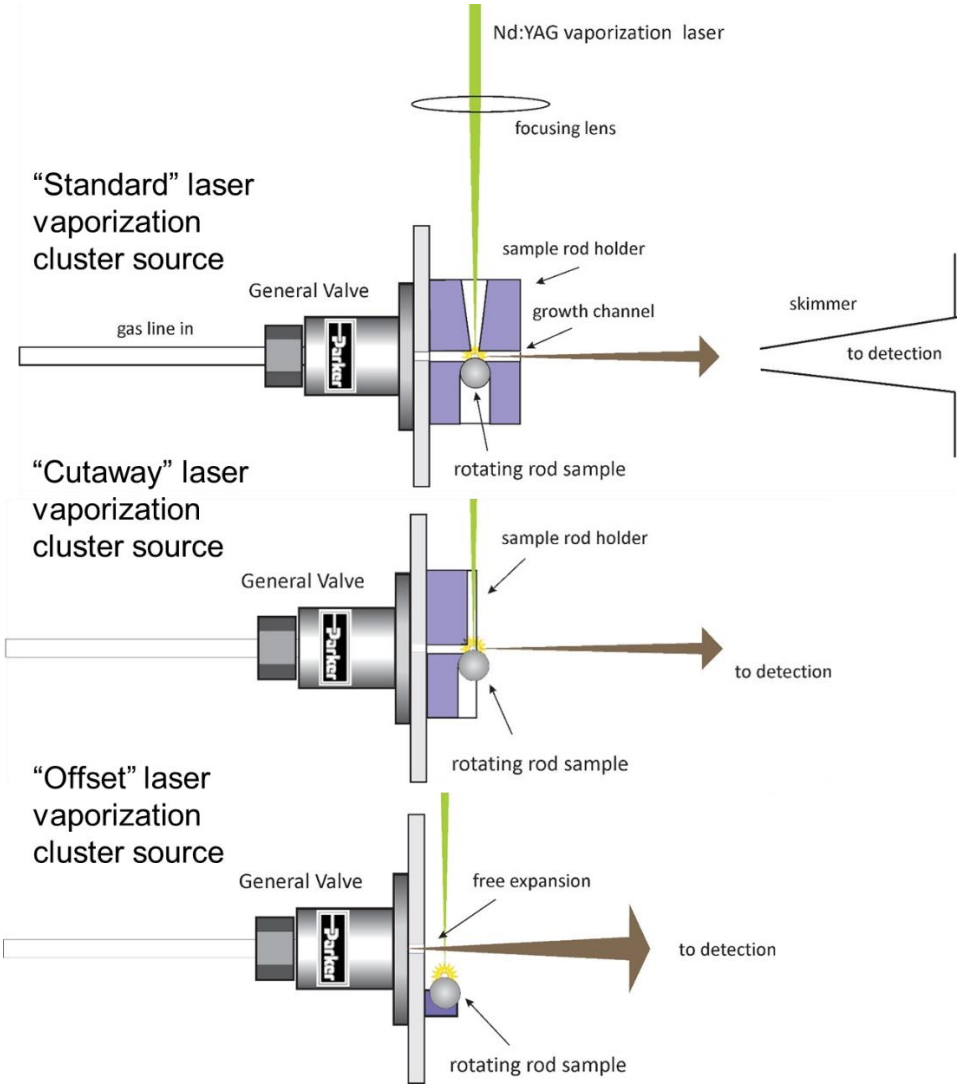

Figure 2.1. Diagram of commonly used laser vaporization cluster sources. The standard source shown can be extended with threaded channels of various lengths and diameters. The cutaway and offset offer colder expansions with less clustering.

A reflectron time–of–flight mass spectrometer is used for mass–analysis and mass–selective photodissociation.[2] A diagram of this instrument is shown in Figure 2.2. The molecular beam is produced by the gas expansion in the source chamber, which is separated

from the mass spectrometer by the skimmer. The mass spectrometer chamber is differentially pumped and baffled to maintain high vacuum (10^{-7}–10^{-5} torr).

Wiley–McLaren style electrodes are used to accelerate ions orthogonal to the direction of travel in the molecular beam.[3] These three electrodes are composed of a biased repeller, a tunable draw–out–grid of intermediate voltage, and ground electrode. The draw–out–grid voltage is adjusted to produce spatial focusing at the detector or the photodissociation region. The draw–out–grid and repeller electrodes produce a weak electric field for spatial focusing along the direction of travel of the ion packet. The stronger electric field produced by the draw–out–grid and ground electrodes is responsible for the bulk of the acceleration. A deflector compensates for the translational energy of the ions in the molecular beam, though this introduces a mass discrimination favoring heavier ions when voltage in increased. An einzel lens is situated between the deflector and flight tube; the voltage is adjusted to focus ions at the dissociation region or detector.

A pulsed deflector is located in the flight tube partway between the ion optics and reflectron. This is used to reject all ions outside a given mass range from passing on to the reflectron and detector. A high voltage complement pulse maintains voltage on the pusher, rejecting ions passing through, at all times other than when an ion of interest passes through. This allows for a specific mass from those observed to be studied exclusively with photodissociation.

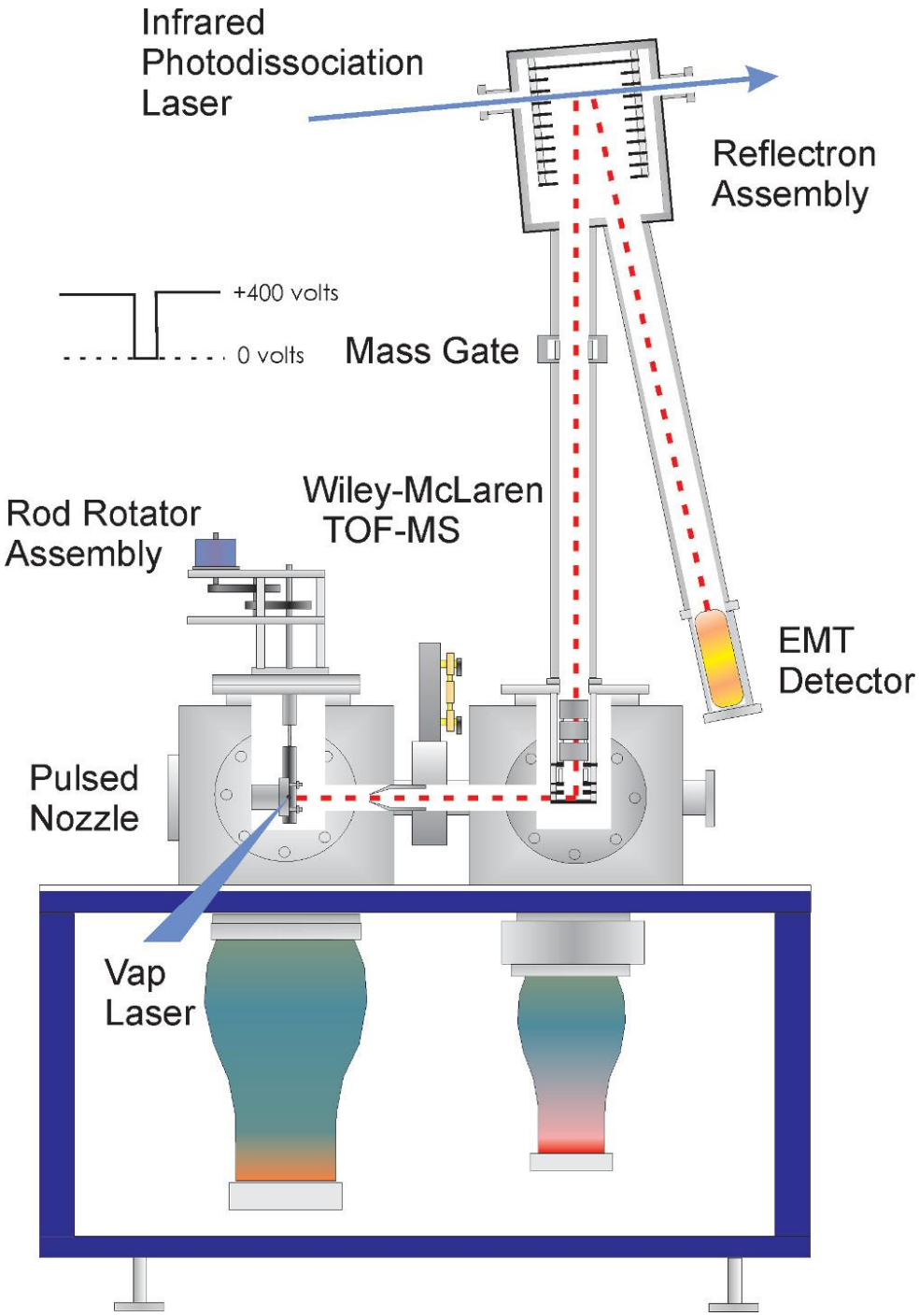

Figure 2.2. This instrument diagram shows the so–called source chamber on the left where supersonic expansion is carried out with an excess of pumping capacity. The skimmed molecular beam follows the dashed red line into the mass spectrometer where mass analysis and spectroscopy take place.

The reflectron is designed to maintain two regions of differing electrostatic field gradients. Ions entering the reflectron immediately lose most of their kinetic energy due to a

steep initial electric field. The rear of the reflectron maintains a weaker electric field, increasing the amount of time ions spend in this region. The relatively slow motion of ions in this region makes it ideal for photodissociation, and laser radiation can be passed through the reflectron at the point where the ions turn around. Ions and any photodissociation products are then reaccelerated by the reflectron towards the detector.

A section of the flight tube between the reflectron and detector is electrically isolated and termed the post–accelerator. This can be pulsed to high voltage while ions are inside it, and when ions exit they are accelerated. This increases the kinetic energy in eV of the ions by the voltage on the post–accelerator, substantially increasing the signal to noise ratio. The ions then impact the electron multiplier tube detector (Electron Multiplier Tube, Hamamatsu Photonics K. K.).

A variety of lasers are used to produce light with sufficient fluence for pulsed photodissociation. Fundamental frequency and second, third, and fourth harmonics (1064, 532, 355, 266 nm respectively) of a Spectra Physics GCR–150 Nd:YAG can be directed through the reflectron for fixed frequency photodissociation. A Spectra Physics PRO–230 Nd:YAG laser is used to pump a Laser Vision OPO/OPA laser system which produces tunable infrared light. The optical parametric oscillator (OPO) produces near infrared light from 4500 to 9000 cm^{-1} from Nd:YAG second harmonic light at 532 nm. The near infrared and Nd:YAG 1064 nm light is used for further difference frequency generation (DFG) by optical parametric amplification (OPA) to produce mid infrared light from 2000 to 4500 cm^{-1}. An external AgGaSe crystal is used to mix mid and near infrared for further DFG to produce far infrared light from 700 to 2000 cm^{-1}.

Measurements of laser fluence are vital for accurate analysis of the laser power dependence of an observed photodissociation process. To measure laser area, an impression of the laser is made with either ZAP–IT or linagraph paper (Linagraph Direct Print Type 1985, Kodak) which has been aged in sunlight. For lasers operating with more than 1 mJ/pulse average power is measured with a calorimeter power meter (PowerMax PM30V1, Coherent Inc.). Lasers operating below 1 mJ/pulse are not readily detectable with a calorimeter power meter, so a radiometer power meter (RjP–435, LaserProbe) measures average pulse energy.

COMPUTATIONAL METHODS

CCSD(T)/aug–cc–pVTZ is considered a gold standard level of theory. However, the computational cost of such a calculation with an actinide and ligands is staggering. The number of ways partially occupied d and f orbitals can be constructed regularly results in multireference character for transition metals and actinides. Single reference ab initio theory is expected to perform poorly compared to DFT in mildly multireference systems, while neither may perform well for strongly multireference systems.[4,5] The hybrid B3LYP and pure PBEh functionals are reliable functionals in the treatment of transition metals and are popular choices for large actinide calculations.[4–6]

All–electron calculations are standard for molecules containing only light atoms. Atoms heavier than zinc experience contraction of low angular momentum orbitals, primarily s, due to electrons accelerating to relativistic velocities when approaching the nucleus. Several Hamiltonians which include terms for relativistic effects have been proposed, including the zero–order and infinite order relativistic approximation (ZORA and IORA)[7–11], the Douglass–Kroll–Hess Hamiltonian (DKH)[12–14], and the exact two component relativistic Hamiltonian (X2C)[15].

The necessity of including all electrons of an actinide and its ligands in the relativistic Hamiltonian calculation render these methods prohibitively expensive for large molecules, and surveying large number of isomers. Basis sets have been published for use specifically with the DKH, ZORA, and X2C Hamiltonians.[16–18]

An alternative for computational treatment of all electrons is the use of an effective core potential (ECP). In this scheme the core electrons are represented by a single highly detailed wavefunction with an effective charge equal to the sum of all electrons replaced. The parameters of the wave function are optimized to reduce energy in a relativistic Hamiltonian. Valence basis sets are then constructed around the ECP intended for use only in that combination to avoid basis set incompleteness error. This method provides accurate representations of relativistic effects on the most strongly affected electrons, which are generally core electrons low in both n and l quantum numbers. This provides the benefit of considering fewer electrons and speeding up calculations. Older ECP basis sets such as Stuttgart/Dresden (SDD)[19–21] have recently been superseded by the Stuttgart/Köln.[22–24] These modern ECPs have been used to produce Dunning style basis sets for relativistic atoms compatible with Dunning basis sets on other elements. This family of basis sets is referred to in the literature as cc–pVnZ–PP, or more infrequently AVnZ (n = D, T, Q, 5).

The presence of occupied f orbitals poses significant challenges to computational quantum chemistry.[25,26] The large number of nodal planes and more detailed structure of *f* orbitals can cause numerical errors when a grid of insufficient resolution is used for integration. This is irrelevant in ab initio theory which makes use of analytical integrals, but all DFT uses grid integration. Many actinide containing molecules require at least double the default grid resolution of most computational packages.

Wavefunction stability is a further concern for any molecule containing partially occupied d or f orbitals.[27–29] An initial guess of the electronic state of a molecule produced by any software package must be tested for stability. This is usually accomplished with a CIS excited state calculation, which seeks to identify if the test Hartree–Fock or Kohn–Sham wavefunction is an excited or non–stationary state. Computational packages such as Gaussian16, Orca, and Cfour all include wavefunction stability tests.[30–32] The ability to test the stability of a wavefunction while using a relativistic all–electron Hamiltonian has not yet been implemented.

REFERENCES

1. Duncan, M. A. Invited Review Article: Laser Vaporization cluster Sources. *Rev. Sci. Instrum.* **2012**, *83*, 041101–19.
2. Wiley, W. C.; McLaren, I. H. Time–of–Flight Mass Spectrometer with Improved Resolution. *Rev. Sci. Instrum.* **1955**, *26*, 1150–1157.
3. Cornett, D. S.; Peschke, M.; LaiHing, K.; Cheng, P. Y.; Willey, K. F.; Duncan, M. A. Reflectron Time–of–Flight Mass Spectrometer for Laser Photodissociation. *Rev. Sci. Instrum.* **1992**, *63*, 2177–2186.
4. Cramer, C. J.; Truhlar, D. G. Density Functional Theory for Transition Metals and Transition Metal Chemistry. *Phys. Chem. Chem. Phys.* **2009**, *11*, 10757–10816.
5. Verma, P.; Truhlar, D. G. Status and Challenges of Density Functional Theory. *CellPress Rev.* **2020**, *2*, 302–318.
6. Dolg, M. *Computational Methods in Lanthanide and Actinide Chemistry*. Wiley: New York, **2015**.

7. van Lenthe, E.; Baerends, E. J.; Snijders, J. G. Relativistic Regular Two–Component Hamiltonians. *J. Chem. Phys.* **1993**, *99*, 4597–4610.

8. van Lenthe, E.; Baerends, E. J.; Snijders, J. G. Relativistic Total Energy Using Regular Approximations. *J. Chem. Phys.* **1994**, *101*, 9783–9792.

9. van Lenthe, E.; Baerends, E. J.; Snijders, J. G. The Zero–Order Regular Approximation for Relativistic Effects: The Effect of Spin–Orbit Coupling in Closed Shell Molecules. *J. Chem. Phys.* **1996**, *105*, 6505–6516.

10. van Wüllen, C. Molecular Density Functional Calculations in the Regular Relativistic Approximation: Method, Application to Coinage Metal Diatomics, Hydrides, Fluorides, and Clorides and Comparison with First–Order Relativistic Calculations. *J. Chem. Phys.* **1988**, *109*, 392–399.

11. Dyall, K. G.; van Lenthe, E. Relativistic Regular Approximations Revisited: An Infinite–Order Relativistic Approximation. *J. Chem. Phys.* **1999**, *111*, 1366–1372.

12. Douglas, M.; Kroll, N. M. Quantum Electrodynamical Corrections to the Fine–Structure of Helium. *Ann. Phys.* **2018**, *82*, 89–155.

13. Jansen, H.; Hess, B. A. Revision of the Douglas–Kroll Transformation, *Phys. Rev. A* **1989**, *39*, 6016–6017.

14. Reiher, M.; Wolf, A. Exact decoupling of the Dirac Hamiltonian. II. The Generalized Douglas–Kroll–Hess Transformation up to Arbitrary Order. *J. Chem. Phys.* **2004**, *121*, 10945–10956.

15. Ilias, M.; Saue, T. An Infinite–Order Two–Component Relativistic Hamiltonian by a Simple One–Step Transformation. *J. Chem. Phys.* **2007**, *126*, 064102–9.

16. Pantazis, D. A.; Chen, X.–Y.; Landis, C. R.; Neese, F. All–Electron Acalar Relativistic Basis Sets for Third–Row Transition Metal Atoms. *J. Chem. Theory Comput.* **2008**, *4*, 908–919.

17. K.A. Peterson, K. A. Correlation Consistent Basis Sets for Actinides. I. The Th and U Atoms. *J. Chem. Phys.* **2015**, *142*, 074105–14.

18. Feng, R; Peterson, K. A. Correlation Consistent Basis Sets for Lanthanides: The Atoms La–Li. *J. Chem. Phys.* **2017**, *147*, 084108–11.

19. Kuchle, W.; Dolg, M.; Stoll, H.; Preuss, H. Energy–Adjusted Pseudopotentials for the Actinides – Parameter Sets and Test Calculations for Thorium and Thorium Monoxide. *J. Chem. Phys.* **1994**, *100*, 7535–7542.

20. Cao, X. Y.; Solg, M. Segmented Contraction Scheme for Small–Core Actinide Pseudopotential Basis Sets. *J. Mol. Struc.: Theochem*, **2004**, *673*, 203–209.

21. Cao, X. Y.; Dolg, M.; Stoll, H.; Valence Basis Sets for Relativistic Energy–Consistent Small–Core Actinide Pseudopotentials. *J. Chem. Phys.* **2003**, *118*, 487–496.

22. Peterson, K. A. Correlation Consistent Basis Sets for Actinides. I. The Th and U Atoms. *J. Chem. Phys.* **2015**, *142*, 074105–14.

23. Dolg, M.; Cao, X. Accurate Relativistic Small–Core Pseudopotentials for Actinides. Energy Adjustment for Uranium and First Applications to Uranium Hydride. *J. Phys. Chem. A*, **2009**, *113*, 12573–12581.

24. Weigand, A.; Cao, X.; Hangele, T.; Dolg, M. Relativistic Small–Core Pseudopotentials for Actinium, Thorium, and Protactinium. *J. Phys. Chem. A* **2014**, *118*, 2519–2530.

25. Gibson, J. K. Gas–Phase Chemistry of Actinide Ions: Probing the Distinctive Character of the 5f Elements. *Int. J. Mass Spectrom.* **2002**, *214*, 1–21.

26. Neidig, M. L.; Clark, D. L.; Martin, R. L. Covalency in f–Element Complexes. *Coord. Chem. Rev.* **2013**, *257*, 394–406.

27. Seeger, R.; Pople, J. A. Self–Consistent Molecular–Orbital Methods. 18. Constraints and Stability in Hartree–Fock Theory. *J. Chem. Phys.* **1977**, 3045–3050.

28. Bauernschmitt, R.; Ahlrichs, R. Stability Analysis for Solutions of the Closed Shell Kohn–Sham Equation. *J. Chem. Phys*. **1996**, *104*, 9047–9052.

29. Ögretir, C.; Csizmadia, I. G. *Computational Advances in Organic Chemistry: Molecular Structure and Reactivity*. Springer: Dordrecht, **1991**.

30. Frisch, M. J.; Trucks, G. W.; Schlegel, H. B.; Scuseria, G. E.; Robb, M. A.; Cheeseman, J. R.; Scalmani, G.; Barone, V.; Petersson, G. A.; Nakatsuji, H.; Li, X.; Caricato, M.; Marenich, A. V.; Bloino, J.; Janesko, B. G.; Gomperts, R.; Mennucci, B.; Hratchian, H. P.; Ortiz, J. V.; Izmaylov, A. F.; Sonnenberg, J. L.; Williams–Young, D.; Ding, F.; Lipparini, F.; Egidi, F.; Goings, J.; Peng, B.; Petrone, A.; Henderson, T.; Ranasinghe, D.; Zakrzewski, V. G.; Gao, J.; Rega, N.; Zheng, G.; Liang, W.; Hada, M.; Ehara, M.; Toyota, K.; Fukuda, R.; Hasegawa, J.; Ishida, M.; Nakajima, T.; Honda, Y.; Kitao, O.; Nakai, H.; Vreven, T.; Throssell, K.; Montgomery, J. A., Jr.; Peralta, J. E.; Ogliaro, F.; Bearpark, M. J.; Heyd, J. J.; Brothers, E. N.; Kudin, K. N.; Staroverov, V. N.; Keith, T. A.; Kobayashi, R.; Normand, J.; Raghavachari, K.; Rendell, A. P.; Burant, J. C.; Iyengar, S. S.; Tomasi, J.; Cossi, M.; Millam, J. M.; Klene, M.; Adamo, C.; Cammi, R.; Ochterski, J. W.; Martin, R. L.; Morokuma, K.; Farkas, O.; Foresman, J. B.; Fox, D. J. *Gaussian 16 Revision C.01*, Gaussian, Inc., Wallingford CT, **2016**.

31. Neese, F.; Wennmohs, F.; Becker, U.; Riplinger, C. The ORCA Quantum Chemistry Program Package. *J. Chem. Phys.* **2020**, *152*, 224108–18.

32. Matthews, D. A.; Cheng, L.; Harding, M. E.; Lipparini, F.; Stopkowicz, S.; Jagau, T.–C.; Szalay, P. G.; Gauss, J.; Stanton, J. F. Coupled–Cluster Tenchniques for Computational Chemistry: The CFOUR Program Package. *J. Chem. Phys.* **2020**, *152*, 214108–35.

CHAPTER 3

PHOTODISSOCIATION AND THEORY TO INVESTIGATE URANIUM OXIDE CLUSTER CATIONS

Accepted by the Journal of Physical Chemistry A.

Reprinted here with the permission from *J. Phys. Chem. A* **2020**, *124*, 1940–1953.

Photodissociation and Theory to Investigate Uranium Oxide Cluster Cations

Joshua H. Marks[1], Paula Kahn[2], Monica Vasiliu[2], David A Dixon[2], Michael A. Duncan[1*]

[1]Department of Chemistry, University of Georgia, Athens, Georgia, U.S.A.

[2]Department of Chemistry & Biochemistry, University of Alabama, Tuscaloosa, Alabama, U.S.A.

[*]E–mail: maduncan@uga.edu

ABSTRACT

Uranium oxide cluster cations are produced by laser vaporization of a uranium rod in a pulsed supersonic expansion and detected with time–of–flight mass spectrometry. Ions are mass–selected and studied via multiphoton dissociation using the third harmonic of a Nd:YAG laser (355 nm). Cations of the stoichiometry $U_nO_{3n-1}^+$ were observed as photofragments from all photodissociated cluster cations. $U_nO_{3n}^+$ clusters were also observed to result from dissociation of larger $U_nO_{3n}^+$ clusters. Electronic structure calculations were used to predict the stability of the observed uranium oxide cluster cations using density functional theory with the hybrid B3LYP exchange–correlation functional and cc–pVnZ–PP basis sets (n = D, T), including diffuse orbitals as computational expense and availability permit. Clustering energies, relative energies and dissociation energies of the cations are reported. The Natural Population Analysis results based on the Natural Bond Orbitals (NBOs) indicate clusters composed of uranyl UO_2^{2+} units bound together by bridging O^{2-}. Spin and charge are found to be localized to the *5f* orbital of a single uranium atom within each charged cluster.

INTRODUCTION

Uranium oxide is found in nature containing uranium atoms in a variety of oxidation states.[1–3] UO_2, and UO_3 are known, though many ores with these oxidation states yield U_3O_8 upon exposure to atmospheric conditions.[4–5] When uranium is mined, used in munitions, or improperly stored, such as radioactive sludge found at the Hanford site, environmental contamination can result in the form of small uranium oxide particles.[6–10] The structure, solvation, and chemistry of these particles are of interest. The spectroscopy of $UO_n^{0/+}$ has been studied extensively in the past.[11–19] Recently, the spectroscopy of uranium containing molecules has been developed into an effective tool for identification, electronic, and structural analysis.[20–24] Mass spectrometry research on uranium has focused on reactivity and isotopic analysis of the uranium atom, though UO^+ and UO_2^+ are frequently observed during isotopic analysis.[25–47] Theoretical studies on these species have been limited by computational expense in the past, but recent advances in methods and basis sets have facilitated high quality calculations.[48–55] Both collisional dissociation and photodissociation with mass spectrometry have been used in the past to determine stable stoichiometries of transition metal and lanthanide oxides. Only the most strongly bound clusters are expected to result from energetic dissociation provided by multiphoton absorption.[56–71] In the present study we examine the stable stoichiometries of small uranium oxide clusters by use of mass spectrometry and fixed frequency photodissociation.

Previous research on the chemistry of uranium oxide has focused on the reactivity of UO^+ and UO_2^+. Schwarz and coworkers have shown that U^+ can catalyze the formation of benzene from ethylene and compared the rates of reaction between UO_2^+ and U^+.[30–31] Duckworth and coworkers have investigated the interactions of UO^+ with other unsaturated hydrocarbons and found similarities to the reactivity of Sm^+.[32–33] Gibson and coworkers have investigated the

oxidation chemistry of uranyl and have discussed in detail the role that frontier *f*–orbitals play in its chemistry.[32,34–37] Notably the contraction of the *5f*–orbitals in Pu and heavier elements limit the role of these orbitals in reactions. Lighter actinides Ac–Np feature *5f*–orbitals that participate in bonding and reactions when symmetry allows, however periodic trends lack predictive power for these elements.[34] Van Stipdonk and coworkers have studied the complexation behavior of the ubiquitous uranyl ion using infrared spectroscopy with the aid of high accuracy computational chemistry.[36–44] Computational chemistry investigating these elements is a developing field that has seen rapid recent advancements. The relativistic effects that dominate uranium chemistry necessitate either an all–electron calculation with a relativistic Hamiltonian or the use of a high quality relativistic pseudopotential. This has led to the development of the cc–pVnZ–PP basis set family by Peterson and relativistic pseudopotentials by Dolg and Cao which have seen wide application in predictions of structure and reactivity in uranium bearing molecules.[54–55] To our knowledge, uranium oxide cluster cations have not been studied with the use of photodissociation or computational chemistry.

Mass spectrometry has been successfully used to determine the stable stoichiometries of small metal oxide clusters with a range of techniques.[56–71] Mass–selected photodissociation is insensitive to the technique used to produce ions, and laser vaporization produces large quantities of metal oxide cluster cations in a number of oxidation states.[71–72] Prior experiments have succeeded in determining the stable stoichiometries of several transition metal and lanthanide oxides. In some systems the preferred stoichiometry indicates a cluster oxidation state that is the same as that found in the bulk metal oxide. This was found to be the case with lanthanum and cerium oxides.[67,69] Other metals have been found to fragment preferentially into stoichiometries not common to the bulk material. Iron oxide is such a case where cluster cations contain FeO,

rather than Fe_2O_3 or Fe_3O_4 commonly found in nature.[66] DFT predictions of structures and relative energies of possible isomers have yielded insight into how clusters relate to bulk phase crystal structures. In the present study, we employ mass–selected photodissociation of small gas phase clusters of uranium oxide to investigate their stability patterns. Computation chemistry is employed to predict the structure, oxidation state, and binding environment of uranium atoms within each cluster.

EXPERIMENTAL

Uranium oxide cluster cations are produced by laser vaporization[72] in a pulsed nozzle source and investigated in a reflectron time–of–flight (RTof) mass spectrometer.[73] The third harmonic (355 nm) of a Spectra–Physics INDI–HG Nd:YAG laser is used to vaporize metal from a rod of depleted uranium metal. A gas mixture containing 3% oxygen in helium is pulsed through a 0.5 mm diameter aperture of a Parker Series 9 valve, and over the rod in the "turbo" block source with an additional half inch growth channel 5 millimeters in diameter as previously described.[71] Ions produced by reaction between the metal plasma and gas are skimmed into a differentially pumped mass spectrometer chamber. Pulsed voltages on the RToF repeller and extractor accelerate ions, and a complement pulsed deflector permits the passage of mass–selected ions. Photodissociation is produced with the third harmonic (355 nm) of a Spectra–Physics GCR–150 Nd:YAG laser operating with a fluence of 1 – 20 mJ/cm^2 . The photodissociation laser intersects the mass–selected ions as they turn around in the reflectron. The resulting fragment ions and unfragmented parent ions are reaccelerated and separated by the reflectron, detected with a Hamamatsu R595 Electron Multiplier Tube, and recorded with the use of a LeCroy LT262 oscilloscope.

Computations were conducted with the Gaussian09 package using the B3LYP exchange–correlation functional.[74] Basis sets of both double and triple zeta quality were used, with aug–cc–pVNZ basis functions on oxygen, and cc–pVNZ–PP basis functions on uranium with the ECP60MDF Stuttgart/Koeln pseudopotential.[54,55] Natural Population Analysis is carried out to determine the degree of localization of the charge and spin. Clustering energies, relative energies and dissociation energies of the cations are calculated for the resulting optimized structures.

RESULTS AND DISCUSSION

The mass spectrum of uranium oxide cluster cations produced by laser vaporization of metallic uranium is shown in Figure 3.1. Each group of peaks correspond to clusters containing the same amount of uranium with varying amounts of oxygen included in the cluster. The labeled peaks except for UO_2^+ all correspond to $(UO_3)_n^+$, and a consistent preference for the formation of a 1:3 ratio of U to O in the ion source. Each group of peaks also feature a peak with only one oxygen fewer than this 1:3 ratio corresponding to $UO_2^+(UO_3)_n$. Clusters with two fewer oxygen than the 1:3 ratio of U:O are absent or of minor intensity. The groups of peaks attributed to one or two uranium atoms clustering with oxygen show alternating intensity with every other peak in clusters containing an excess of oxygen. This is likely caused by clustering of molecular oxygen about a uranium oxide cluster cation. This pattern of alternating intensity is present in heavier clusters, though with an intensity that dies off rapidly with increasing mass. Because clusters in the molecular beam all travel with the same velocity there is a mass dependence on the voltage needed to optimize the deflector, which is used to compensate for molecular beam velocity. This means that while larger clusters than those shown are likely formed, they are more difficult to

detect with regular operating conditions and cannot be mass selected due to poor spatial separation in the region of the mass selector.

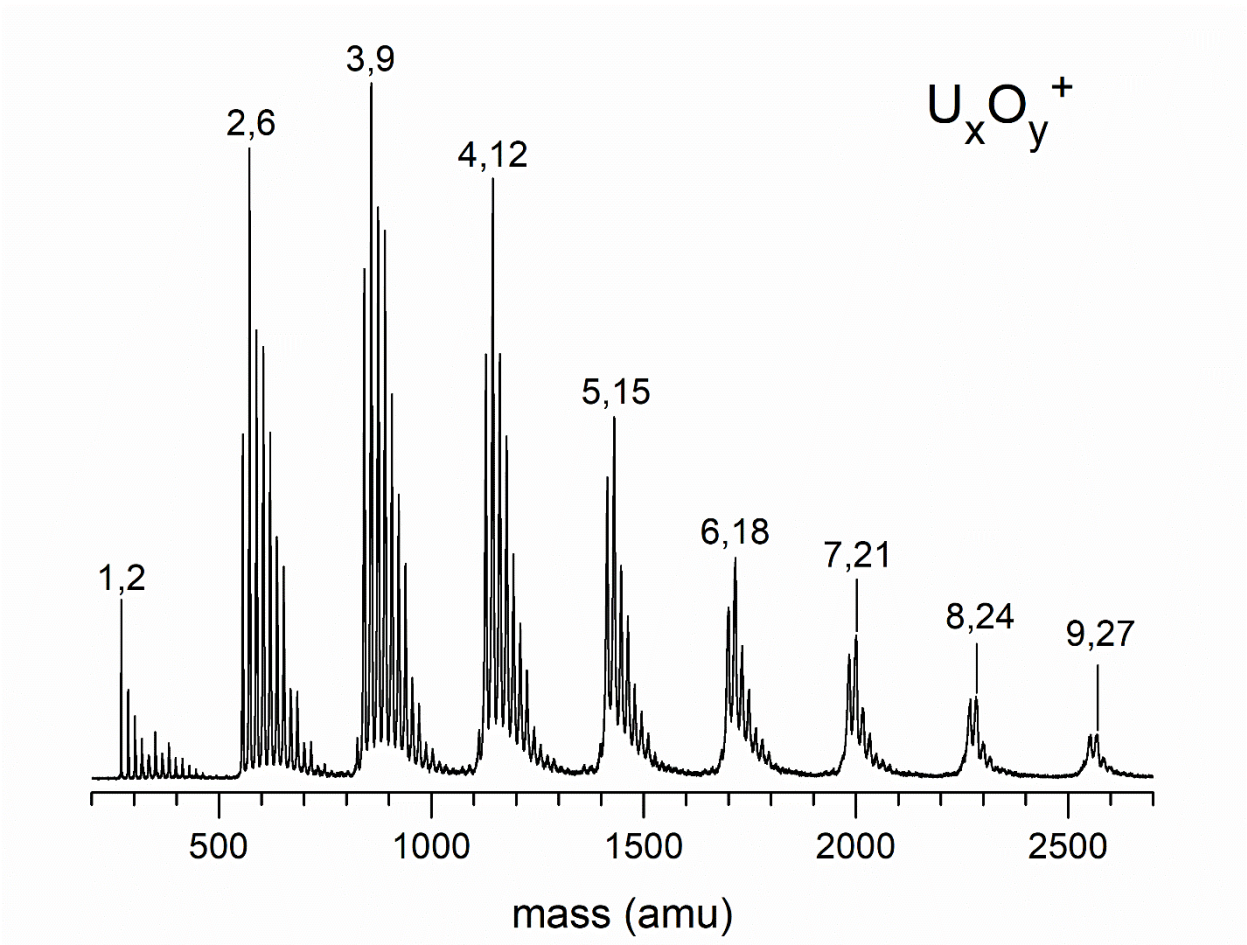

Figure 3.1. Mass spectrum of uranium oxide cluster cations generated using laser vaporization of a uranium metal sample in a supersonic expansion of He seeded with 3% O_2.

Figure 3.2 shows the fragmentation mass spectra obtained by measuring the mass spectrum of a mass–selected ion, and subtracting from it the mass spectrum obtained during photodissociation. Dissociation of these clusters consistently yields UO_2^+, which is also observed as a particularly intense peak in Figure 3.1. This may indicate that U^+ is most stable in the +5 oxidation state. The only other fragment containing just one uranium is UO_3^+ which is only observed as a photofragment of $U_2O_6^+$ by elimination of UO_3 which is known as one stable stoichiometry in the bulk material. Formation of UO_2^+ from $U_2O_6^+$ would require elimination of

UO_4 which may represent a less stable oxidation state, or elimination of UO_3 and atomic oxygen which would require the additional energy required to break a metal oxygen bond. Elimination of atomic oxygen is observed by formation of $U_2O_5^+$ from $U_2O_6^+$. Elimination of two oxygen atoms, most likely in the form of O_2, is observed from $U_2O_7^+$ which also yields $U_2O_5^+$.

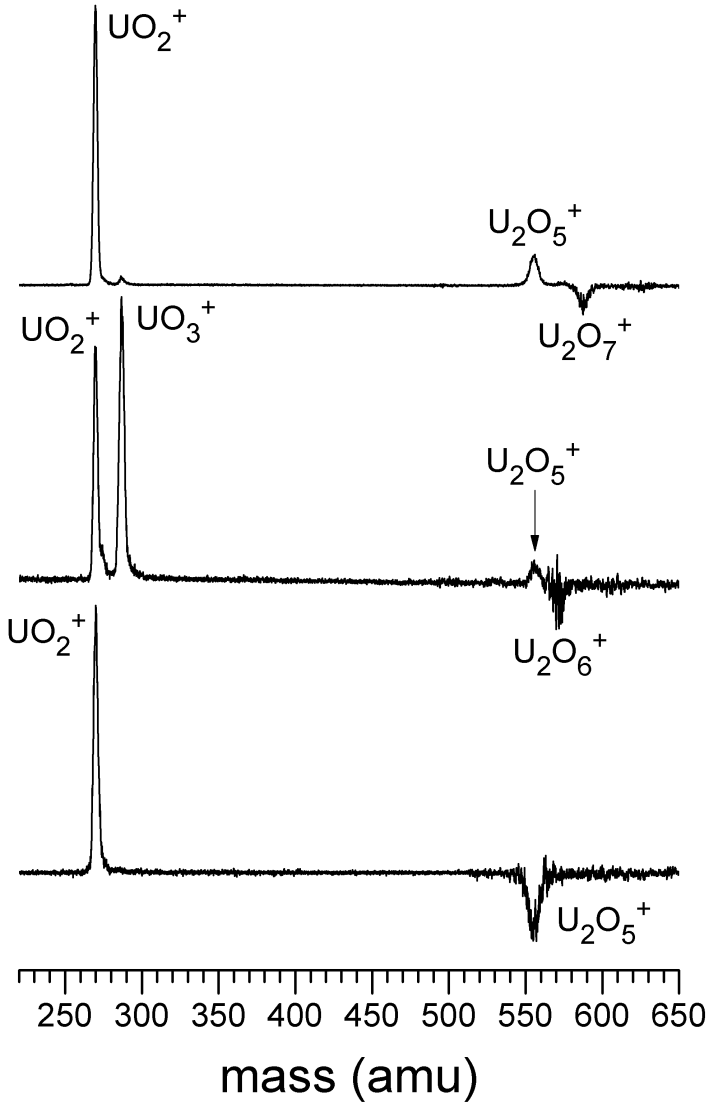

Figure 3.2. Mass spectra showing the photodissociation of $U_2O_7^+$, $U_2O_6^+$, and $U_2O_5^+$ with 355nm light. The negative peaks indicate loss of the parent ion to dissociation, and positive peaks show the production of cationic photofragments. UO_2^+ is seen to form by the photodissociation of all clusters. $U_2O_5^+$ is observed as a low intensity product of the two larger clusters. $U_2O_6^+$ is found to fragment into either UO_2^+ or UO_3^+ upon photodissociation.

Photodissociation mass spectra of clusters containing three uranium are shown in Figure 3.3. Fragmentation of these larger clusters show photofragments consistently differing in mass by UO_3. Elimination of one or two units of UO_3 are found to be the only dissociation pathway for $U_3O_8^+$. This is also true of $U_3O_{10}^+$ with the additional elimination of O_2 to yield $U_3O_8^+$ which then eliminates one or two units of UO_3. It should be noted that the elimination of neutral fragments from a parent cation may be sequential or concerted, yielding one cation and one or more neutral clusters. The eliminated neutral is not detected in this experiment. $U_3O_9^+$ is found to be like $U_2O_6^+$ in not only its 1:3 ratio of U:O but also the presence of fragment cations of the same stoichiometric ratio. $U_3O_9^+$ can eliminate one or two units of UO_3, which gives rise to $U_2O_6^+$ and UO_3^+ which are not observed for the other two parent cations. $U_3O_9^+$ is also seen to eliminate an additional oxygen giving rise to two more intense fragment cations UO_2^+, and $U_2O_5^+$. Exclusive loss of atomic oxygen also yields a low intensity signal for $U_3O_8^+$.

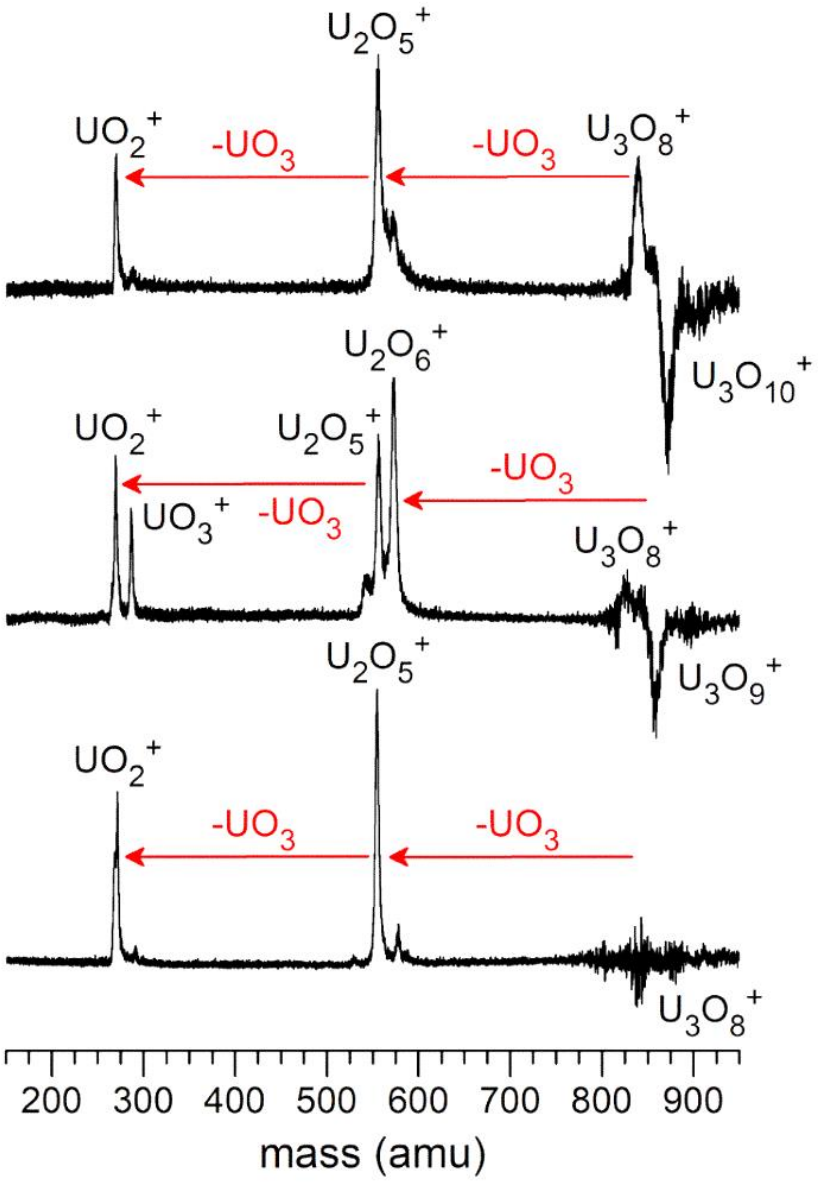

Figure 3.3. Mass spectra showing the photodissociation of $U_3O_{10}^+$, $U_3O_9^+$, and $U_3O_8^+$. $U_3O_8^+$ is found to dissociate almost exclusively by elimination of one or two units of UO_3. $U_3O_{10}^+$ follows this same pattern of losses of UO_3 with the additional elimination of O_2. $U_3O_9^+$ is found to either eliminate one or more units of UO_3, or eliminate cations of the formula $UO_2^+(UO_3)_n$.

The study of larger cluster cations is limited not by the resolving power of the mass spectrometer, but the spatial separation of ions in the region of the mass selector. This is located approximately after one third of the total ion flight path. Because of this, ions containing four or

more uranium are substantially more difficult to mass select. Figure 3.4 shows the fragmentation mass spectra that were obtained for such heavy ions. The mass spectrum of $U_6O_{17}^+$ shows that some ions with one more or fewer oxygen were able to pass the mass selector. These parent ions are observed as negative peaks neighboring the peak indicating loss of $U_6O_{17}^+$. The same is true to a lesser extent for $U_5O_{15}^+$ and $U_4O_{12}^+$ and is evident not by the presence of negative peaks, but broadening of fragment peaks, particularly $U_3O_8^+$.

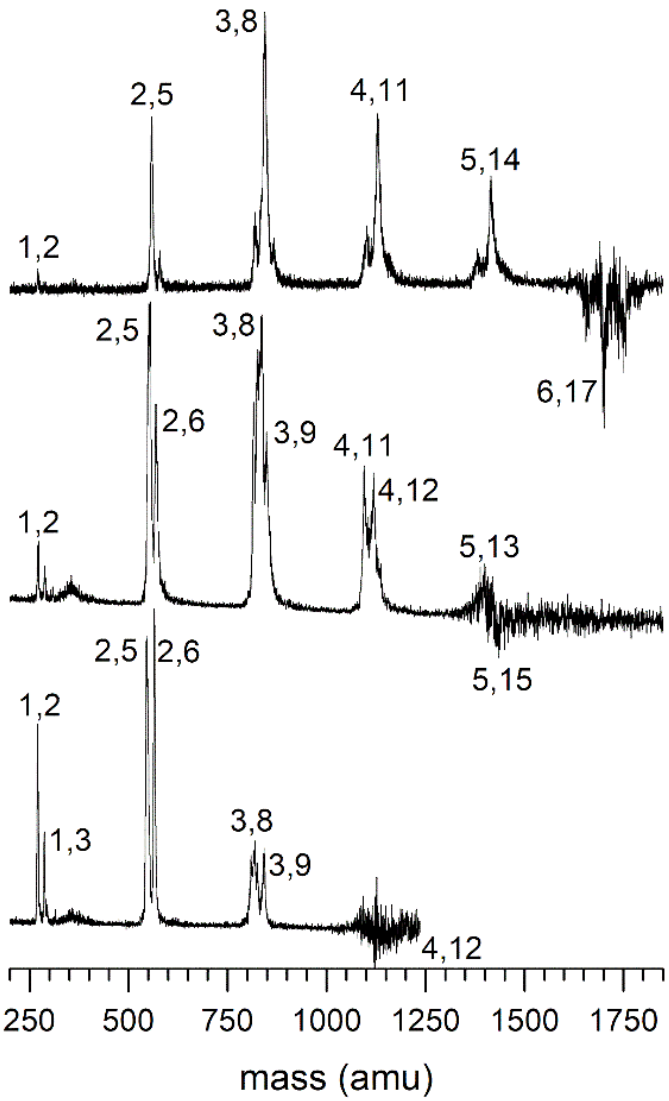

Figure 3.4. Mass spectra showing the photodissociation of $U_6O_{17}^+$, $U_5O_{15}^+$, and $U_4O_{12}^+$. Labels for peaks $U_nO_m^+$ are labeled n,m. $U_6O_{17}^+$, which conforms to the formula $UO_2^+(UO_3)_n$, is found to dissociate only through the elimination of one or more units of UO_3. $U_5O_{15}^+$, and $U_4O_{12}^+$ eliminate either units of UO_3 to form cations, or form cations of the formula $UO_2^+(UO_3)_n$.

The fragmentation pattern observed for $U_6O_{17}^+$ shows nearly exclusive elimination of UO_3 to form ions $UO_2^+(UO_3)$. These fragment ions are observed for clusters containing a 1:3 ratio of U:O such as $U_5O_{15}^+$ and $U_4O_{12}^+$. However, fragmentation of ions containing a 1:3 ratio of U:O also yield $(UO_3)_n^+$ fragments. The presence of both patterns in all fragmentation mass spectra corresponding to $(UO_3)_n^+$ suggests competition between two fragmentation pathways. One fragmentation pathway, observed from all cations studied, leads only to the formation of cations conforming to the formula $UO_2^+(UO_3)_n$, and is likely the result of preferential formation of particularly stable cations. A second pathway is observed only from ions $(UO_3)_n^+$ which yields $(UO_3)_n^+$ by elimination of $(UO_3)_n$. This pattern may result from preferential formation of particularly stable neutrals. This is a strong indication that the formation of undetected $(UO_3)_n$ neutral fragments is energetically favorable. This is also a form of uranium oxide known to be relatively stable as a bulk material in atmospheric conditions, though it should be noted that bulk UO_3 reduces by elimination of O_2 to U_3O_8 upon heating.

Figure 3.5 shows the fragmentation mass spectrum of $U_3O_8^+$ measured with various intensities of the 355 nm photodissociation laser. The relative intensities of UO_2^+ and $U_2O_5^+$ do not vary except at the highest power. Fragment intensity is expected to vary linearly with laser power in the case of single photon absorption. If this were the case the relative intensity of the two fragments would remain the same regardless of laser power.

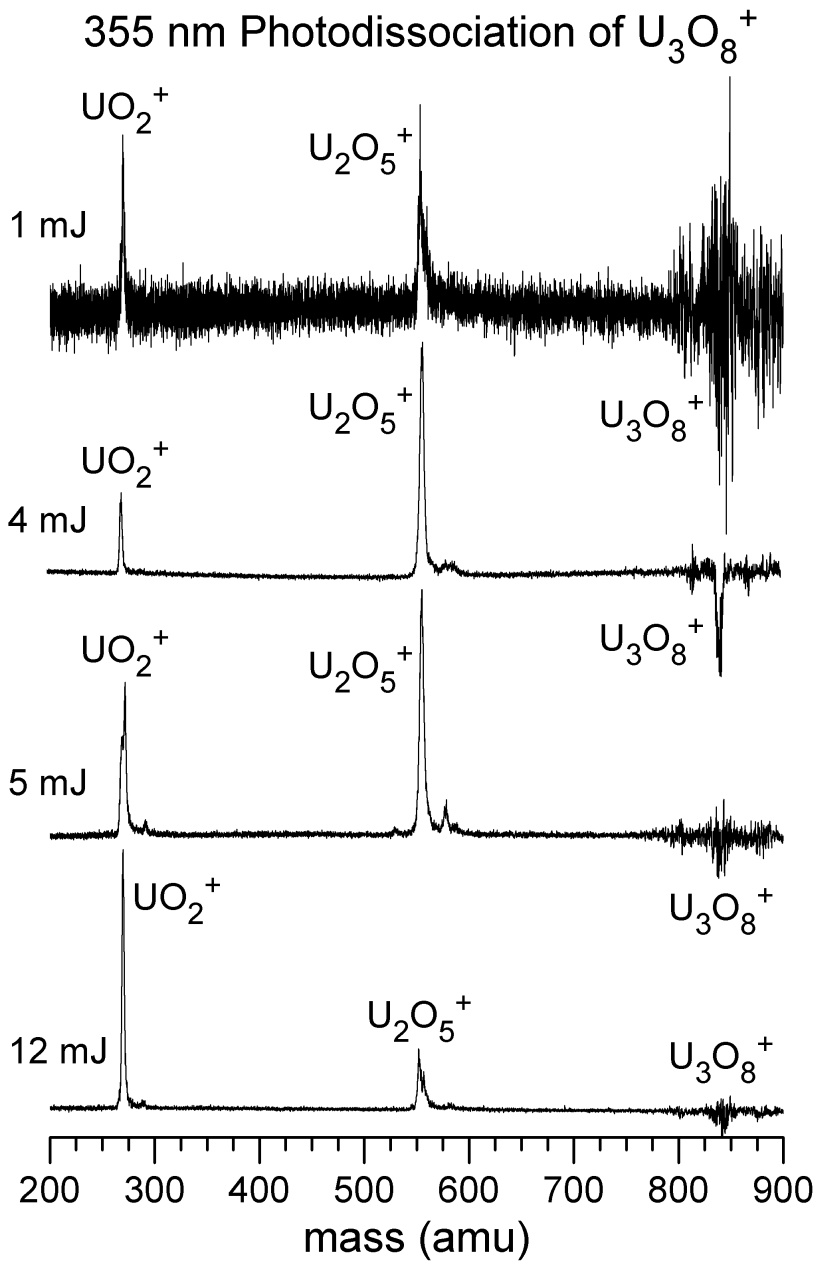

Figure 3.5. Mass spectra showing the photodissociation of $U_3O_8^+$ obtained with various intensities of 355nm laser light. The relative intensities of the two primary fragmentation channels, UO_2^+ and $U_2O_5^+$, varies with laser power in a non–linear manner. This indicates that multiphoton absorption is necessary to cause photodissociation.

Computational studies on those uranium oxide cluster cations observed as abundant photofragments were conducted with the intent of determining both the structure and the localization of charge. While $UO_2^+(UO_3)_n$ clusters are observed directly in the mass

spectrometer, the presence of clusters of $(UO_3)_n$ are implied by the fragmentation patterns of $(UO_3)_n^+$ cluster cations. Figure 3.6 shows the structures of UO_2^+ and UO_3 computed at the B3LYP/aug–cc–pVDZ(O)/cc–pVDZ–PP(U) level of theory for multiple spin states. The low energy spin state for UO_2^+ is predicted to be the doublet, representative of a +5 uranium with two oxygens in the –2 oxidation state. This is structurally similar to the uranyl ion with the addition of an electron to the *f*–orbitals of uranium. UO_3 is predicted to be in a singlet ground state with two closely bonded oxygens in axial positions forming a uranyl–like structure, which is bound to a third equatorial oxygen at longer distance.

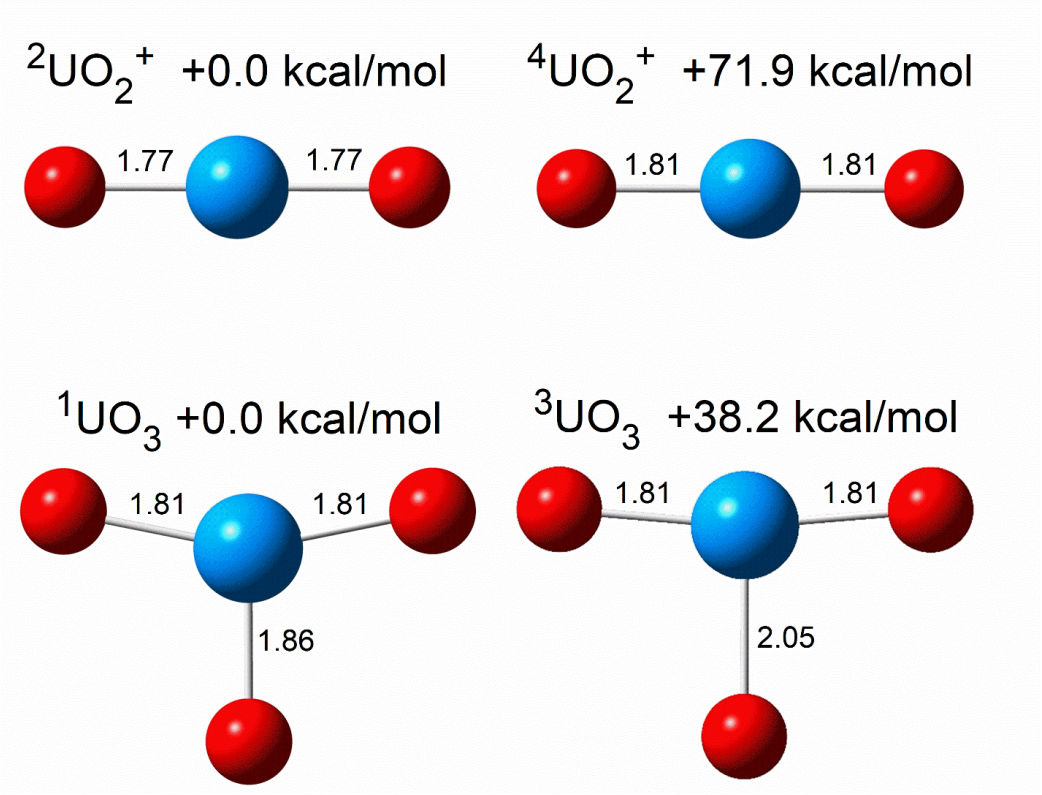

Figure 3.6. Calculated structures of $^2UO_2^+$, $^4UO_2^+$, $^1UO_3$, and $^3UO_3$.

Figure 3.7 shows two predicted structures of $U_2O_5^+$ and U_2O_6 in the doublet and singlet states respectively. These spin states are predicted to be most stable by approximately 50 kcal/mol for these and larger clusters. $U_2O_5^+$ is shown to have stable C_s and C_{2v} isomers,

however the C_s isomer is 18 kcal/mol lower in energy. NBO calculations show that this isomer carries its charge entirely in the f–orbitals on the uranium in an asymmetric U–O bonding environment. U_2O_6 is predicted to have a high symmetry D_{2h} structure. Each uranium exhibits short bonds to two axial oxygens creating a uranyl ion, that is then bound to the other uranyl ion through longer U–O bonds to bridging oxygens.

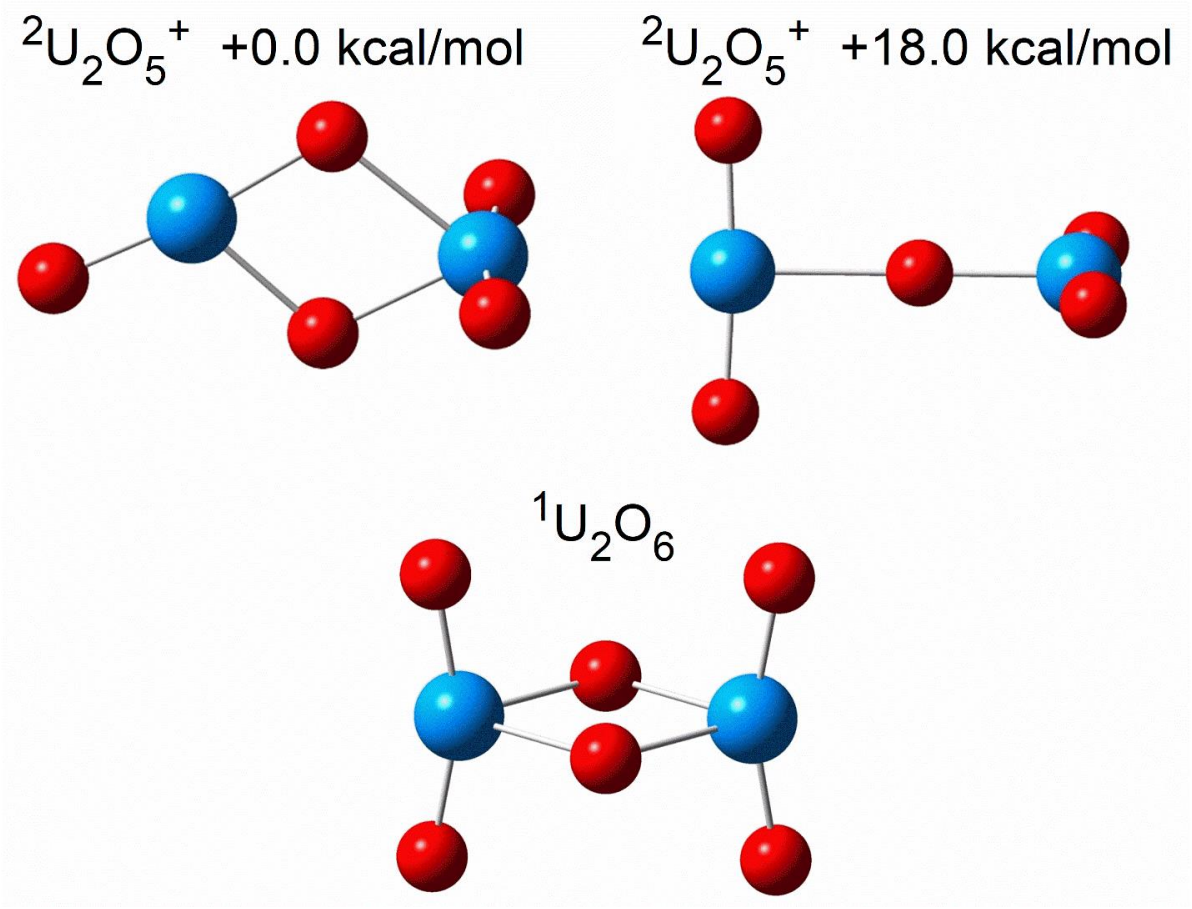

Figure 3.7. Calculated structures for two isomers of $U_2O_5^+$ and one of U_2O_6. In the low energy isomer of $U_2O_5^+$ spin and presumably charge are predicted to be localized to an unpaired electron in the *f*–orbitals of the uranium in the asymmetric environment. The unpaired electron is found on the leftmost uranium in both isomers of $U_2O_5^+$.

Figure 3.8 shows the predicted structures of $U_3O_8^+$ and U_3O_9 in both ring and chain isomers. The ring isomer of $U_3O_8^+$ includes two uranium in uranyl structures and one asymmetrically bound uranium that carries the charge in its *f*–orbitals. The ring isomer of U_3O_9

does not contain this asymmetric charge center, and instead consists of three uranyl ions bound through three bridging oxygens. The two chain isomers shown are both predicted to be higher in energy.

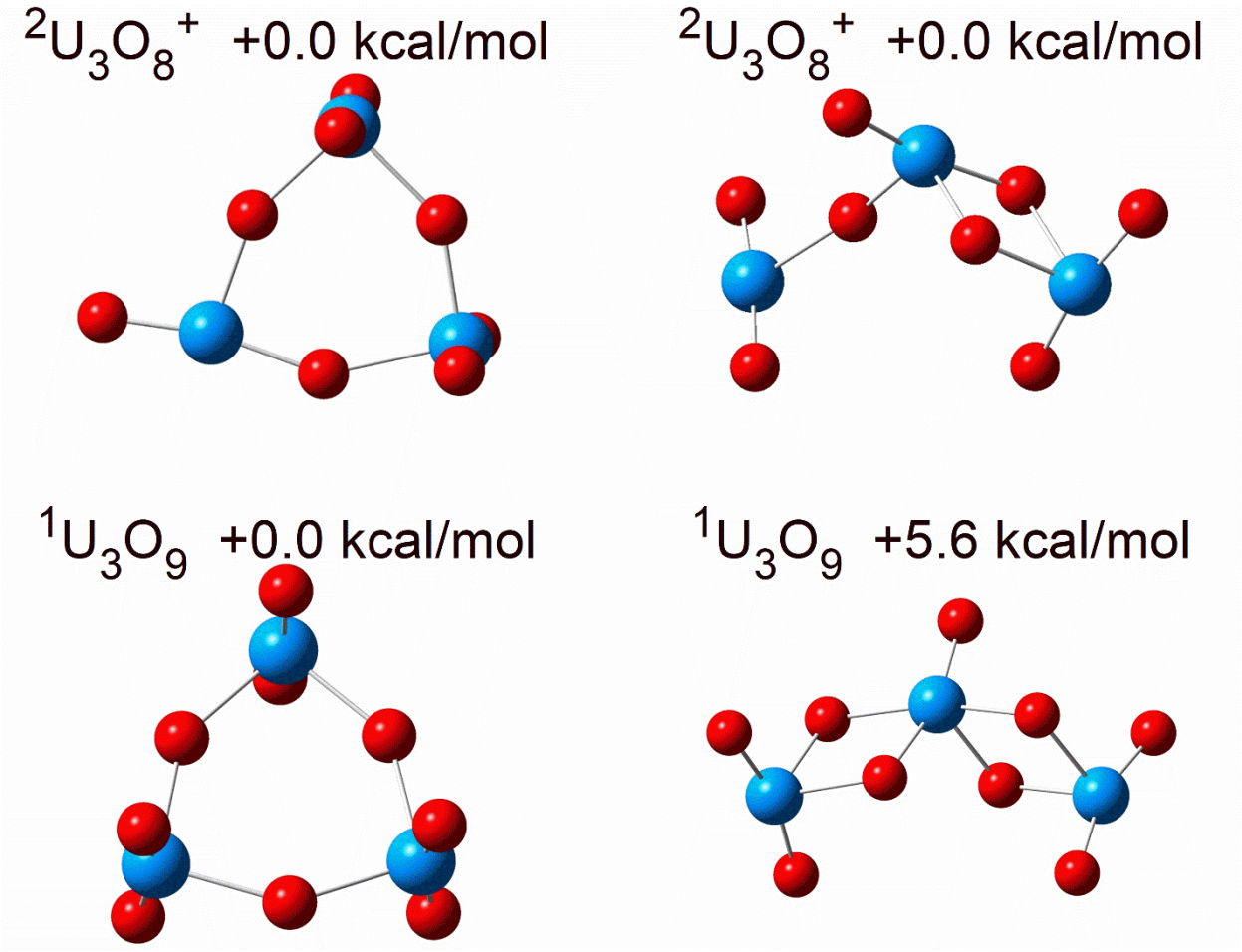

Figure 3.8. Calculated structures for two isomers of $U_3O_8^+$ and two isomers of U_3O_9. The unpaired electron is found on the leftmost uranium in both isomers of $U_3O_8^+$.

Figure 3.9 shows the lowest energy isomers predicted for $U_4O_{11}^+$ and U_4O_{12}. $U_4O_{11}^+$ is predicted to be most stable in a cage isomer, while the chain isomer is 4.9 kcal/mol higher in energy. The cage isomer includes two uranium in the uranyl configuration, while the charge is still carried in the *f*–orbitals of the asymmetrically bound uranium. The two isomers of U_4O_{12} presented differ only by 0.2 kcal/mol which is well below the error of this level of theory. Both

structures are symmetric, the chain is C_i and the ring is D_{4h}. These two structures differ significantly in the presence of uranyl units within the larger structure. The ring isomer is composed entirely of uranyl ions binding through equatorial bridging oxygens. The ends of the chain isomer both exhibit uranyl structures but the central two uranium atoms are strongly bound to only one oxygen with four longer bonds to bridging oxygens. This allows the central two uranium to maintain the preferred +6 oxidation state while binding to five different oxygen atoms.

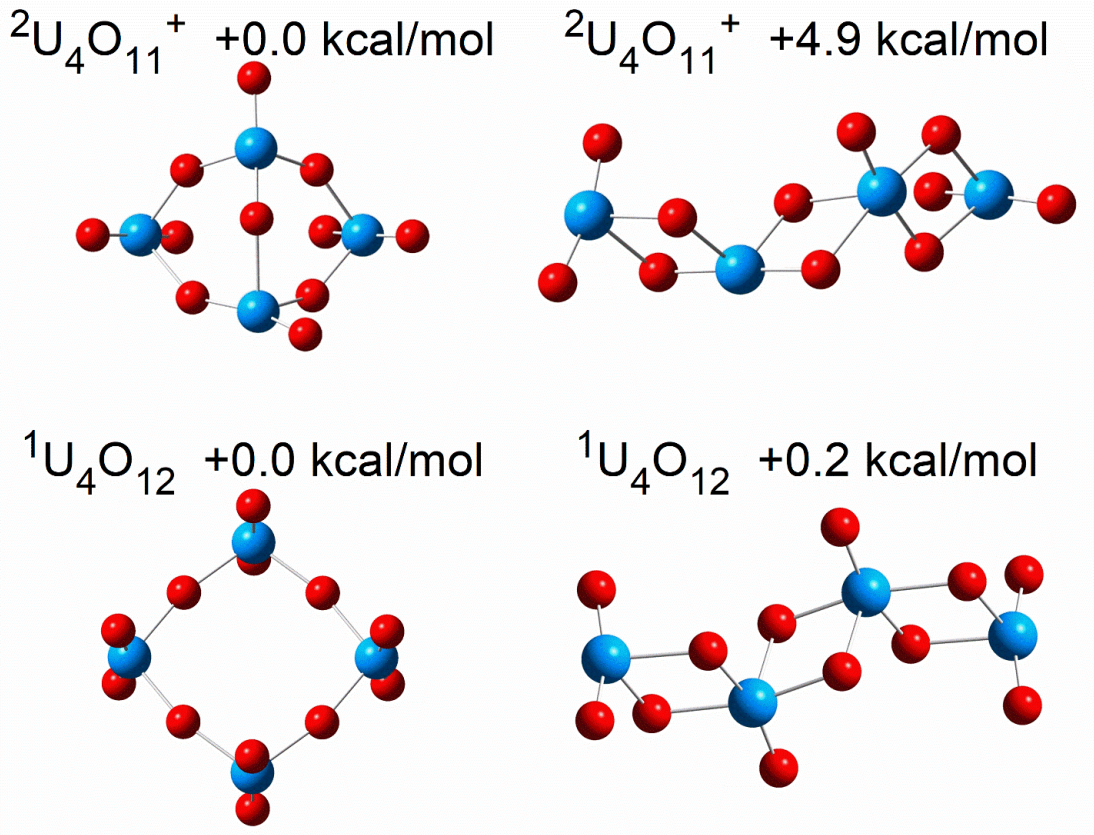

Figure 3.9. Calculated structures for two isomers of $U_4O_{11}^+$ and two isomers of U_4O_{12}. The low energy isomer of $U_4O_{11}^+$ contains an unpaired electron on the lowest uranium atom, while in the higher energy isomer the unpaired electron is on the second leftmost uranium.

In all presented structures, U–O bonds are found to fall into two distinct categories. Some oxygens are doubly bound in axial positions on uranium; in uranyl ions two such oxygens are present. Other oxygens form single bonds in equatorial positions to bridge two uranium atoms.

The predicted bond energies of these types of bonds for the structures presented are shown in Table 3.1. These values were computed with using CCSD(T) and CBS extrapolation with pseudopotentials and the third order Douglass–Kroll–Hess Hamiltonian as computational expense allowed. The bond energies for oxygen in axial positions were assumed to be constant regardless of cluster size past the structures containing only one uranium. While the bond energies for the axial doubly bonded oxygens are found to be near 175 kcal/mol for these small clusters, the U–O single bonds are found to vary between 80 and 105 kcal/mol.

Table 3.1. Average U–O Bond Dissociation Energy in kcal/mol calculated at the B3LYP/aug–cc–pVDZ–PP level of theory. Higher accuracy ab initio calculations were included as computational expense allowed. Binding energies for equatorial oxygen were calculated assuming that the axial bond energy values are constant.

Molecule	**U–O Position**	**Highest level**	**Average BDE**
$^{1}UO_3 \rightarrow {}^{3}UO_2 + {}^{3}O$	Equatorial	CBS–PP	146.6
		CBS–dk3	147.7
		DFT	135.1
	Axial	CBS–PP	174.7
		CBS–dk3	174.2
		DFT	180.5
$^{3}UO_2$ ($D_{\infty h}$)	Axial	CBS–PP	174.7
		CBS–dk3	174.2
		DFT	180.5
$^{2}UO_2^{+}$($D_{\infty h}$)	Axial	CBS–PP	173.5
		CBS–dk3	173.3
		DFT	182.0
$^{3}U_2O_5$(C_s)	Equatorial	CCSD(T)/aT	102.2
		DFT	82.8
$^{2}U_2O_5^{+}$(C_{2v})	Equatorial	CCSD(T)/aT	99.1
		DFT	90.0
$^{2}U_2O_5^{+}$(C_s)	Equatorial	CCSD(T)/aT	101.9
		DFT	97.2

$^1U_2O_6$	Equatorial	CBS–PP	93.9
		DFT	85.3
$^2U_3O_8^+(C_1)$	Equatorial	DFT	90.9
$^2U_3O_8^+(C_s)$	Equatorial	DFT	93.1
$^1U_3O_9(C_{2v})$	Equatorial	CCSD(T)/aT	98.7
$^2U_4O_{11}^+$(chain)	Equatorial	DFT	104.0
$^2U_4O_{11}^+$(ring)	Equatorial	DFT	104.6
		DFT	89.1
$^1U_4O_{12}(D_{4h})$	Equatorial	CCSD(T)/aD	99.6
		DFT	89.5
$^1U_4O_{12}(C_i)$	Equatorial	CCSD(T)/aD	100.8
		DFT	89.7
$^1U_5O_{15}(D_{5h})$	Equatorial	DFT	95.3
$^1U_5O_{15}(C_s)$	Equatorial	DFT	95.7
$^2U_6O_{17}^+$(cage)	Equatorial	DFT	96.2
$^2U_6O_{17}^+$(cage)	Equatorial	DFT	95.9
$^2U_6O_{17}^+$(chain)	Equatorial	DFT	92.9

Table 3.2 shows the calculated dissociation energy required for clusters to eliminate UO_3 or dissociate completely to UO_3. One photon of 355 nm light contains 81 kcal/mol, which is enough to eliminate only one UO_3 from several of the studied clusters. In Figure 3.5 a change in the relative intensities of the two fragments is observed with increasing laser power. This may be attributed to an increase in the probability of multiphoton absorption with increasing laser power. The ionization potential is also expected to decrease as clusters grow larger, and the charge would be expected to remain on the fragment with the lowest ionization potential. This means the formation of U_2O_6 would require the input of additional energy equal to the difference in IP of U_2O_6 and UO_3. When $U_3O_8^+$ dissociates to yield UO_2^+ may also eliminate 2(UO_3) or

U_2O_6. Both dissociation pathways would require multiple photons of 355 nm light and is still observed with as little as 1 mJ per pulse of light.

Table 3.2. Dissociation energies for lowest energy spin states calculated at the B3LYP/aug–cc–pVDZ(O)/cc–pVDZ–PP(U) level of theory.

Reaction	**ΔH_{298K} (kcal/mol)**
$U_2O_6(D_{2h}) \rightarrow 2UO_3$	71.1
$U_2O_5^+(C_s) \rightarrow UO_3 + UO_2^+$	71.7
$U_2O_5^{2+}(D_{2d}) \rightarrow UO_3 + UO_2^{2+}$	139.1
$U_3O_8^+(C_s) \rightarrow UO_3 + U_2O_5^+(C_s)$	62.5
$U_3O_8^{2+}(D_{2h}) \rightarrow UO_3 + U_2O_5^{2+}(D_{2d})$	95.7
$U_3O_9(C_1) \rightarrow 3UO_3$	123.7
$U_3O_9(C_{2v}) \rightarrow 3UO_3$	129.0
$U_4O_{12}(C_i) \rightarrow 4UO_3$	176.9
$U_4O_{12}(D_{4h}) \rightarrow 4UO_3$	175.7
$U_4O_{11}^+(C_1) \rightarrow UO_3 + U_3O_8^+(C_s)$	71.9
$U_4O_{11}^{2+}(C_1) \rightarrow UO_3 + U_3O_8^{2+}(D_{2h})$	84.0
$U_5O_{15}(C_s) \rightarrow 5UO_3$	223.5
$U_5O_{15}(D_{5h}) \rightarrow 5UO_3$	219.6
$U_5O_{14}^{2+}(C_2) \rightarrow UO_3 + U_4O_{11}^{2+}(C_1)$	32.9
$U_6O_{18}(C_i) \rightarrow 6UO_3$	281.6

CONCLUSIONS

Uranium oxide cluster cations were produced by laser vaporization of depleted uranium in an oxygen seeded helium supersonic expansion. While clusters with substantially more oxygen than $(UO_3)_n^+$ were also produced, the only clusters containing less oxygen were of the stoichiometry $UO_2^+(UO_3)_n$. Mass spectrometry of the resulting cluster cations showed that $(UO_3)_n^+$ were most intense. Mass–selected photodissociation showed that all clusters produce $UO_2^+(UO_3)_n$ as photofragments. The exclusive formation of $UO_2^+(UO_3)_n$ from most studied

clusters indicates that this formula represents the most stable form of uranium oxide cluster cations. Only $(UO_3)_n^+$ parent clusters photodissociate to yield clusters of different stoichiometry, namely $(UO_3)_n^+$ photofragments. The consistent spacing of UO_3 between observed photofragments, and the preferred elimination of $(UO_3)_n$ from $(UO_3)_n^+$ is a strong indication that $(UO_3)_n$ is the stable stoichiometry of neutral uranium oxide clusters. B3LYP/aug–cc–pVDZ–PP calculations indicate that the structures of the observed cation photofragments contain a uranium atom in the +5 oxidation state that carries the charge and spin in the *5f*–orbital. The rest of the cluster is composed of +6 uranium in the form of UO_2^{2+} bonding to two additional bridging oxygens. Ion mobility could be used in future studies to verify the proposed structures. Furthermore, photoionization could potentially be used to detect the eliminated neutral clusters and investigate if they are $(UO_3)_n$ as suggested by the observed mass loss on photodissociation.

AUTHOR INFORMATION

Corresponding author: Email: maduncan@uga.edu

ACKNOWLEDGEMENTS

We gratefully acknowledge the generous support for this work from the U.S. Department of Energy via Grant No. DESC0018835 (MAD) and from the Air Force Office of Scientific Research through grant RUSDE0000929001 and DOE Grant No. DE–SC0018921 (DAD) for the computational work. D.A.D. also thanks the Robert Ramsay Fund at The University of Alabama.

SUPPORTING INFORMATION AVAILABLE: Additional mass spectra and further details of the computations are available free of charge via at http://pubs.acs.org.[75]

REFERENCES

1. Katz, J. J.; Rabinowitch, E. *The Chemistry of Uranium the Element, Its Binary and Related Compounds*; Dover Publications, Inc.: New York, **1961**.
2. Katz, J. J.; Seaborg, G. T.; Morss, L. R. *The Chemistry of the Actinide Elements, 2nd ed*; Chapman and Hall: London, **1986**.
3. Cotton, S. *Lanthanide and Actinide Chemistry*; John Wiley & Sons, Ltd.: Chichester, **2006**.
4. Lottermoser, B. *Mine Wastes: Characterization, Treatment and Environmental Impact*; Springer: London, **2007**.
5. Klein, C.; Dutrow, B. *Manual of Mineral Science*; John Wiley & Sons: United States of America, **2008**.
6. Morris, D. E.; Allen, P. G.; Berg, J. M.; Chisholm–Brause, C. J.; Conradson, S. D.; Donohoe, R. J.; Hess, N. J.; Musgrave, J. A.; Tait, C. D. Speciation of Uranium in Fernald Soils by Molecular Spectroscopic Methods: Characterization of Untreated Soils. *Environ. Sci. Technol.* **1996**, *30*, 2322–2331.
7. Maher, K.; Bargar, J. R.; Brown, G. E., Jr. Environmental Speciation of Actinides. *Inorg. Chem.* **2013**, *52*, 3510–3532.
8. Potocki, M.; Mayewski, P. A.; Kurbatov, A. V.; Simoes, J. C.; Dixon, D. A.; Goodwin, I.; Carleton, A. M.; Handley, M. J.; Jana, R.; Korotkikh, E. V. Recent Increase in Antarctic Peninsula Ice Core Uranium Concentrations. *Atmospheric Environ.* **2016**, *140*, 381–385.
9. Steinhauser, G. Anthropogenic Radioactive Particles in the Environment. *J. Radioanal. Nucl. Chem.* **2018**, *318*, 1629–1639.

10. Reynolds, J. G.; Cooke, G. A.; Page, J. S.; Warrant, R. W. Uranium–Bearing Phases in Hanford Nuclear Waste. *J. Radioanal. Nucl. Chem.* **2018**, *316*, 289–299.

11. Heaven, M. C.; Nicolai, J.–P.; Riley, S. J.; Parks, E. K. Rotationally Resolved Electronic Spectra for Uranium Monoxide. *Chem. Phys. Lett.* **1985**, *119*, 229–233.

12. Kaledin, L. A.; McCord, J. E.; Heaven, M.C. Laser Spectroscopy of UO: Characterization and Assignment of States in the 0– to 3–eV Range, with a Comparison to the Electronic Structure of ThO. *J. Mol. Spec.* **1994**. *164*. 27–65.

13. Kaledin, L. A.; Heaven M. C. Electronic Spectroscopy of UO. *J. Mol. Spec.* **1997**. *185*. 1–7.

14. Lue, C. J.; Jin, J.; Ortiz, M. J.; Rienstra–Kiracofe, J. C.; Heaven M. C. Electronic Spectroscopy of UO_2 Isolated in a Solid Ar Matrix. *J. Am. Chem. Soc.* **2004**, *126*, 1812–1815.

15. Han, J.; Goncharov, V.; Kaledin, L. A.; Komissarov, A. V.; Heaven, M. C. Electronic Spectroscopy and Ionization Potential of UO_2 in the Gas Phase. *J. Phys. Chem.* **2004**, *120*, 5155.

16. Gagliardi, L.; Heaven, M. C.; Krogh, J. W.; Roos, B. O. The Electronic Spectrum of the UO_2 Molecule. *J. Am. Chem. Soc.* **2005**, *127*, 86–91.

17. Goncharov, V.; Kaledin, L. A.; Heaven, M. C. Probing the Electronic Structure of UO^+ with High–Resolution Photoelectron Spectroscopy. *J. Chem. Phys.* **2006**, *125*, 133202.

18. Heaven, M. C.; Probing Actinide Electronic Structure using Fluorescence and Multi–Photon Ionization Spectroscopy. *Phys. Chem. Chem. Phys.* **2006**. *8*. 4497–4509.

19. Merritt, J. M.; Han, J.; Heaven M. C. Sectroscopy of the UO_2^+ Cation and the Delayed Ionization of UO_2. *J. Chem. Phys.* **2008**, *128*, 084304.

20. Gutowski, K. E.; Cocalia, V. A.; Griffin S. T.; Bridges, N. J.; Dixon, D. A.; Rogers, R. D. Interactions of 1–Methylimidazole with $UO_2(CH_3CO_2)_2$ and $UO_2(NO_3)_2$: Structural, Spectroscopic, and Theoretical Evidence for Imidazole Binding to the Uranyl Ion. *J. Am. Chem. Soc.* **2007**, *129*, 526–536.

21. Wang, X. F.; Andrews, L.; Thanthiriwatte, K. S.; Dixon, D. A. Infrared Spectra of H_2ThS and H_2US in Noble Gas Matrixes: Enhanced H–An–S Covalent Bonding. *Inorg. Chem.* **2013**, *52*, 10275–10285.

22. Andrews, L.; Cho, H. G.; Thanthiriwatte, K. S.; Dixon, D. A. Thorium and Uranium Hydride Phosphorus and Arsenic Bearing Molecules with Single and Double Actinide–Pnictogen and Bridged Agnostic Hydrogen Bonds. *Inorg. Chem.* **2017**, *56*, 2949–2957.

23. Wacker, J. N.; Vasiliu, M.; Huang, K.; Baumbach, R. E.; Bertke, J. A.; Dixon, D. A.; Knope, K. E. Uranium(IV) Chloride Complexes: UCl_6^{2-} and an Unprecedented $U(H_2O)_4Cl^{4-}$ Structural unit. *Inorg. Chem.* **2017**, *56*, 9772–9780.

24. Fang, Z. T.; Garner, E. B.; Dixon, D. A.; Gong, Y.; Andrews, L.; Liebov, B. Laser–Ablated U Atom Reactions with CN_2 to Form UNC, $U(NC)_2$, and $U(NC)_2$: Matrix Infrared Spectra and Quantum Chemical Calculations. *J. Phys. Chem. A* **2018**, *122*, 516–528.

25. Dietz, T. G.; Duncan, M. A.; Smalley, R. E.; Cox, D. M.; Horsley, J. A.; Kaldor, A. Spectral Narrowing and Infrared–Laser Fragmentation of Jet–Cooled $UO_2(hfaa)_2$ TMP and $UO_2(hfaa)_2$ THF: Volatile Uranyl Compounds. *J. Chem. Phys.* **1982**, *77*, 4417–4426.

26. Pillai, E. D.; Molek, K. S.; Duncan, M. A. Growth and Photodissociation of $U^+(C_6H_6)_n$ (n=1–3) and $UO_m^+(C_6H_6)$ (m=1, 2) Complexes. *Chem. Phys. Lett.* **2005**, *405*, 247–251.

27. Ricks, A. M.; Gagliardi, L.; Duncan, M. A. Infrared Spectroscopy of Extreme Coordination: The Carbonyls of U^+ and UO_2^+. *J. Am. Chem. Soc.* **2010**, *132*, 15905–15907.

28. Ricks, A. M.; Gagliardi, L.; Duncan, M. A. Uranium Oxo and Superoxo Cations Revealed Using Infrared Spectroscopy in the Gas Phase. *J. Phys. Chem. Lett.* **2011**, *2*, 1662–1666.

29. Allen, G. C.; Holmes, N. R.; Mixed–Valency Behavior in some Uranium–Oxides Studies by X–Ray Photoelectron Spectroscopy. *Can. J. Spectrosc.* **1993**, *38*, 124–130.

30. Heinemann, C.; Cornehl, H. H.; Schwarz H. Hydrocarbon Activation by "Bare" Uranium Cations: Formation of a Cationic Uranium–Benzene Complex from Three Ethylene Units. *J. Organomet. Chem.* **1995**, *501*, 201–209.

31. Cornehl, H. H.; Wesendrup, R.; Diefenbach, M.; Schwarz, H. A Comparitive Study of Oxo–Ligand Effects in the Gas–Phase Chemistry of Atomic Lanthanide and Actinide Cations. *Chem. Eur. J.* **1997**, 3, 1083–1090

32. Jackson, G. P.; Gibson, J. K.; Duckworth, D. C. Gas–Phase Reactions of Bare and Oxo–Ligated Actinide and Lanthanide Cations with Pentamethylcyclopentadiene Studied in a Quadrupole Ion Trap Mass Spectrometer. *Int. J. Mass. Spectrom.* **2002**, *220*, 419–441.

33. Jackson, G. P.; King, F. L.; Goeringer, D. E.; Duckworth, D. C. Gas–Phase Reactions of U^+ and U^{2+} with O_2 and H_2O in a Quadrupole Ion Trap. *J. Phys. Chem. A* **2002**, *106*, 7788–7794.

34. Gibson, J. K. Gas–Phase Chemistry of Actinide Ions: Probing the Distinctive Character of the 5f Elements. *Int. J. Mass Spectrom.* **2002**, *214*, 1–21.

35. Rios, D.; Gibson, J. K. Activation of Gas Phase Uranyl Diacetone Alcohol Coordination Complexes by Spectator Ligand Addition. *Eur. J. Inorg. Chem.* **2012**, *2012*, 1054–1060.

36. Van Stipdonk, M. J.; del Carmen Michelini, M.; **Plaviak, A.; Martin, D.;** Gibson, J. K. Formation of Bare UO_2^{2+} and NUO^+ by Fragmentation of Gas–Phase Uranyl–Acetonitrile Complexes. *J. Phys. Chem. A,* **2014**, *118*, 7838–7846.

37. de Jong, W. A.; Dau, P.; Wilson, R.; Marçalo, J.; Van Stipdonk, M. J.; Corcovilos, T.; Berden, G.; Martens, J.; Oomens, J.; Gibson, J. K. Revealing Disparate Chemistries of Protactinium and Uranium. Synthesis of the Molecular Uranium Tetroxide Anion, UO^{4-}. *Inorg. Chem*. **2017**, *56*, 3686–3694.

38. Groenewold, G. S.; Van Stipdonk, M. J.; Gresham, G. L.; Chien, W.; Bulleigh, K.; Howard, A. CID MS/MS of Desferrioxamine Siderophore Complexes from ESI of UO_2^{2+}, Fe^{3+} and Ca^{2+} Solutions. *J. Mass Spectrom.* **2004**, *39*, 752–761.

39. Groenewold, G. S.; Cossel, K. C.; Gresham, G. L.; Gianotto, A. K.; Appelhans, A. D.; Olson, J. E.; Van Stipdonk, M. J.; Chien, W. Binding of Molecular O_2 to Di– and Tri–Ligated $[UO_2]^+$. *J. Am. Chem. Soc.* **2006**, *128*, 3075–3084.

40. Groenewold, G. S.; Gianotto, A. K.; Cossel, K. C.; Van Stipdonk, M. J.; Moore, D. T.; Polfer, N.; Oomens, J.; de Jong, W. A.; Visscher, L. Vibrational Spectroscopy of Mass Selected $[UO_2(ligand)_n]^{2+}$ Complexes in the Gas Phase: Comparison with Theory. *J. Am. Chem. Soc.* **2006**, *128*, 4802–4813.

41. Groenewold, G. S.; Oomens, J.; de Jong, W. A.; Gresham, G. L.; McIlwain, M. E.; Van Stipdonk, M. J.; Vibrational Spectroscopy of Anionic Nitrate Complexes of UO_2^{2+} and Eu^{3+} Isolated in the Gas Phase. *Phys. Chem. Chem. Phys.* **2008**, *10*, 1192–1202.

42. Groenewold, G. S.; van Stipdonk, M. J.; Oomens, J. de Jong, W. A.; McIlwain, M. E. The Gas–Phase Bis–Uranyl Nitrate Complex $[(UO_2)_2(NO_3)_5]^-$: Infrared Spectrum and Structure. *Int. J. Mass Spectrom*. **2011**, *308*, 175–180.

43. Groenewold, G. S.; van Stipdonk, M. J.; Oomens, J.; de Jong, W. A.; Gresham, G. L.; McIlwain, M. E. Vibrational Spectra of Discrete UO_2^{2+} Halide Complexes in the Gas Phase. *Int. J. Mass Spectrom*. **2010**, *297*, 67–75.

44. Van Stipdonk, M. J.; Hanley, C.; **Perez, E.; Pestok, J.;** Mihm, P.; Corcovilos, T. A. Collision–Induced Dissociation of Uranyl–Methoxide and Uranyl–Ethoxide Cations: Formation of UO_2H^+ and Uranyl–Alkyl Product Ions. *Rapid Comm. Mass Spectrom.* **2016**, *30*, 1879–1890.

45. Tanner, S. D.; Li, C.; Vais, V.; Baranov, V. I.; Bandura, D. R. Chemical Resolution of Pu^+ from U^+ and Am^+ Using Band–Pass Reaction Cell Inductively Coupled Plasma Spectrometer. *Anal. Chem.* **2004**, *76*, 3042–3048.

46. Vent–Schmidt, T.; Andrews, L.; Thanthiriwatte, K. S.; Dixon, D. A.; Riedel, S. Reaction of Laser–Ablated Uranium and Thorium Atoms with H_2Se: A Rare Example of Selenium Multiple Bonding. *Inorg. Chem.* **2015**, *54*, 9761–9769.

47. Forbes, T. P.; Szakal, C. Considerations for Uranium Isotope Ratio Analysis by Atmospheric Pressure Ionization Mass Spectrometry. *Analyst.* **2018**, *144*, 317–323.

48. de Jong, W. A.; Harrison, R. J.; Nichols, J. A.; Dixon, D, A. Fully Relativistic Correlated Benchmark Results for Uranyl and a Critical Look at Relativistic Effective Core Potentials for Uranium. *Theor. Chem. Acc.* **2001**, *107*, 22–26.

49. Haiges, R.; Vasiliu, M.; Dixon, D. A.; Christe, K. O.; The Uranium(VI) Oxoazides $[UO_2(N_3)_2 \cdot CH_3CN]$, $[(bipy)_2(UO_2)_2(N_3)_4]$, $[(bipy)UO_2(N_3)_3]^-$, $[UO_2(N_3)_4]^{2-}$, and $[(UO_2)_2(N_3)_8]^{4-}$. *Chem. Eur. J.* **2016**, *23*, 652–664.

50. Flores, L. A.; Murphy, J. G.; Copeland, W. B.; Dixon, D. A. Reaction of CO_2 with UO_3 Nanoclusters. *J. Phys. Chem. A* **2017**, *121*, 8518–8524.

51. del Carmen Michelini, M.; Russo, N.; Sicilia, E. How Can Uranium Ions (U^+, U^{2+}) Activate the O–H Bond of Water in the Gas Phase? *Angew. Chem.* **2006**, *45*, 1095–1099.

52. del Carmen Michelini, M.; Russo, N.; Sicilia, E. Gas–Phase Chemistry of Actinides Ions: New Insights into the Reaction of UO^+ and UO^{2+} with Water. *J. Am. Chem. Soc.* **2007**, *129*, 4229–4239.

53. Odoh, S. O.; Govind, N.; Schreckenbach, G.; de Jong, W. A. Cation–Cation Interactions in $[(UO_2)_2(OH)_n]^{4-n}$ Complexes. *Inorg. Chem.* **2013**, *52*, 11269–11279.

54. Dolg, M.; Cao, X.; Accurate Relativistic Small–Core Pseudopotentials for Actinides. Energy Adjustments for Uranium and First Applications to Uranium Hydride. *J. Phys. Chem. A* **2009**, *113*, 12573–12581.

55. Peterson, K. A. Correlation Consistent Basis Sets for Actinides. I. The Th and U Atoms. *J. Chem. Phys.* **2015**, *142*, 074105.

56. Deng, H. T.; Kerns, K. P.; Castleman, A. W., Jr. Formation, Structures, and Reactivities of Niobium Oxide Cluster Ions. *J. Phys. Chem.* **1996**, *100*, 13386−13392.

57. Bell, R. C.; Zemski, K. A.; Kerns, K. P.; Deng, H.T.; Castleman, A. W., Jr. Reactivities and Collision–Induced Dissociation of Vanadium Oxide Cluster Cations. *J. Chem. Phys. A* **1998**, *102*, 1733−1742.

58. Bell, R. C.; Zemski, K. A.; Castleman, A. W., Jr. Size–Specific Reactivities of Vanadium Oxide Cluster Cations. *J. Cluster Sci.* **1999**, *10*, 509−524.

59. Zemski, K. A.; Justes, D. R.; Castleman, A. W., Jr. Studies of Metal Oxide Clusters: Elucidating Reactive Sites Responsible for the Activity of Transition Metal Oxide Catalysts. *J. Phys. Chem. B* **2002**, *106*, 6136−6148.

60. Jena, P.; Castleman, A. W., Jr. Mass Spectrometry and its Role in Advancing Cluster Science. *Int. J. Mass Spectrom.* **2015**, *377*, 235−247.

61. Foltin, M.; Stueber, G. J.; Bernstein, E. R. On the Growth Dynamics of Neutral Vanadium Oxide and Titanium Oxide Clusters. *J. Chem. Phys.* **1999**, *111*, 9577−9586.

62. Matsuda, Y.; Bernstein, E. R. On the Titanium Oxide Neutral Cluster Distribution in the Gas Phase: Detection through 118 nm Single–Photon and 193 nm Multiphoton Ionization. *J. Phys. Chem. A* **2005**, *109*, 314−319.

63. Yin, S.; Bernstein, E. R. Gas Phase Chemistry of Neutral Metal Clusters: Distribution, Reactivity, and Catalysis. *Int. J. Mass Spectrom.* **2012**, *321−322*, 49−65.

64. Molek, K. S.; Jaeger, T. D.; Duncan, M. A. Photodissociation of Vanadium, Niobium, and Tantalum Oxide Cluster Cations. *J. Chem. Phys.* **2005,** *123*, 144313.

65. Molek, K. S.; Reed, Z. D.; Ricks, A. M.; Duncan, M. A. Photodissociation of Chromium Oxide Cluster Cations. *J. Phys. Chem. A* **2007,** *111*, 8080−8089.

66. Molek, K. S.; Anfuso–Cleary, C.; Duncan, M. A. Photodissociation of Iron Oxide Cluster Cations. *J. Phys. Chem. A* **2008**, *112*, 9238−9247.

67. Reed, Z. D.; Duncan, M. A. Photodissociation of Yttrium and Lanthanum Oxide Cluster Cations. *J. Phys. Chem. A* **2008**, *112*, 5354−5362.

68. Knight, A. M.; Bandyopadhyay, B.; Anfuso, C. L.; Molek, K. S.; Duncan, M. A. Photodissociation of Indium Oxide Cluster Cations. *Int. J. Mass. Spectrom.* **2011**, *304*, 29−35.

69. Dibble, C. J.; Akin, S. T.; Ard, S.; Fowler, C. P.; Duncan, M. A. Photodissociation of Cobalt and Nickel Oxide Cluster Cations. *J. Phys. Chem. A* **2012**, *116*, 5398−5404.

70. Akin, S. T.; Ard, S. G.; Dye, B. E.; Schaefer, H. F.; Duncan, M. A. Photodissociation of Cerium Oxide Nanocluster Cations. *J. Phys. Chem. A* **2016**, *120*, 2313–2319.

71. Marks, J. H.; Ward, T. B.; Duncan, M. A. Photodissociation of Manganese Oxide Cluster Cations. *J. Phys. Chem. A* **2018**, *122*, 3383–3390.

72. Duncan, M. A. Invited Review Article: Laser Vaporization Cluster Sources. *Rev. Sci. Inst.* **2012**, *83*, 041101.

73. Duncan, M. A. Reflectron Time–of–Flight Mass Spectrometer for Laser Photodissociation. *Rev. Sci. Inst.* **1991**, *63*, 2177.

74. Frisch, M. J. et al. *Gaussian 09 (Revision* D.01); Gaussian, Inc.: Wallingford CT, **2013**.

75. Marks, J. H.; Khan, P.; Vasiliu, M.; Dixon, D. A.; Duncan, M. A. Photodissociation and Theory to Investigate Uranium Oxide Cluster Cations. *J. Phys. Chem. A* **2020**, *124*, 1940–1953.

CHAPTER 4

PHOTODISSOCIATION AND INFRARED SPECTROSCOPY OF URANIUM CATION NITROGEN COMPLEXES

To be submitted to the Journal of Physical Chemistry A

Photodissociation and Infrared Spectroscopy of Uranium Cation Nitrogen Complexes

J. H. Marks[1], B. M. Rittgers[1], M. van Stipdonk[2], M. A. Duncan[1*]

[1]Department of Chemistry, University of Georgia, Athens, Georgia 30602, U.S.A.

[2]Department of Chemistry and Biochemistry, Duquesne, Pittsburg, PA 15282, U.S.A.

*Email: maduncan@uga.edu

ABSTRACT

Laser vaporization of uranium in a pulsed supersonic expansion of nitrogen is used to generate complexes of $U^+(N_2)_n$ (n = 1–8). Complexes are mass selected in a reflectron time–of–flight mass spectrometer and spectra are measured using tunable infrared laser photodissociation spectroscopy. The spectra of $U^+(N_2)_n$ reveal intact N_2 ligands rather than the formation or uranium nitride, NUN. The N_2 stretch is observed about 130 cm^{-1} to the red of the free–molecule frequency for complexes with n = 3–8. Fixed frequency photodissociation at 532 and 355 nm indicate that the U–N_2 bond dissociation energy varies little with changing coordination. The consistent ratio of photon energy to the number of ligands eliminated allows an estimate of U^+–N_2 average bond dissociation energy of 12.1 ± 1.3 kcal/mol. Density functional theory is used to predict that U^+ is most stable in the sextet state with one to eight N_2 in an end–on orientation. The fully coordinated complex is predicted to be $U^+(N_2)_8$ with ligands forming a cube about the uranium cation. These calculations also predict infrared spectra that do not agree with experiment for smaller complexes. Despite the failure to accurately predict infrared spectroscopy, theory provides a prediction of the U^+–N_2 average bond dissociation energy of

11.8 ± 0.5 kcal/mol, in remarkably good agreement with the value estimated with 355 and 532 nm photodissociation.

INTRODUCTION

Uranium nitrides are a class of ceramic materials that is being implemented as a new nuclear energy source.[1–8] The use of these materials and their likely presence in nuclear waste necessitate research into the chemistry of nitrogenous uranium.[9–21] Uranium dinitride, NUN, is of particular interest because it is isoelectronic with the uranyl ion, UO_2^{2+}. Few uranium complexes are known that contain uranium nitride or uranium dinitride. Metalloorganic complexes incorporating nitrides or bonds to N_2 are prevalent in chemistry and represent likely intermediate structures in the Haber–Bosch ammonia synthesis. Transition metal neutral and ionic complexes with N_2 have been studied extensively with a variety of spectroscopic methods.[22–38] The effect of 5f electrons on the reactivity and catalytic activity of uranium complexes is an area of active research.[39] The 5f and 6d orbitals are found to vary in both relative size and energy across the actinide series. The 5f orbitals are contracted and stabilized by increasing nuclear charge more strongly than the 6d orbitals. Because of this only the first five actinides possess 5f orbitals diffuse enough to act as valence orbitals. The role of the 5f orbitals in covalency between uranium and N_2 is of particular interest.[40–48] Mass spectrometry techniques have been used to investigate several uranium ion complexes and clusters.[49–62] This class of compounds has been studied in matrix isolation[63–72] in the gas phase,[73–90] and computationally.[91–107] In this study we employ infrared photodissociation spectroscopy to investigate complexes of uranium cation and nitrogen.

Liddle and coworkers have contributed a large body of work on the synthesis and characterization of actino–nitrides such as uranium nitride.[15,17,44–46] Matrix isolation has been the primary route of investigation for uranium nitrogen complexes.[63–72] Uranium dinitride is of particular interest because it is isoelectronic with the uranyl cation, UO_2^{2+}, which is ubiquitous in the aqueous chemistry of uranium. Andrews and coworkers have published several papers on the infrared spectroscopy of uranium nitride compounds in rare gas and nitrogen matrixes.[64–70] This includes a study on molecular nitrogen complexes of uranium, uranium nitride, and uranium dinitride.[70] Gas phase spectroscopy on uranium compounds is similarly limited. Gas phase spectroscopy has focused largely on complexes of the oxides of uranium, chiefly uranyl.[73–76,78–82,87–90] A study by Bowen and coworkers measured the photoelectron spectrum of the uranium dinitride anion.[83] This revealed a closed shell electronic structure with uranium in the +6 oxidation state, isoelectronic with the uranyl cation. The insertion of U into N_2 is found to result in a linear structure with each nitrogen triple bonded to the uranium.

Actinides present a range of challenges for computational chemistry. Accurately modeling the effects of relativistic electron velocity and occupied f orbitals are active areas of research. The large number of electrons poses further issues of computational cost. Relativistic Hamiltonians with all–electron treatments are preferred but are prohibitively expensive for large molecules or surveying many isomers. Fully relativistic effective core potentials (ECP) reduce computational expense but provide accurate treatment of valence electrons, where core–correlation error is low. Previous computational work on $U(N_2)_n$ molecules by Gagliardi and coworkers used B3LYP with the SDD relativistic ECP and large Pople basis set to investigate the many isomers and spin states possible.[68–70] These computations predict that the fully coordinated complex contains seven nitrogen molecules bound end–on to the neutral uranium.

The recently published cc–pVnZ–PP basis set using the Stuttgart/Köln fully relativistic 60 electron ECP for use with uranium is compatible with Dunning basis sets on non–relativistic atoms such as nitrogen.[108,109] Further development of computational chemistry in this field is dependent on comparison to gas phase spectra of uranium complexes, of which there is only a small body of work.

Infrared photodissociation spectroscopy is a technique that has been applied to transition metal–N_2 complexes.[31–33] These are generally observed to have an N_2 stretch that is IR active and a red shift of about 100 cm^{-1} compared to the free N_2 frequency due to interaction with the transition metal. This technique has also been successful in previous investigations of uranium oxide, superoxide, carbonyl, and oxide carbonyl.[85,86] $U^+(CO)_8$, isoelectronic with $U^+(N_2)_8$, was observed to have a CO stretch about 60 cm^{-1} to the red of the free CO stretch. The complexes of V^+ and Nb^+ with N_2 have also been investigated.[31,32] In both the case of $V^+(N_2)_n$ and $Nb^+(N_2)_n$ the N_2 stretch was observed to become IR active and red shifted about 100 cm^{-1} due to interaction with the transition metal cation. Comparison to DFT computations indicated nitrogen binding end–on, with a slight lengthening of the N_2 bond. The red shift and bond lengthening are described by the Dewar–Chatt–Duncanson (DCD) model of binding, in which the ligand donates electron density from its σ bond and the metal back–binds to provide electron density to the unoccupied ligand π^* orbital. The effects that f electrons may have on such a bond are investigated here in $U^+(N_2)$. Infrared photodissociation spectroscopy and comparison to DFT computations are used to investigate the structure of $U^+(N_2)_n$ complexes and the nature of the U^+–N_2 bond.

EXPERIMENTAL

Uranium cation–nitrogen complexes are produced in a pulsed supersonic expansion of 100 psi nitrogen (UHP, Airgas) with laser vaporization of uranium. A Spectra Physics INDI laser is used to produce up to 20 mJ/pulse of 355 nm light for vaporization.[110] Mass separation and selection are carried out in a reflectron time–of–flight mass spectrometer previously reported.[111] After mass selection, photodissociation and further mass separation of dissociation products is conducted in the reflectron. Tunable infrared light for photodissociation is produced with a Laser Vision OPO/OPA. Infrared radiation is passed through the photodissociation region of the reflectron and retroreflected with a concave gold mirror to improve the photodissociation yield. Laser radiation at 355 and 532 nm is produced by a Spectra Physics GCR–150 for photodissociation with only one pass at energies of 0.22 – 106 MW/cm^2.

Uranium cation–nitrogen complexes are investigated with B3LYP/cc–pVTZ–PP.[112] The product of insertion chemistry, NUN^+, was investigated only for the smallest complexes. The energy of all proposed isomers of $U^+(N_2)_n$ (n = 1–8) were calculated for doublet, quartet, and sextet spin states. Isomers incorporating either side–on, or end–on bonds, or both in combination were considered and optimized without structural constraint. Vibrational frequency and natural bond orbital (NBO) analyses were conducted on all optimized structures. A scaling factor of 0.951 was calculated by predicting the frequency of the N_2 stretch at the same level of theory. All predicted spectra are shown only in the N_2 stretching region and scaled.

RESULTS AND DISCUSSION

The mass spectrum produced with uranium laser vaporization in a nitrogen supersonic expansion is shown in Figure 4.1. The peak for U^+ is off scale and about twenty times larger

than any complex or cluster cation observed, indicating inefficient clustering with molecular nitrogen. The mass coincidence between UN^+ and $(N_2)_9^+$ leaves some confusion as to the identity of the small peaks between each of the numbered $U^+(N_2)_n$. However, the similar intensity of the well resolved $(N_2)_n^+$ peaks between U^{2+} and U^+ is strong evidence that all or most of these mass coincident peaks are due to pure nitrogen cation clusters. The small peak observed as a sharp shoulder on the left side of UO^+ is UN^+ and/or $(N_2)_9^+$. Complexes of $U^{2+}(N_2)_n$ were observed with low intensity in the 100 to 200 amu range. These peaks are less intense than the N_2 cation clusters of similar mass. Complexation of U^+ with N_2 produces only small quantities of $U^+(N_2)_n$ from n = 1–8, with some slight variations in intensity. The peaks for even values of n tend to be more intense, particularly for n = 8. With n > 8 the intensity of $U^+(N_2)_n$ is diminished by an order of magnitude. This is a significant indication that the fully coordinated complex is n = 8. No such drop–off in intensity is observed for the small peaks between the numbered peaks that may be $(N_2)_n^+$ or $UN^+(N_2)_n$, which is further evidence for the attribution of these peaks to pure molecular nitrogen cation clusters.

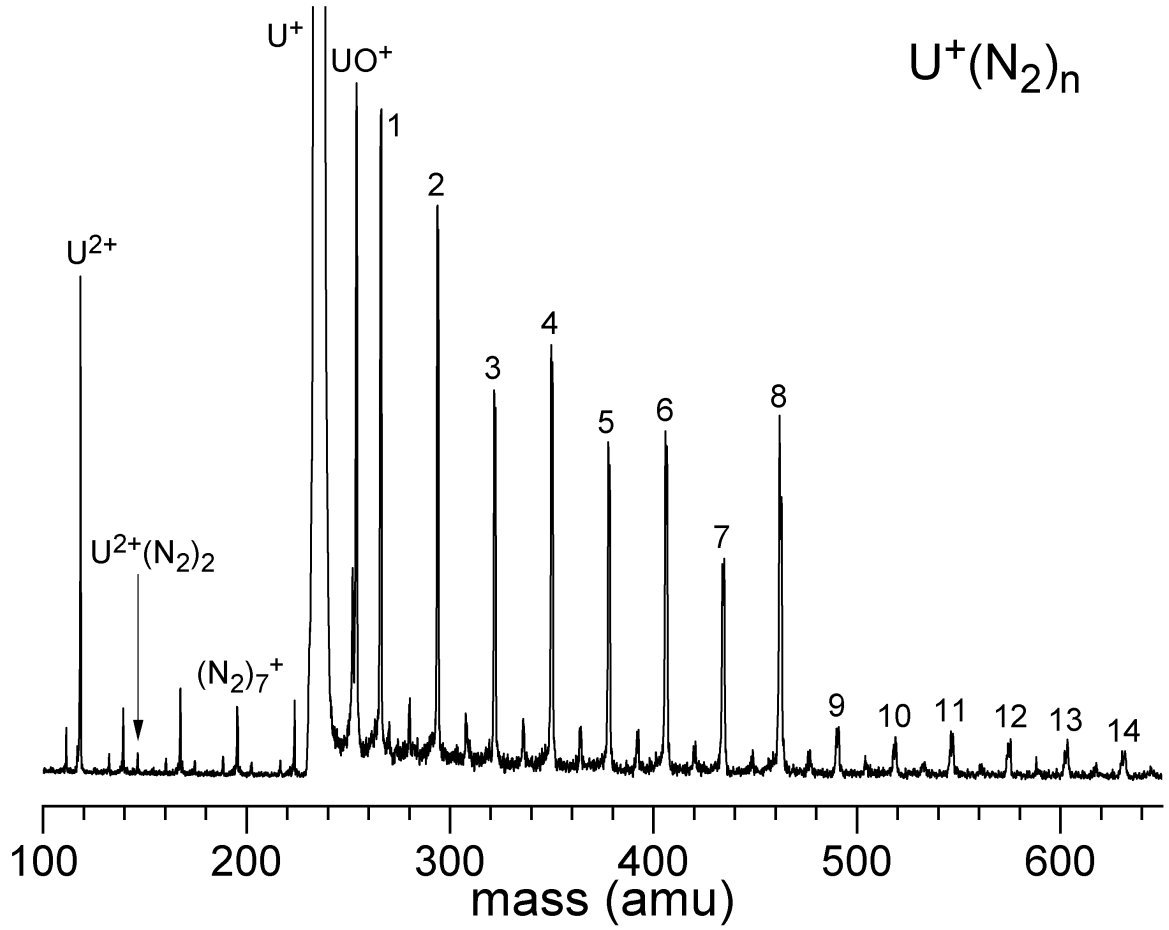

Figure 4.1. Mass spectrum obtained using a 100 psi pure N_2 expansion and laser vaporization of uranium metal. Complexes of $U^+(N_2)_n$ are found to be relatively intense only for n = 1–8. A large decrease in intensity observed for n > 8 may indicate that this is the fully coordinated complex.

Fixed frequency photodissociation at multiple wavelengths was used to investigate how photon energy affects dissociation. Difference mass spectra were calculated by subtracting the mass spectrum observed with photodissociation from that measured without. In such mass spectra positive peaks indicate the masses of cations formed from the dissociating species, and negative peaks indicate the loss of signal for the dissociating species. The difference mass spectra observed for $U^+(N_2)_8$ are shown in Figure 4.2. The photodissociation laser fluence power dependence of the fragment ion peak intensity was studied for this ion. It was found that the

relative intensity of U^+ to the other fragments responds non–linearly as laser power is varied for both 532 and 355 nm photodissociation. For measurement with 355 nm, the n = 1, 2 and 3 fragments are observed with the same intensity relative to each other regardless of laser power. The same is true of the n = 3 and 4 fragments observed at 532 nm. This shows that it is likely that these fragments are all the result of a single photon process. The elimination of 6–7 N_2 from $U^+(N_2)_8$ with the laser photon energy of 28170 cm^{-1} indicates an average bond energy of 11.5–13.4 kcal/mol. The elimination of 3–4 ligands with 18800 cm^{-1} similarly indicates 10.8–13.4 kcal/mol. The similarity of these values could be taken to indicate that the energy with which each successive N_2 bonds to U^+ is very similar.

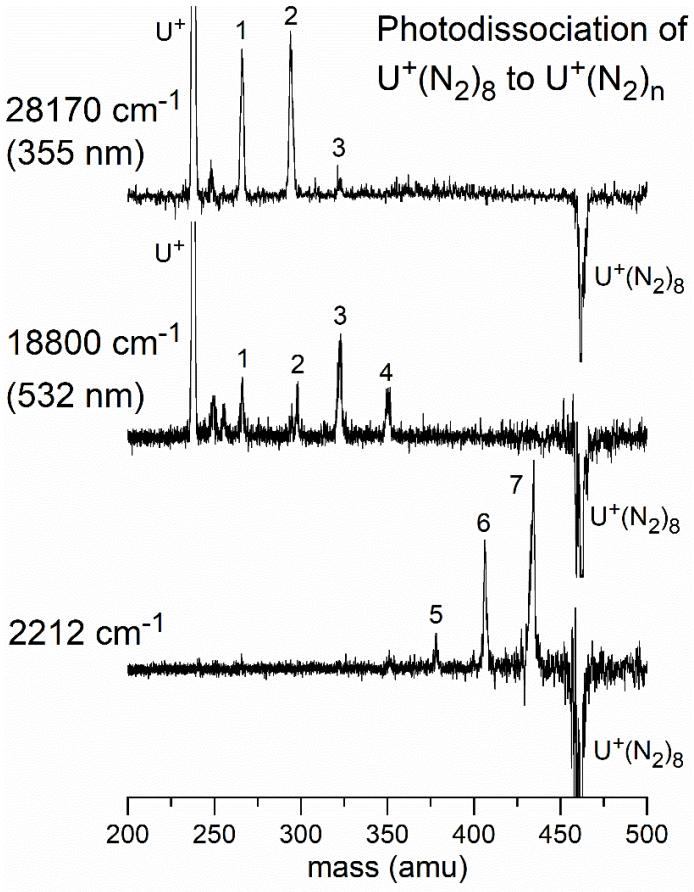

Figure 4.2. Photodissociation of $U^+(N_2)_n$ for n = 8 measured with 355 and 532 nm Nd:YAG harmonics and 2212 cm^{-1} light in the infrared. The ratio of photon energy to N_2 eliminated is consistent at both 355 and 532 nm, indicating an average U^+–N_2 bond is 12.1 ± 1.3 kcal/mol. Photodissociation from the 2212 cm^{-1} light is likely multiphoton in origin.

If the average U^+–N_2 bond dissociation energy (BDE) is in the range of 10.8–13.4 kcal/mol, then single photon photodissociation should not be observable with infrared light in the range of 2200 cm^{-1}, with photon energy of 6.3 kcal/mol. The lower trace of Figure 4.2 may be the result of single photon photodissociation, and the estimate of BDE obtained with 355 and 532 nm photodissociation would then be substantially high. Alternatively, it is possible that the infrared dissociation is a multiphoton process, because the infrared measurements were made using a concave folding mirror, which causes a focal point in the photodissociation region of the mass spectrometer. In this region of the spectrum the infrared laser can produce only 1 mJ/ pulse on average. The focused light was necessary for producing detectable photodissociation with low laser power. It was found to produce a non–linear response in fragmentation intensity to changes in photodissociation laser power. This is an indication of multiphoton absorption, making this the likely process.

The small peaks between U^+ and n = 1 in Figure 4.2 were determined to result from intense photodissociation to form U^+ and $U^+(N_2)$ by nearby masses not fully attenuated by the mass–selector. There is no evidence for the formation of any molecule containing an odd number of nitrogen atoms from the photodissociation of $U^+(N_2)_8$ or any other investigated complex. This is evidence for a lack of reactions between U^+ and N_2 to would form $UN^+(N_2)_n$ or $NUN^+(N_2)_n$. $UN^+(N_2)_n$ should produce fragment ions with odd numbers of nitrogen which were not observed. Furthermore, if the NUN^+ ion is strongly bonded, like the uranyl ion, the smallest ion produced may be n = 1, though it was observed to be U^+ in n = 8 in Figure 4.2, as was found to be the case for complexes n = 1–7.

Infrared photodissociation mass spectra for $U^+(N_2)_n$ for n = 3–8 were measured at the peak absorption found for each complex. Those ions larger than n = 4 all dissociate to give

some amount of n = 4, while ions n = 4 and smaller eliminate fewer N_2. This is a clear indication that the n = 4 complex possesses some additional stability beyond that of larger complexes. This complex would possess a half–filled inner coordination if the fully coordinated complex is n = 8 as indicated by the mass spectrum in Figure 4.1. This stability may derive from a higher symmetry structure, such as the tetrahedral or square planar configurations possible for a tetravalent complex. If each N_2 ligand donates electron density from both π bonds, then a total of 21 electrons are in circulation about the uranium. This increased stability may derive from the 22–electron rule. Some actinides exhibit behavior associated with the similar 18 electron rule for transition metals. The d orbitals in some actinides are higher in energy than the s, p, and f orbitals, leaving a 22–electron valence shell of the $s^2p^6f^{14}$. Examples include U(cyclooctatetraene)$_2$ also known as uranocene, uranium hexacarbonyl, and uranium hexahalides, all of which are stable with 22 valence electrons interacting with uranium.

The infrared photodissociation spectra of $U^+(N_2)_n$ (n = 3–8) are shown in Figure 4.3. Infrared photodissociation was not observed for complexes with n = 1 or 2, and rare gas tagged complexes were not observed. The spectrum of n = 3 is found to be more complicated than those observed for larger complexes. The peak at 2245 cm^{-1} is likely the N_2 stretch, which is red shifted 85 cm^{-1} from the free N_2 stretch at 2330 cm^{-1}, marked by the red vertical dashed line. The low, broad features at 2194 and 2394 cm^{-1} may be the same vibration present in multiple isomers, or could be attributable to multiphoton absorption due to the high photodissociation laser fluence needed to produce observable signal. This blue shifted feature is also observed for n = 4 at 2371 cm^{-1}, though significantly diminished, and is not observed for any other complex. The N_2 stretch is found to red shift slightly more as n increases from 3 to 7. This trend reaches a maximum with the N_2 stretch 132 cm^{-1} to the red of the free vibration. The n = 8 complex is the

largest complex produced in the mass spectrometer with sufficient intensity to allow a spectrum to be measured. The only observed peak is found at 2212 cm^{-1}, less red shifted than n = 5, 6, or 7. This peak is also more intense and narrow which may indicate that all other complexes are present in multiple isomers while n = 8 is not. This narrow peak may also be caused by a higher symmetry structure in which most or all of the local N_2 stretches are degenerate. This conclusion may be warranted by comparison to spectra of $U^+(CO)_8$, which is predicted to have cubic coordination.

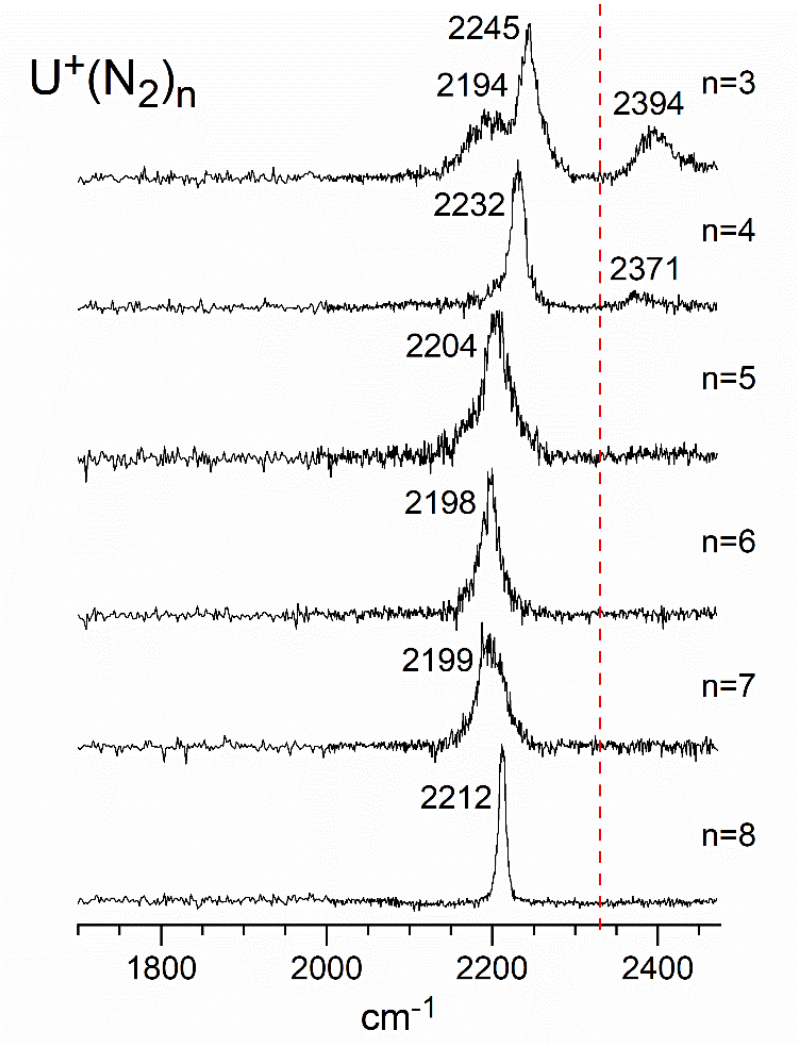

Figure 4.3. Infrared photodissociation spectra of $U^+(N_2)_n$ for n = 3–8 in the N_2 stretching region. The position of the normally infrared inactive N_2 stretch is marked with the red dashed line.

Computational chemistry at the B3LYP/cc–pVTZ–PP level was used to predict the electronic state, nuclear structure, and vibrational frequencies of $U^+(N_2)_n$ for n = 1–8, and $NUN^+(N_2)_{n-1}$ for n = 1–3. For all isomers of $U^+(N_2)_n$ for which doublet, quartet, and sextet electronic states were found to be stable, the sextet is invariably lower in energy by about 9 kcal/mol, followed by the quartet, then doublet which is usually 12 to 20 kcal/mol higher in energy than the sextet. It should be noted that DFT tends to over–stabilize high spin states, though this effect is unlikely to produce an error as large as 9 kcal/mol. The opposite trend is observed for computations of $NUN^+(N_2)_{n-1}$, where the doublet is invariably lower in energy. This is likely due to the closed shell nature of NUN, which consists of U in the +6 oxidation state triple bonding to two axial nitrogen atoms. Formation of NUN^+ in higher spin states then corresponds to ionization of excited states of NUN, because an ionized closed shell neutral can only produce a doublet unless excited. Ionization of this species requires the removal of an electron from a core orbital of uranium. The ionization potential (IP) of NUN is predicted to be about 3 eV higher than that of uranium at 6.2 eV. The NUN^+ doublet is expected to lie 11.9 kcal/mol above the energy of $U^+(N_2)$. Low energy structures of $NUN^+(N_2)_{n-1}$ for n = 2 or 3 are also predicted to be less stable, 9.4 and 8.3 kcal/mol higher in energy than the non–inserted isomers.

Predicted structures of $U^+(N_2)_n$ for n = 1–8 are shown in Figure 4.4. The isomers presented here are predicted to be the most stable structure for each value of n. Complexes n = 4 and 5 have trigonal pyramidal and trigonal bipyramidal coordination respectively. Complexes n = 6–8 show cubic coordination with ligands bound at the corners of a cube centered on U^+. The minimum energy structures for n = 6 and 7 both have unoccupied binding sites, while n = 8 is predicted to have the symmetry of a cube, the T_d point group. These structures all consist of

entirely end–on bonds between U^+ and N_2. This results in a slight elongation of the N_2 bond by 3.3 pm in the 1a sextet. This effect decreases as n grows and N_2 is only elongated by 0.8 pm in the 8a sextet.

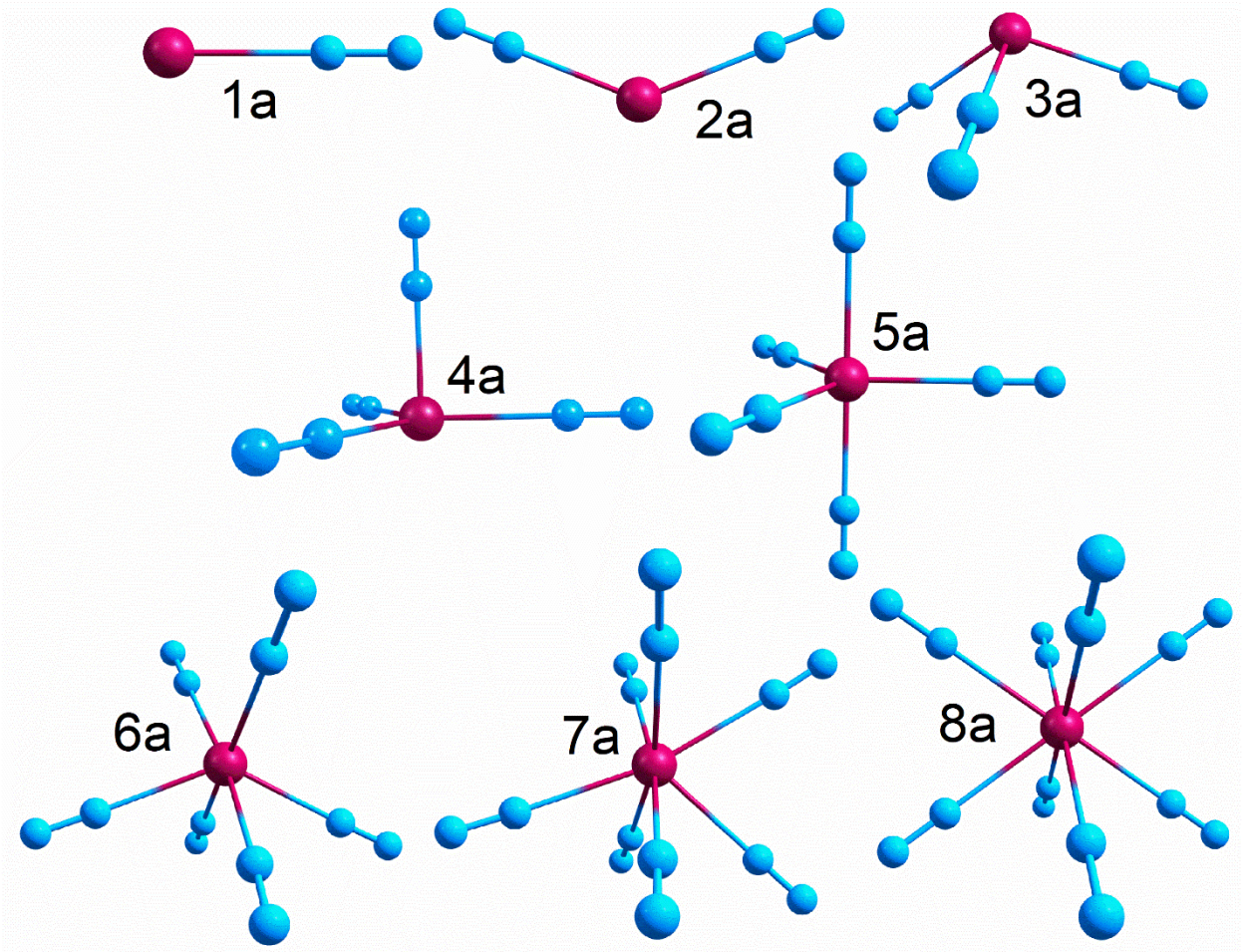

Figure 4.4. The lowest energy structures of $U^+(N_2)_n$ for each value of n. The complexes shown are all in the sextet state which was found to be the lowest energy spin state for all $U^+(N_2)_n$ isomers which are stable in the sextet state. The n = 4 and 5 structures show preference for trigonal bipyramidal coordination, while n = 6, 7, and 8 successively build a square prism.

The measured spectrum of $U^+(N_2)_3$ is shown in Figure 4.5 with simulated spectra predicted for the lowest energy 3a isomer with several possible multiplicities and isomers 3b, 3c, and 3d. The spectra predicted for isomer 3a in the sextet, quartet, and doublet states all vary considerably, though the increase in relative energy with lower spin states makes the presence of

these isomers less likely. The 3a sextet is predicted to show a large peak which should be accompanied by a smaller peak higher in energy. This large peak is predicted at 2068 cm^{-1} while the major peak in the measured spectrum is at 2245 cm^{-1}. The spectra predicted for the 3a quartet and doublet both have two major peaks which may explain the pair of peaks measured at 2194 and 2245 cm^{-1}. However, like the 3a sextet these doublet and quartet state vibrations are all far too low in energy to be considered to match experiment.

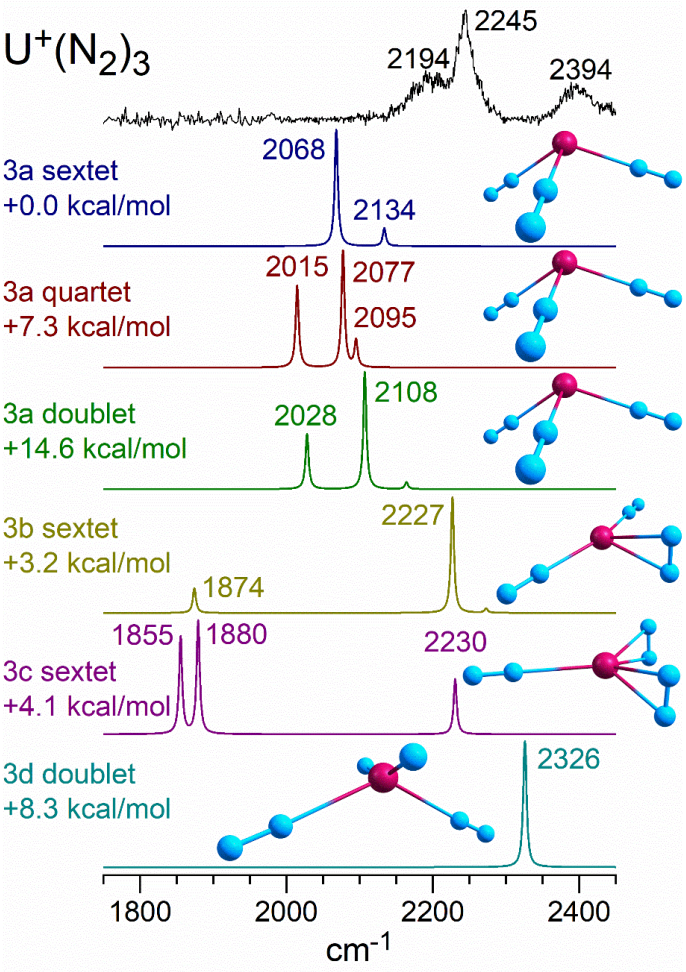

Figure 4.5. The experimental spectrum of $U^+(N_2)_3$ with simulated spectra of the lowest energy isomer, 3a, in the sextet, quartet, and doublet states. Below are simulated spectra of isomer 3b, 3c, and 3d sextets. Side–on bonding and NUN^+ formation are both predicted to yield spectra closer what was observed, though they are both predicted to lie higher in energy than the 3a isomer.

Other isomers which may produce a satisfactory match with experiment were explored and several low energy isomers are shown in Figure 4.2. The 3b and 3c sextets both include one and two N_2 ligands, respectively, binding side–on. This increases the relative energy of these isomers by 3.2 kcal/mol for 3b and 4.1 kcal/mol for 3c. These structures both predict a large infrared absorption within 20 cm^{-1} of the 2245 cm^{-1} peak. The 3b and 3c isomers are both predicted to have vibrations at about 1880 cm^{-1} attributed to the stretching of the side–on bound N_2. These vibrations are expected to be much less intense than those of the end–on bound nitrogen whose stretch occurs at 2227 cm^{-1} in isomer 3b. The doublet of isomer 3d was also investigated to see if insertion chemistry produced a stable structure that matched the experiment. This structure is predicted to produce nearly no red shift of the N_2 stretch in the end–on ligands. These ligands are predicted to vibrate at 2326 cm^{-1}, nearly identical to the frequency of the free N_2 stretch at 2330 cm^{-1}. The formation of the NUN^+ structure is expected to be energetically unfavorable, decreasing the relative stability of the complex by 8.3 kcal/mol. It should be noted that the vibration at 2336 cm^{-1} predicted for isomer 3d is the closest any isomer comes to explaining the origin of the peak at 2394 cm^{-1}. No predicted spectrum of any isomer or spin state of $U^+(N_2)_3$ or $NUN^+(N_2)_2$ provides convincing evidence for the structure of this complex.

The experimental spectrum of $U^+(N_2)_4$ is shown in Figure 4.6 with simulated spectra of isomers 4a, 4c, and 4d. With this size complex and larger there are multiple ways to arrange the end–on N_2 ligands to produce isomers such as 4a and 4c, and side–on binding produces additional isomers. The 4a and 4c isomers are both predicted to have intense absorptions which might be attributed to the observed 2232 cm^{-1} peak. However, as was the case with $U^+(N_2)_3$, these vibrations are predicted too far to the red of the measured absorption. The peak predicted

at 1978 cm^{-1} for isomer 4a is not evident in the experimental data, as only baseline is observed to the red of the 2232 cm^{-1} peak. The 4d isomer predicts the side–on binding N_2 ligands to vibrate in the region of 1900 cm^{-1} where no signal is found. In the predicted spectra for both $U^+(N_2)_n$ for n = 3 and 4, the N_2 in an end–on bond is expected to have a vibration over 100 cm^{-1} to the red of the observed peak, and the side–on binding N_2 stretch is expected over 300 cm^{-1} to the red of the observed peak. It may be that these calculations over–estimate the effect of the uranium cation on the end–on nitrogen. If this is the case, then it is plausible that isomer 4c is the observed structure and its two peaks are simply not resolved. Furthermore, none of these spectra predict any vibration which could provide an explanation for the peak at 2371 cm^{-1}. This peak may be the result of a combination band of the N_2 stretch with either a U^+–N_2 stretch or U^+NN bend. Alternatively, this peak could originate from the presence of a small amount of $NUN^+(N_2)_3$. The $NUN^+(N_2)_2$ spectra for isomer 3d in Figure 4.5 is predicted to yield the highest frequency N_2 stretch. This may be the case for $NUN^+(N_2)_3$ as well, from which the 2371 cm^{-1} peak might originate.

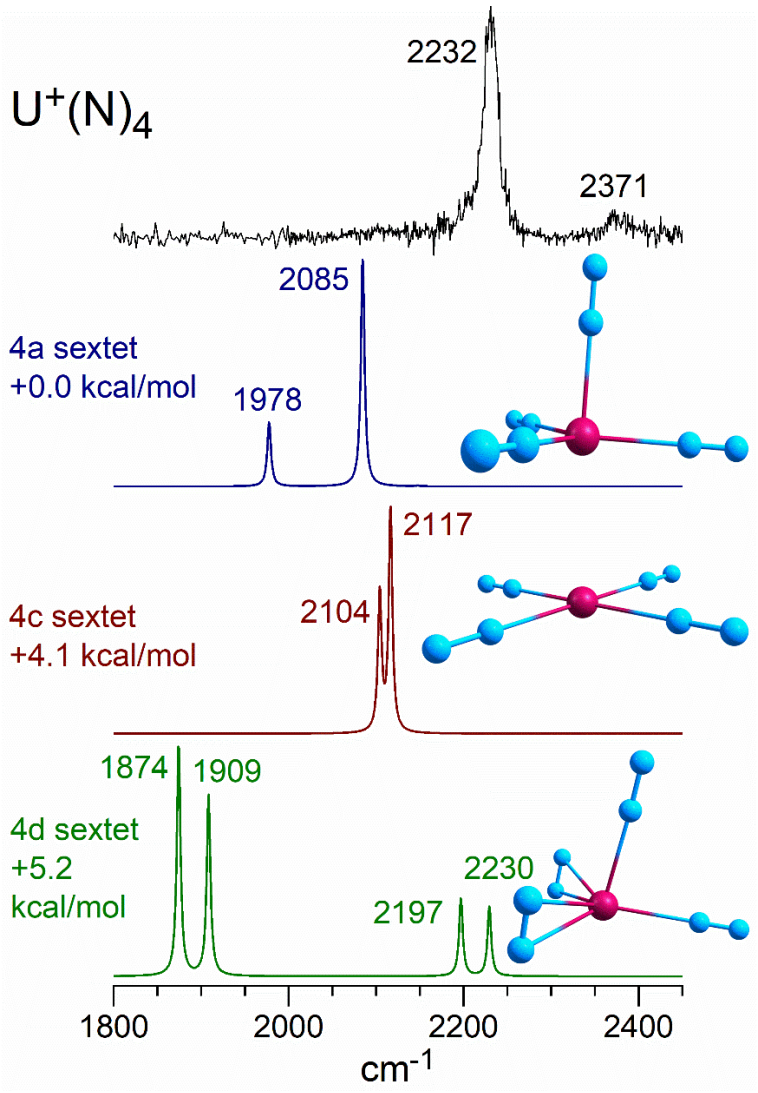

Figure 4.6. The experimental spectrum of $U^+(N_2)_4$ with simulated spectra of isomers 4a, 4c, and 4e sextets. No predicted spectrum provides a satisfactory match with experiment. Side–on bonding is expected to cause a substantial N_2 red shift in isomer 4d among others. No photodissociation is detected in this region of the spectrum, from 1800 to 2000 cm $^{-1}$.

The spectrum of $U^+(N_2)_8$ is shown in Figure 4.7 with predicted spectra for the three lowest energy isomers. These spectra mark a departure from the poor matches between experiment and theory shown in Figures 5 and 6. The assignment of the peak predicted for isomer 8a at 2184 cm^{-1} to that observed experimentally only 28 cm^{-1} higher in energy is obvious. No other isomer of this complex is predicted to produce a spectrum consisting of a single narrow peak. The 8a isomer optimized to cubic coordination without any symmetry constraints and is

expected to represent the fully coordinated complex. The isomers 8b and 8c both contain N_2 in the side–on position. Because of the large coordination of these complexes, side–on binding introduces steric strain not evident for the n = 3 or 4 complexes. Rotation of two ligands from end–on to side–on bonds results in an increase in energy by 18.5 kcal/mol for isomer 8b and 18.7 kcal/mol for isomer 8c. The similar rotation of two ligands in $U^+(N_2)_4$ was found to increase energy by only 5.2 kcal/mol in the case of isomer 4d in Figure 4.6. This much larger increase in energy for side–on bonding in n = 8 complexes is attributable entirely to steric crowding of ligands about the uranium. This steric crowding also results in a change in coordination geometry from cubic to square antiprismatic in isomers 8b and 8c. This was predicted to be the stable coordination of $U^+(CO)_8$, although in that complex all carbonyl ligands are expected to bind end–on in a U^+–CO configuration.

Bond dissociation energies (BDE) for the $U^+(N_2)_n$ complexes are detailed in Table 4.1. The BDE calculated for the elimination of one nitrogen from a complex with any n ligands assumes dissociation to form the most structurally similar isomer with n–1 ligands. This value is found to vary significantly throughout the range of isomers presented. The BDE of the n = 4 complexes is 14.0 kcal/mol, which is predicted to be the strongest U^+– (N_2) bond. This could be attributed to stability of a complex nearing 22 electrons, though this complex is the cation of a neutral 22–electron complex, having only 21. The average bond energies of these complexes are calculated from the total bond energy of the complex from U^+ and N_2 units divided by n. These values are found to be remarkably consistent as for different values of n. This is in good agreement with the patterns observed from 355 and 532 nm photodissociation in Figure 4.2. Excitation at Both wavelengths removed a number of N_2 ligands proportional to the photon energy; the average BDE predicted from this experiment is 12.1 ± 1.3 kcal/mol. If the lowest

energy isomer for each complex with n N_2 is considered, the range of values for average BDE is 11.3–12.2, well within the error of the experiment. This is a remarkable agreement given how poorly these calculations predicted infrared spectra.

Table 4.1. Relative energies of isomers of $U^+(N_2)_n$ for n = 1–8 and bond dissociation energies (BDE) calculated for one N_2 ligand or as an average over all N_2 ligands. All energies are listed in kcal/mol. For brevity only the lowest energy spin state of selected isomers are presented here.

Isomer	**Rel. Energy**	**BDE last N_2**	**Mean BDE per N_2**
1a sextet	+0.0	13.1	13.1
1b doublet	+11.9	13.0	13.0
1c sextet	+14.2	–1.1	–1.1
2a sextet	+0.0	10.2	11.6
2b sextet	+0.3	9.8	11.5
2c sextet	+3.0	7.2	10.1
3a sextet	+0.0	10.8	11.4
3b sextet	+3.2	10.6	10.3
3c sextet	+4.1	9.7	10.0
3d doublet	+8.3	11.9	12.5
4a sextet	+0.0	14.0	12.0
4b sextet	+1.6	12.4	11.6
4c sextet	+4.1	9.9	11.0
5a sextet	+0.0	13.1	12.2
5b sextet	+1.7	11.4	11.9
5c sextet	+8.0	10.3	10.6
6a sextet	+0.0	10.4	11.9
6b sextet	+0.1	10.3	11.9
6c sextet	+1.2	10.9	11.7
7a sextet	+0.0	10.4	11.7
7b sextet	+13.8	9.7	7.0
7c sextet	+20.0	4.9	8.9
8a sextet	+0.0	8.7	11.3
8b sextet	+18.5	4.0	9.0
8c sextet	+18.7	3.7	9.0

These computational results show excellent agreement with the experimentally determined average bond energy, but poor agreement with infrared spectra. Disagreement between theory and experiment in the infrared spectra is found to be substantially worse in the

smaller complexes, but much better for the n=8 complex. While the agreement between experiment and theory could be improved upon, the 28 cm^{-1} error for n = 8 marks a large improvement on the accuracy of predictions for smaller complexes shown in Figures 4.5 and 4.6.

A systematic error is observed infrared spectra predicted for $U(N_2)_n$ complexes with B3LYP/cc–pVTZ–PP. As n decreases from 8, the N_2 stretch is predicted increasingly to the red of the observed peak. The smallest complex for which spectra were measured is the n = 3, which is predicted to vibrate 180 cm^{-1} to the red of the observed vibration. The B3LYP/cc–pVTZ–PP calculations used to make these predictions was compared to prior predictions and published infrared gas phase spectra of uranium complexes. However, few gas phase infrared spectra of uranium cation complexes have been published.

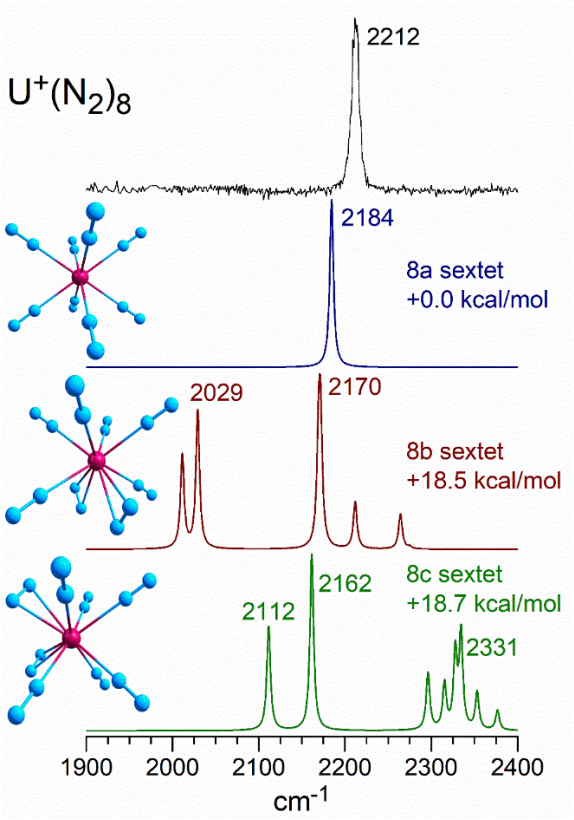

Figure 4.7. The experimental spectrum of U+(N2)8 with simulated spectra of isomers 8a, 8b, and 8c sextets. The predicted band position for the cubic isomer 8a is close to the observed peak, while the less symmetric isomers predicted would all be predicted to yield more complex spectra.

The only previous vibrational spectroscopy on small uranium cation complexes is our work on $U^+(CO)_8$, $UO_2^+(CO)_5$, UO_4^+, and UO_6^+.[85,86] This spectroscopy was accompanied by infrared transitions predicted with the PBE functional with VTZP on carbon and oxygen with SDD on uranium. To validate the theoretical methods used in the present work on nitrogen complexes, we have re–investigated the spectroscopy of these complexes studied previously. The B3LYP/cc–pVTZ–PP predictions are seen to be in good agreement with experiment in Figures 4.8 through 4.11. It is also shown that these B3LYP calculations are an improvement on the PBE results originally published with the spectra. For B3LYP calculations the scaled vibrations are lower in frequency than experiment for seven of the eight vibrations observed in Figures 4.8 through 4.11. This trend was observed for $U^+(N_2)_8$ in Figure 4.7 in which the N_2 stretch was predicted to be 28 cm^{-1} lower in energy than was observed. These complexes are fully coordinated in the case of $U^+(CO)_8$, $UO_2^+(CO)_5$, and $U^+(N_2)_8$, and nearly so for $UO_2^+(O_2)$ and $UO_2^+(O_2)_2$. There are no published spectra of incompletely coordinates U^+ complexes with which to evaluate these computational methods. The accuracy of B3LYP calculations seems to improve for UO_6^+ over UO_4^+, with average absolute errors of 9 and 32 cm^{-1} respectively.

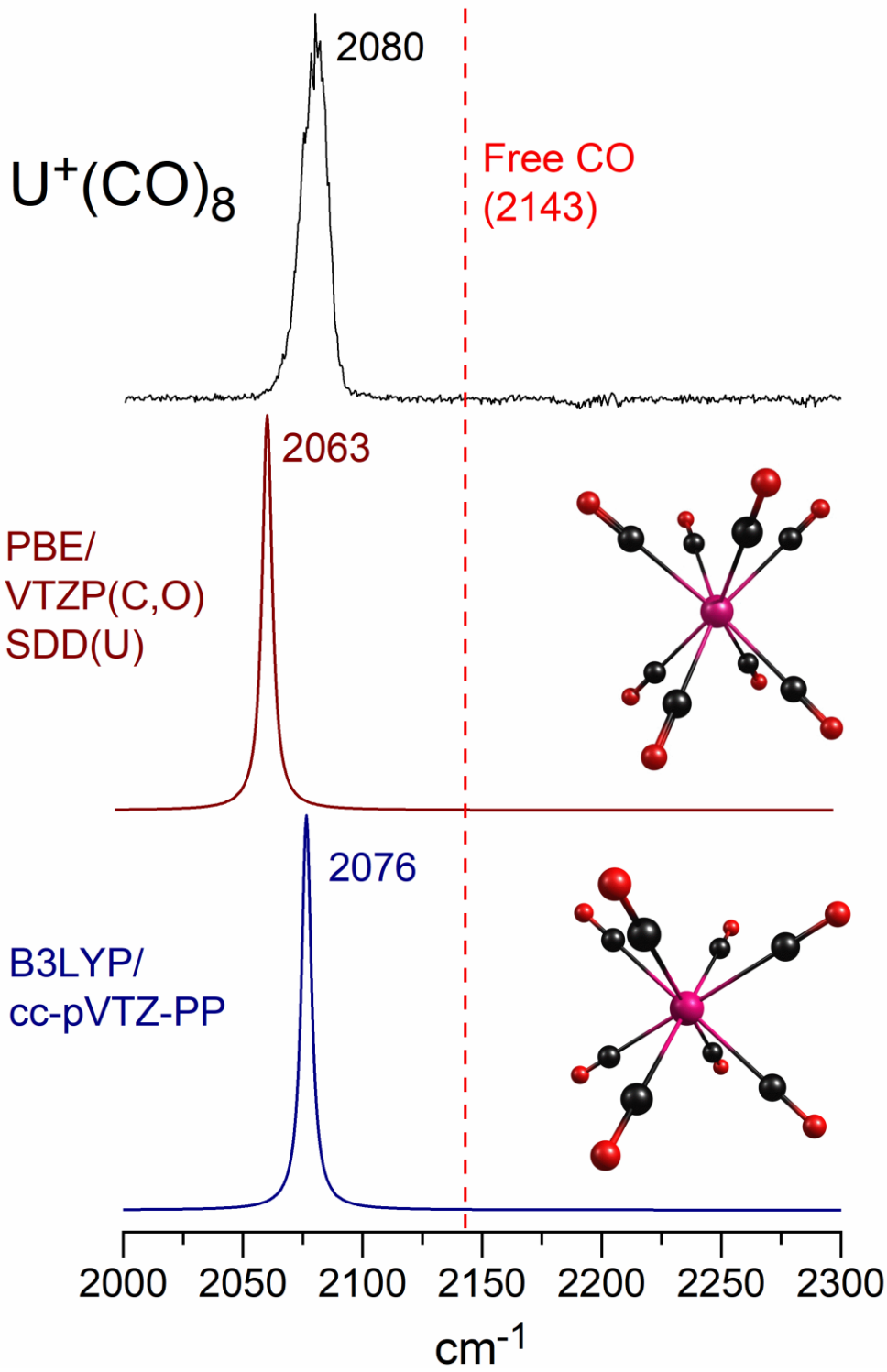

Figure 4.8. Infrared photodissociation spectrum of $U^+(CO)_8$ with simulated spectra calculated at two levels of theory. The PBE functional with VTZP on carbon and oxygen and SDD on uranium are shown with B3LYP/cc–pVTZ–PP.

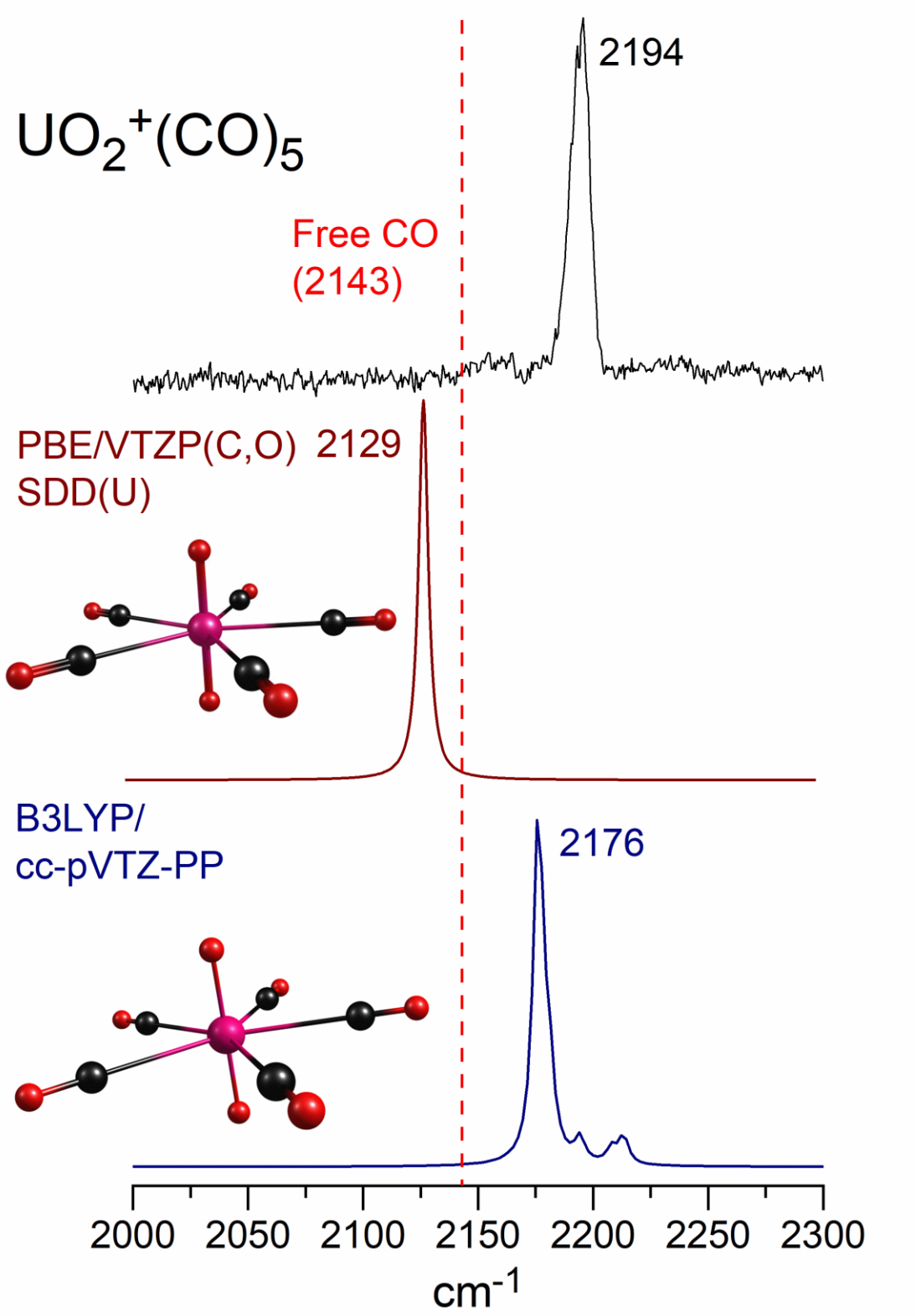

Figure 4.9. Infrared photodissociation spectrum of $UO_2^+(CO)_5$ with simulated spectra calculated at two levels of theory. The PBE functional with VTZP on carbon and oxygen and SDD on uranium are shown with B3LYP/cc–pVTZ–PP.

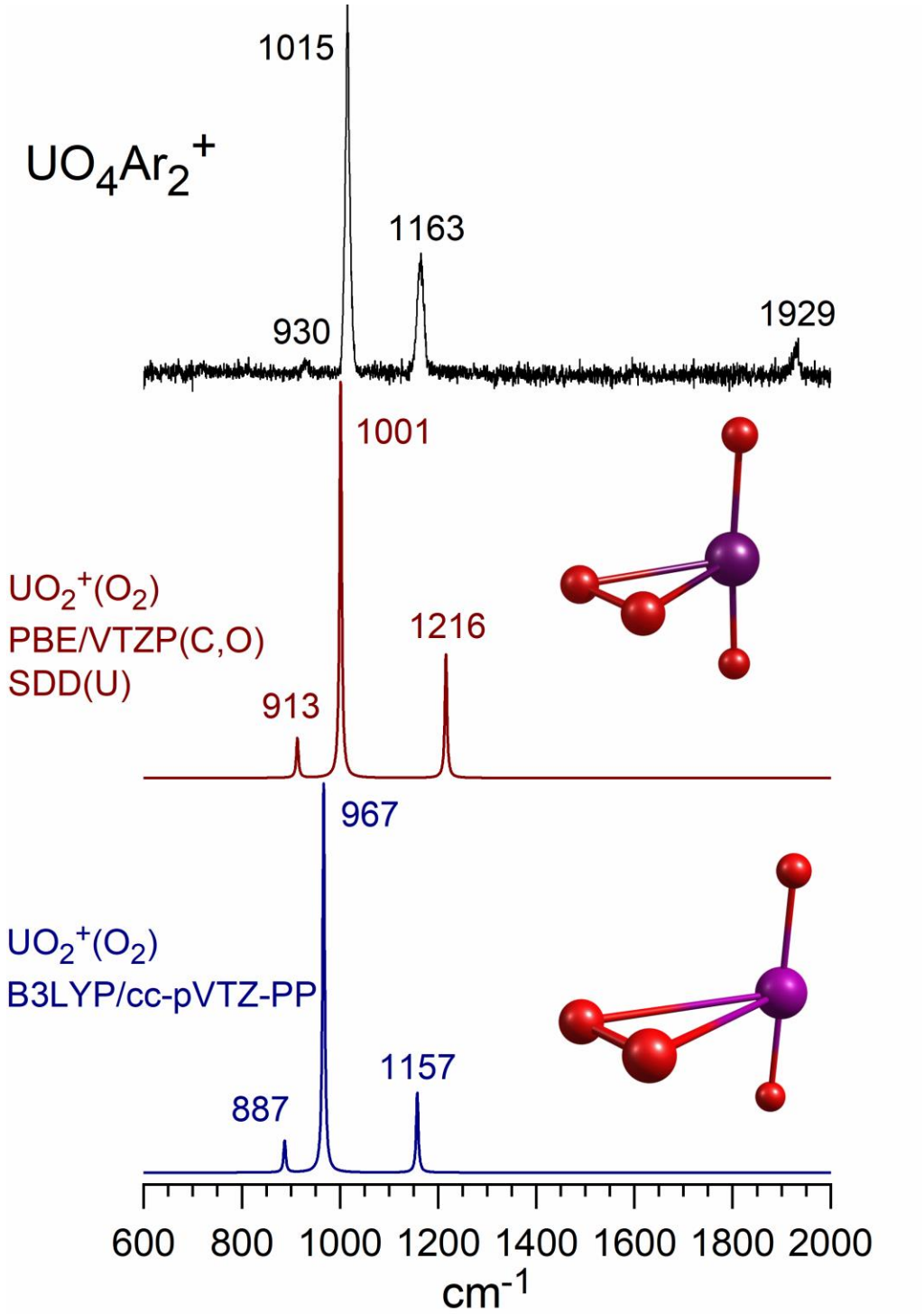

Figure 4.10. Infrared photodissociation spectrum of $U^+(O)_4$ with simulated spectra calculated at two levels of theory. The PBE functional with VTZP on carbon and oxygen and SDD on uranium are shown with B3LYP/cc–pVTZ–PP.

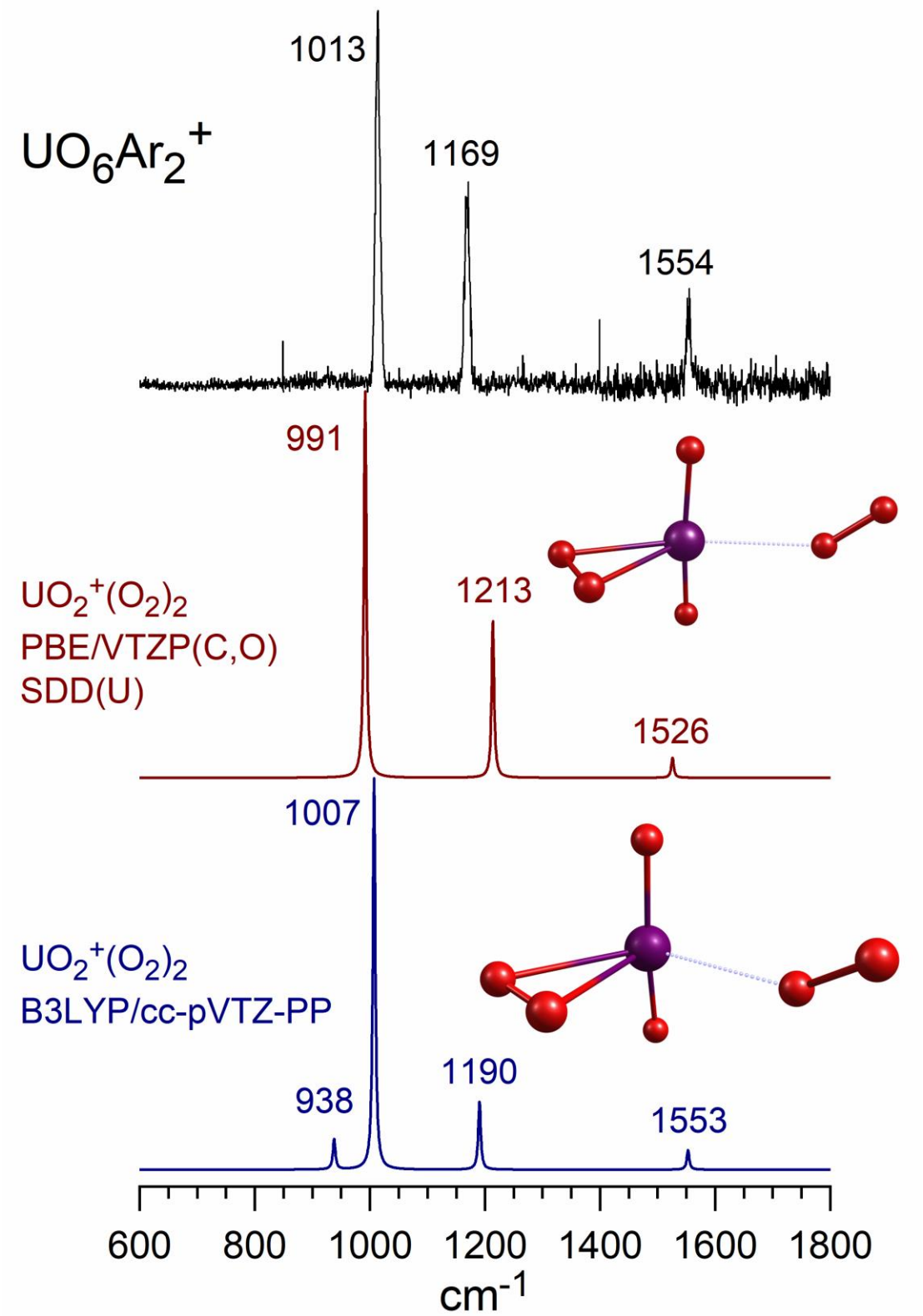

Figure 4.11. Infrared photodissociation spectrum of $U^+(O)_6$ with simulated spectra calculated at two levels of theory. The PBE functional with VTZP on carbon and oxygen and SDD on uranium are shown with B3LYP/cc–pVTZ–PP.

The errors in the vibrational frequency observed for prediction of $U^+(N_2)_n$ are larger with fewer ligands, though it is not clear why this should be the case. Any of the approximations that are used to make actinide theory on large molecules computationally affordable may be at fault. This includes the use of an ECP and the implicit neglect of core–valence correlation. The electronic state of U^+ is most likely better represented with a multireference wavefunction. Strong field spin–orbit interaction in uranium causes further coupling between states of different multiplicity. Multireference calculations and appropriate treatment of spin–orbit coupling are unaffordable in complexes containing more than two or three atoms in addition to uranium. While this level of theory appears to perform well in fully coordinated complexes, smaller complexes may require more rigorous treatment in the future.

CONCLUSIONS

Laser vaporization and supersonic expansion were used to produce $U^+(N_2)_n$ complexes for n = 1–8. These complexes were mass selected and studied via photodissociation in a mass spectrometer. Fixed frequency photodissociation shows that all molecular nitrogen bound to uranium is readily eliminated. Photodissociation to eliminate only N_2 and never N indicates a lack of insertion of U^+ into the N_2 bond to form uranium nitride or dinitride. A consistent ratio of photon energy to N_2 ligands eliminated across multiple complexes and laser powers was found with 355 and 532 nm photodissociation. This provided a convenient method of estimating an $U^+–N_2$ average bond dissociation energy of 12.1 ± 1.3 kcal/mol. The infrared photodissociation spectra show that the N_2 stretch becomes infrared active and red shifts 100 to 130 cm^{-1} because of interaction with uranium cation. Computations at the B3LYP/cc–pVTZ–PP level are used to predict that the sextet $U^+(N_2)_8$ is a fully coordinated with eight N_2 bound end on with cubic

coordination. These calculations were found to predict an exaggerated redshift for smaller complexes for which agreement between experiment and theory was not found. However, these calculations did correctly predict a fully coordinated complex. Furthermore, predictions of average BDE place it in the range 11.3–12.2 kcal/mol for n = 1–8. The predicted value is consistent between complexes of different size, and consistent with estimates of average U^+–N_2 BDE obtained with 355 and 532 nm fixed frequency photodissociation. Given the failure of theory to reproduce infrared spectra these seemingly accurate bond energies may be a fortuitous result, having no basis in a sound treatment of the electronic structure of the complex, and this issue certainly warrants further investigation. Future experiments will seek to validate the accuracy of this level of theory in predicting infrared spectra of gas phase U^+ complexes. Further research into the possible formation and spectroscopy of NUN^+ complexes or $U_nN_m^+$ clusters would be more broadly applicable.

AUTHOR INFORMATION

Corresponding author: Email: maduncan@uga.edu

ACKNOWLEDGEMENTS

We gratefully acknowledge the generous support for this work from the U.S. Department of Energy via Grant No. DE-SC0018835 and from the Air Force Office of Scientific Research through grant FA-9550-20-1-0327.

REFERENCES

1. Rundle, R. E.; Baenziger, N. C.; Wilson, A. S.; McDonald, R. A. The Structures of the Carbides, Nitrides and Oxides of Uranium. *J. Am. Chem. Soc.* **1948**, *70*, 99–105.
2. Katz, J. J.; Rabinowitch, E. *The Chemistry of Uranium the Element, Its Binary and Related Compounds*, Dover Publications, Inc.: New York, **1961**.
3. Katz, J. J.; Seaborg, G. T.; Morss, L. R. *The Chemistry of the Actinide Elements, 2nd ed*, Chapman and Hall: London, **1986**.
4. H. C. Aspinall, *Chemistry of the f–Block Elements*, Gordon and Breach, Amsterdam, **2001**.
5. Konings, R. J. M.; Morss, L. R.; Fuger, J. *The Chemistry of the Actinide and Transactinide Elements, 3rd ed.*, edited by L. R. Morss, N. M. Edelstein, and J. Fuger Springer: Dordrecht, **2006**.
6. Cotton, S. *Lanthanide and Actinide Chemistry*, John Wiley & Sons, Ltd.: Chichester, **2006**.
7. Lottermoser, B. *Mine Wastes: Characterization, Treatment and Environmental Impact*, Springer: London, **2007**.
8. Klein, C.; Dutrow, B. *Manual of Mineral Science*, John Wiley & Sons: Hoboken, NJ, **2008**.
9. Matthews, R. B.; Chidester, K. M.; Hoth, C. W.; Mason, R. E.; Petty, R. L. Fabrication and Testing of Uranium Nitride Fuel for Space Power Reactors. *J. Nucl. Mater.* **1988**, *151*, 345–356.
10. Morris, D. E.; Allen, P. G.; Berg, J. M.; Chisholm–Brause, C. J.; Conradson, S. D.; Donohoe, R. J.; Hess, N. J.; Musgrave, J. A.; Tait, C. D. Speciation of Uranium in

Fernald Soils by Molecular Spectroscopic Methods: Characterization of Untreated Soils. *Environ. Sci. Technol.* **1996**, *30*, 2322–2331.

11. Rogozkin, B. D.; Stepennova, N. M.; Bergman, G. A.; Proshkin, A. A. Thermochemical Stability, Radiation Testing, Fabrication, and Reprocessing of Mononitride Fuel. *At. Energy* **2003**, *95*, 835–844.
12. Streit, M.; Ingold, F. Nitrides as a Nuclear Fuel Option. *J. Eur. Ceram. Soc.* **2005**, *25*, 2687– 2692.
13. Fox, A. R., Bart, S. C., Meyer, K. & Cummins, C. C. Towards uranium catalysts. *Nature* **2008**, *455*, 341–349.
14. Maher, K.; Bargar, J. R.; Brown, G. E., Jr. Environmental Speciation of Actinides. *Inorg. Chem.* **2013**, *52*, 3510–3532.
15. Liddle, S. T. The Renaissance of Non–Aqueous Uranium Chemistry. *Angew. Chem. Int. Ed.* **2015**, *54*, 8604–8641.
16. Potocki, M.; Mayewski, P. A.; Kurbatov, A. V.; Simoes, J. C.; Dixon, D. A.; Goodwin, I.; Carleton, A. M.; Handley, M. J.; Jana, R.; Korotkikh, E. V. Recent Increase in Antarctic Peninsula Ice Core Uranium Concentrations. *Atmospheric Environ.* **2016**, *140*, 381–385.
17. Cleaves, P. A.; Kefalidis, C. E.; Gardner, B. M.; Tuna, F.; McInnes, E. J. L.; Lewis, W.; Maron, L.; Liddle, S. T. Terminal Uranium(V/VI) Nitride Activation of Carbon Dioxide and Carbon Disulfide: Factors Governing Diverse and Well–Defined Cleavage and Redox Reactions. *Chem. Eur. J.* **2017**, *23*, 2950–2959.
18. Reynolds, J. G.; Cooke, G. A.; Page, J. S.; Warrant, R. W. Uranium–Bearing Phases in Hanford Nuclear Waste. *J. Radioanal. Nucl. Chem.* **2018**, *316*, 289–299.

19. Steinhauser, G. Anthropogenic Radioactive Particles in the Environment. *J. Radioanal. Nucl. Chem.* **2018**, *318*, 1629–1639.

20. Allen, D. J.; Blair, S. R.; Millerr, M. G.; Nelson, M. E.; Evaluation of Non–Oxide Fuel for Fission–Based Nuclear Reactors on Spacecraft. *Nucl. Technol.* **2019**, *205*, 755–765.

21. Kashcheev, V. A.; Chernikov, M. A.; Shadrin, A. Y. Radwaste Characteristics in Uranium–Plutonium Nuclear Fuel Production. *At. Energy* **2020**, *128*, 95–102.

22. Bauschlicher, C. W., Jr.; Petterson, L. M.; Siegbahn, P. E. M. The Bonding in FeN_2, FeCO, and Fe_2N_2: Model Systems for Side–On bonding of CO and N_2. *J. Chem. Phys*. **1987**, *87*, 2129–2137.

23. Khan, F. A.; Steele, D. L.; Armentrout, P. B.Ligand Effects in Organometallic Thermochemistry: The Sequential Bond Energies of $Ni(CO)_x^+$ and $Ni(N_2)_x^+$ (x = 1–4) and $Ni(NO)_x^+$ (x = 1–3). *J. Phys. Chem*. **1995**, *99*, 7819–7828.

24. Tjelta, B. L.; Armentrout, P. B. Gas–Phase Metal Ion Ligation: Collision–Induced Dissociation of $Fe(N_2)_x^+$ (x = 1–5) and $Fe(CH_2O)_x^+$ (x = 1–4). *J. Phys. Chem. A* **1997**, *101*, 2064–2073.

25. Tjelta, B. L.; Walter, D.; Armentrout, P. B.Determination of Weak Fe^+–L Bond Energies (L = Ar, Kr, Xe, N_2, and CO_2) by Ligand Exchange Reactions and Collision–Induced Dissociation. *Int. J. Mass. Spectrom.* **2001**, *204*, 7–21.

26. Asher, R. L.; Buthelezi, B.; Brucat, P. J. Optical Excitation of $Co^+ \cdot N_2$. *J. Phys. Chem*. **1995**, *99*, 1068–1072.

27. Heinemann, C.; Schwarz, J.; Schwarz, H. Ground state of $Co(N_2)^+$. *J. Phys. Chem*. **1996**, *100*, 6088–6092.

28. Andrews, L.; Bare, W. D.; Chertihin, G. V. Reactions of Laser–Ablated V, Cr, and Mn Atoms with Nitrogen Atoms and Molecules. Infrared Spectra and Density Functional Calculations on Metal Nitrides and Dinitride Complexes. *J. Phys. Chem. A* **1997**, *101*, 8417–8427.

29. Duarte, A. D.; Salahub, D. R.; Haslett, T.; Moskovits, M. $Fe(N_2)_n$ (n = 1–5): Structure, Bonding, and Vibrations from Density Functional Theory. *Inorg. Chem.* **1999**, *38*, 3895–3903.

30. Parrish, S. H.; Van Zee, R. J.; Weltner, W., Jr. Vanadium and Niobium Hexadinitrogen and Hexacarbonyl Complexes: Electron–Spin–Resonance Spectra at 4 K. *J. Phys. Chem. A* **1999**, *103*, 1025–1028.

31. Pillai, E. D.; Jaeger, T. D.; Duncan, M. A. IR Spectroscopy and Density Functional Theory of Small $V^+(N_2)_n$ Complexes. *J. Phys. Chem. A*, **2005**, *129*, 3521–3526.

32. Pillai, E. D.; Jaeger, T. D.; Duncan, M. A. IR Spectroscopy of $Nb^+(N_2)_n$ Complexes: Coordination, Structures, and Spin States. *J. Am. Chem. Soc.*, **2007**, *129*, 2297–2307.

33. Brathwaite, A. D.; Abbott–Lyon, H. L.; Duncan, M. A. Distinctive Coordination of CO vs N_2 to Rhodium Cations: An Infrared and Computational Study. *J. Phys. Chem. A* **2016,** *120*, 7659–7670.

34. Lu, Z.–H.; Jiang, L.; Xu, Q. A Combined Experimental and Theoretical Study of Iron Dinitrogen Complexes: $Fe(N_2)$, $Fe(NN)_x$ (x = 1−5), and $Fe(NN)_3^-$. *J. Phys. Chem. A* **2010,** *114*, 2157–2163.

35. Lu, Z.–H.; Jiang, L.; Xu, Q. Reactions of Laser–Ablated Nb and Ta Atoms with N_2: Experimental and Theoretical Study of $M(NN)_x$ (M = Nb, Ta; x = 1−4) in Solid Neon. *J. Phys. Chem. A* **2010,** *114*, 6837–6842.

36. Xie, H; Shi, L.; Xing, X.; Tang. Z. Infrared Photodissociation Spectroscopy of $M(N_2)_n^+$ (M = Y, La, Ce; n = 7–8) in the Gas Phase. *Phys. Chem. Chem. Phys.* **2016,** *18*, 4444–4450.

37. Ding, K.; Xu, H.; Yang, Y.; Li, T.; Chen, Z.; Ge, Z.; Zhu, W.; Zheng, W. Mass Spectrometry and Theoretical Investigation of VN_n^+ (n = 8, 9, and 10) Clusters. *J. Phys. Chem. A* **2018,** *122*, 4687–4695.

38. Yoo, H.–W.; Choi, C.; Cho, S. G.; Jung, Y.; Choi, M. Y. Infrared Spectroscopy and Density Functional Calculations on Titanium–Dinitrogen Complexes. *Chem. Phys. Lett.* **2018,** *698*, 163–170.

39. Gibson, J. K. Gas–Phase Chemistry of Actinide Ions: Probing the Distinctive Character of the *5f* Elements. *Int. J. Mass Spectrom.* **2002**, *214*, 1–21.

40. Evans, W. J.; Kozimor, S. A.; Ziller, J. W. Molecular Octa–Uranium Rings with Alternating Nitride and Azide Bridges. *Science* **2005**, *309*, 1835–1838.

41. Fox, A. R.; Cummins, C. C. Uranium–Nitrogen Multiple Bonding: The Case of a Four–Coordinate Uranium(VI) Nitridoborate Complex. *J. Am. Chem. Soc.* **2009**, *131*, 5716–5717.

42. Fortier, S.; Wu, G.; Hayton, T. W. Synthesis of a Nitrido–Substituted Analogue of the Uranyl Ion, $[N{=}U{=}O]^+$. *J. Am. Chem. Soc.* **2010**, *132*, 6888–6889.

43. Thomson, R. K.; Cantat, T.; Scott, B. L.; Morris, D. E.; Batista, E. R.; Kiplinger, J. L. Uranium Azide Photolysis Results in C–H Bond Activation and Provides Evidence for a Terminal Uranium Nitride. *Nat. Chem.* **2010**, *2*, 723–729.

44. King, D. M.; Tuna, F.; McInnes, E. J. L.; McMaster, J.; Lewis, W.; Blake, A. J.; Liddle, S. T. Synthesis and Structure of a Terminal Uranium Nitride Complex. *Science* **2012**, *337*, 717–720.

45. King, D. M.; Tuna, F.; McInnes, E. J. L.; McMaster, J.; Lewis, W.; Blake, A. J.; Liddle, S. T. Isolation and Characterization of Uranium(VI)–Nitride Triple Bond. *Nat. Chem.* **2013**, *5*, 482–488.

46. King, D. M.; Liddle, S. T. Progress in Molecular Uranium–Nitride *Chemistry. Coord. Chem. Rev.* **2014**, *2*, 266–267.

47. Hayton, T. W. Recent Developments in Actinide–Ligand Multiple Bonding. *Chem. Commun.* **2013**, *49*, 2956–2973

48. Rudel, S. S.; Deubner, H. L.; Müller, M.; Karttunen, A. J.; Kraus, F. Complexes Featuring a Linear [N≡U≡N] Core Isoelectronic to the Uranyl Cation. *Nat. Chem.* **2020**, *12*, 962–967.

49. Heinemann, C.; Cornehl, H. H.; Schwarz, H. Hydrocarbon Activation by "Bare" Uranium Cations: Formation of a Cationic Uranium–Benzene Complex from Three Ethylene Units. *J. Organomet. Chem.* **1995**, *501*, 201–209.

50. Cornehl, H. H.; Wesendrup, R.; Diefenbach, M.; Schwarz, H. A Comparative Study of Oxo–Ligand Effects in the Gas–Phase Chemistry of Atomic Lanthanide and Actinide Cations. *Chem. Eur. J.* **1997**, *3*, 1083–1090.

51. Jackson, G. P.; Gibson, J. K.; Duckworth, D. C. Gas–Phase Reactions of Bare and Oxo–Ligated Actinide and Lanthanide Cations with Pentamethylcyclopentadiene Studied in a Quadrupole Ion Trap Mass Spectrometer. *Int. J. Mass. Spectrom.* **2002**, *220*, 419–441.

52. Jackson, G. P.; King, F. L.; Goeringer, D. E.; Duckworth, D. C. Gas–Phase Reactions of U^+ and U^{2+} with O_2 and H_2O in a Quadrupole Ion Trap. *J. Phys. Chem. A* **2002**, *106*, 7788–7794.

53. Groenewold, G. S.; van Stipdonk, M. J.; Gresham, G. L.; Chien, W.; Bulleigh, K.; Howard, A. CID MS/MS of Desferrioxamine Siderophore Complexes from ESI of UO_2^{2+}, Fe^{3+} and Ca^{2+} Solutions. *J. Mass Spectrom.* **2004**, *39*, 752–761.

54. Groenewold, G. S.; Cossel, K. C.; Gresham, G. L.; Gianotto, A. K.; Appelhans, A. D.; Olson, J. E.; van Stipdonk, M. J.; Chien, W. Binding of Molecular O_2 to Di– and Tri–Ligated $[UO_2]^+$. *J. Am. Chem. Soc.* **2006**, *128*, 3075–3084.

55. van Stipdonk, M. J.; Michelini, M. del C.; Plaviak, A.; Martin, D.; Gibson, J. K. Formation of Bare UO_2^{2+} and NUO^+ by Fragmentation of Gas–Phase Uranyl–Acetonitrile Complexes. *J. Phys. Chem. A,* **2014**, *118*, 7838–7846.

56. van Stipdonk, M. J.; Hanley, C.; Perez, E.; Pestok, J.; Mihm, P.; Corcovilos, T. A. Collision–Induced Dissociation of Uranyl–Methoxide and Uranyl–Ethoxide Cations: Formation of UO_2H^+ and Uranyl–Alkyl Product Ions. *Rapid Comm. Mass Spectrom.* **2016**, *30,* 1879–1890

57. de Jong, W. A.; Dau, P.; Wilson, R.; Marçalo, J.; van Stipdonk, M. J.; Corcovilos, T.; Berden, G.; Martens, J.; Oomens, J.; Gibson, J. K. Revealing Disparate Chemistries of Protactinium and Uranium. Synthesis of the Molecular Uranium Tetroxide Anion, UO^{4-}. *Inorg. Chem*. **2017**, *56*, 3686–3694.

58. Pillai, E. D.; Molek, K. S.; Duncan, M. A. Growth and Photodissociation of $U^+(C_6H_6)_n$ (n = 1–3) and $UO_m^+(C_6H_6)$ (m = 1, 2) Complexes. *Chem. Phys. Lett.* **2005**, *405*, 247–251.

59. Marks, J. H.; Kahn, P.; Vasiliu, M; Dixon, D.; Duncan, M. A. Photodissociation and Theory to Investigate Uranium Oxide Cluster Cations. *J. Phys. Chem. A* **2020**, *124*, 1940–1953.

60. Michelini, M. del C.; Russo, N.; Sicilia, E. How Can Uranium Ions (U^+, U^{2+}) Activate the O–H Bond of Water in the Gas Phase? *Angew. Chem.* **2006**, *45*, 1095–1099.

61. Michelini, M. del C.; Russo, N.; Sicilia, E. Gas–Phase Chemistry of Actinides Ions: New Insights into the Reaction of UO^+ and UO^{2+} with Water. *J. Am. Chem. Soc.* **2007**, *129*, 4229–4239.

62. Rios, D.; Gibson, J. K. Activation of Gas Phase Uranyl Diacetone Alcohol Coordination Complexes by Spectator Ligand Addition. *Eur. J. Inorg. Chem.* **2012**, *2012*, 1054–1060.

63. Green, D.W.; Reedy, G.T. The Identification of UN in Ar matrices. *J. Chem. Phys*., **1976**, *65*, 2921–2922.

64. Hunt, R. D.; Yustein, J. T.; Andrews, L. Matrix Infrared Spectra of NUN Formed by the Insertion of Uranium Atoms into Molecular Nitrogen. *J. Chem. Phys.* **1993**, *98*, 6070–6074.

65. Kushto, G.P.; Souter, P.F.; Andrews, L.; Neurock, M. A. Matrix Isolation FT–IR and Quasirelativistic Density Functional Theory Investigation of the Reaction Products of Laser–Ablated Uranium Atoms with NO, NO_2 and N_2O. *J. Chem. Phys.*, **1997**, *106*, 5894–5903.

66. Zhou, M.; Andrews, L., Infrared Spectra and Pseudopotential Calculations for NUO^+, NUO, and NThO in solid neon, *J. Chem. Phys.*, **1999**, *111*, 11044–11049.

67. Andrews, L.; Wang, X.; Lindh, R.; Roos, B.O.; Marsden, C.J., Simple NUF_3 and PUF_3 Molecules with Triple Bonds to Uranium. *Angew. Chem. Int. Ed.*, **2008**, *47*, 5366–5370.

68. Wang, X., Andrews, L., Vlaisavljevich, B. & Gagliardi, L. Combined Triple and Double Bonds to Uranium: The N≡U=N–H Uranimine Nitride Molecule Prepared in Solid Argon. *Inorg. Chem.* **2011**, *50*, 3826–3831.

69. Andrews, L., Wang, X., Gong, Y., Vlaisavljevich, B. & Gagliardi, L. Infrared Spectra and Electronic Structure Calculations for the NUN(NN)1−5 and NU(NN)1−6 Complexes in Solid Argon. *Inorg. Chem.* **2013**, *52*, 9989−9993.

70. Andrews, L.; Wang, X.; Gong, Y.; Kushto, G. P.; Vlaisavljevich, B.; Gagliardi, L Infrared Spectra and Electronic Structure Calculations for NN Complexes with U, UN and NUN in Solid Argon, Neon and Nitrogen. *J. Phys. Chem. A* **2014**, *118*, 5289−5303.

71. Sankaran, K.; Sundararajan, K.; Viswanathan, K.S. A Matrix Isolation FTIR Investigation of Laser–Ablated Uranium Oxide in Argon and Nitrogen Matrices. *Bull. Mater. Sci.*, **1999**, *22*, 785–790

72. Sankaran, K.; Sundararajan, K.; Viswanathan, K.S. Matrix Isolation Infrared Studies of the Reactions of Laser–Ablated Uranium with N_2: Reactions Beyond Insertion into N_2. *J. Phys. Chem. A*, **2001**, *105*, 3995–4001.

73. Heaven, M. C.; Nicolai, J.–P.; Riley, S. J.; Parks, E. K. Rotationally Resolved Electronic Spectra for Uranium Monoxide. *Chem. Phys. Lett.* **1985**, *119*, 229–233.

74. Allen, G. C.; Holmes, N. R. Mixed–Valency Behavior in Some Uranium–Oxides Studies by X–Ray Photoelectron Spectroscopy. *Can. J. Spectrosc.* **1993**, *38*, 124–130.

75. Kaledin, L. A.; McCord, J. E.; Heaven, M. C. Laser Spectroscopy of UO: Characterization and Assignment of States in the 0 to 3 eV Range, with a Comparison to the Electronic Structure of ThO. *J. Mol. Spec.* **1994**, *164*, 27–65.

76. Kaledin, L. A.; Heaven, M. C. Electronic Spectroscopy of UO. *J. Mol. Spec.* **1997**, *185*. 1–7.

77. Lue, C. J.; Jin, J.; Ortiz, M. J.; Rienstra–Kiracofe, J. C.; Heaven, M. C. Electronic Spectroscopy of UO_2 Isolated in a Solid Ar Matrix. *J. Am. Chem. Soc.* **2004**, *126*, 1812–1815.

78. Han, J.; Goncharov, V.; Kaledin, L. A.; Komissarov, A. V.; Heaven, M. C. Electronic Spectroscopy and Ionization Potential of UO_2 in the Gas Phase. *J. Phys. Chem.* **2004**, *120*, 5155–5163.

79. Gagliardi, L.; Heaven, M. C.; Krogh, J. W.; Roos, B. O. The Electronic Spectrum of the UO_2 Molecule. *J. Am. Chem. Soc.* **2005**, *127*, 86–91.

80. Goncharov, V.; Kaledin, L. A.; Heaven, M. C. Probing the Electronic Structure of UO^+ with High–Resolution Photoelectron Spectroscopy. *J. Chem. Phys.* **2006**, *125*, 133202–1 – 133202.

81. Heaven, M. C. Probing Actinide Electronic Structure using Fluorescence and Multi–Photon Ionization Spectroscopy. *Phys. Chem. Chem. Phys.* **2006**, *8*, 4497–4509.

82. Merritt, J. M.; Han, J.; Heaven, M. C. Spectroscopy of the UO_2^+ Cation and the Delayed Ionization of UO_2. *J. Chem. Phys.* **2008**, *128*, 084304.

83. Gaoziang, L.; Zhang, C.; Ciborowski, S. M.; Asthana, A.; Cheng, L.; Bowen, K. H. Mapping the Electronic Structure of the Uranium(VI) Dinitride Molecule, UN_2. *J. Phys. Chem. A* **2020**, *124*, 6486–6492.

84. Dietz, T. G.; Duncan, M. A.; Smalley, R. E.; Cox, D. M.; Horsley, J. A.; Kaldor, A. Spectral Narrowing and Infrared–Laser Fragmentation of Jet–Cooled $UO_2(hfaa)_2$ TMP and $UO_2(hfaa)_2$ THF: Volatile Uranyl Compounds. *J. Chem. Phys.* **1982**, *77*, 4417–4426.

85. Ricks, A. M.; Gagliardi, L.; Duncan, M. A. Infrared Spectroscopy of Extreme Coordination: The Carbonyls of U^+ and UO_2^+. *J. Am. Chem. Soc.* **2010**, *132*, 15905–15907.

86. Ricks, A. M.; Gagliardi, L.; Duncan, M. A. Uranium Oxo and Superoxo Cations Revealed using Infrared Spectroscopy in the Gas Phase. *J. Phys. Chem. Lett.* **2011**, *2*, 1662–1666.

87. Groenewold, G. S.; Gianotto, A. K.; Cossel, K. C.; van Stipdonk, M. J.; Moore, D. T.; Polfer, N.; Oomens, J.; de Jong, W. A.; Visscher, L. Vibrational Spectroscopy of Mass Selected $[UO_2(ligand)_n]^{2+}$ Complexes in the Gas Phase: Comparison with Theory. *J. Am. Chem. Soc.* **2006**, *128*, 4802–4813.

88. Groenewold, G. S.; Oomens, J.; de Jong, W. A.; Gresham, G. L.; McIlwain, M. E.; van Stipdonk, M. J. Vibrational Spectroscopy of Anionic Nitrate Complexes of UO_2^{2+} and Eu^{3+} Isolated in the Gas Phase. *Phys. Chem. Chem. Phys.* **2008**, *10*, 1192–1202.

89. Groenewold, G. S.; van Stipdonk, M. J.; Oomens, J.; de Jong, W. A.; Gresham, G. L.; McIlwain, M. E. Vibrational Spectra of Discrete UO_2^{2+} Halide Complexes in the Gas Phase. *Int. J. Mass Spectrom*. **2010**, *297*, 67–75.

90. Groenewold, G. S.; van Stipdonk, M. J.; Oomens, J. de Jong, W. A.; McIlwain, M. E. The Gas–Phase Bis–Uranyl Nitrate Complex $[(UO_2)_2(NO_3)_5]^-$: Infrared Spectrum and Structure. *Int. J. Mass Spectrom*. **2011**, *308*, 175–180.

91. de Jong, W. A.; Harrison, R. J.; Nichols, J. A.; Dixon, D, A. Fully Relativistic Correlated Benchmark Results for Uranyl and a Critical Look at Relativistic Effective Core Potentials for Uranium. *Theor. Chem. Acc.* **2001**, *107*, 22–26.

92. Gutowski, K. E.; Cocalia, V. A.; Griffin, S. T.; Bridges, N. J.; Dixon, D. A.; Rogers, R. D. Interactions of 1–Methylimidazole with $UO_2(CH_3CO_2)_2$ and $UO_2(NO_3)_2$: Structural, Spectroscopic, and Theoretical Evidence for Imidazole Binding to the Uranyl Ion. *J. Am. Chem. Soc.* **2007**, *129*, 526–536.

93. Dolg, M.; Cao, X. Accurate Relativistic Small–Core Pseudopotentials for Actinides. Energy Adjustments for Uranium and First Applications to Uranium Hydride. *J. Phys. Chem. A* **2009**, *113*, 12573–12581.

94. Wang, X. F.; Andrews, L.; Thanthiriwatte, K. S.; Dixon, D. A. Infrared Spectra of H_2ThS and H_2US in Noble Gas Matrixes: Enhanced H–An–S Covalent Bonding. *Inorg. Chem.* **2013**, *52*, 10275–10285.

95. Odoh, S. O.; Govind, N.; Schreckenbach, G.; de Jong, W. A. Cation–Cation Interactions in $[(UO_2)_2(OH)_n]^{4-n}$ Complexes. *Inorg. Chem.* **2013**, *52*, 11269–11279.

96. Vent–Schmidt, T.; Andrews, L.; Thanthiriwatte, K. S.; Dixon, D. A.; Riedel, S. Reaction of Laser–Ablated Uranium and Thorium Atoms with H_2Se: A Rare Example of Selenium Multiple Bonding. *Inorg. Chem.* **2015**, *54*, 9761–9769.

97. Haiges, R.; Vasiliu, M.; Dixon, D. A.; Christe, K. O. The Uranium(VI) Oxoazides $[UO_2(N_3)_2 \cdot CH_3CN]$, $[(bipy)_2(UO_2)_2(N_3)_4]$, $[(bipy)UO_2(N_3)_3]^-$, $[UO_2(N_3)_4]^{2-}$, and $[(UO_2)_2(N_3)_8]^{4-}$. *Chem. Eur. J.* **2016**, *23*, 652–664.

98. Flores, L. A.; Murphy, J. G.; Copeland, W. B.; Dixon, D. A. Reaction of CO_2 with UO_3 Nanoclusters. *J. Phys. Chem. A* **2017**, *121*, 8518–8524.

99. Andrews, L.; Cho, H. G.; Thanthiriwatte, K. S.; Dixon, D. A. Thorium and Uranium Hydride Phosphorus and Arsenic Bearing Molecules with Single and Double Actinide–Pnictogen and Bridged Agnostic Hydrogen Bonds. *Inorg. Chem.* **2017**, *56*, 2949–2957.

100. Wacker, J. N.; Vasiliu, M.; Huang, K.; Baumbach, R. E.; Bertke, J. A.; Dixon, D. A.; Knope, K. E. Uranium(IV) Chloride Complexes: UCl_6^{2-} and an Unprecedented $U(H_2O)_4Cl^{4-}$ Structural unit. *Inorg. Chem.* **2017**, *56*, 9772–9780.

101. Fang, Z. T.; Garner, E. B.; Dixon, D. A.; Gong, Y.; Andrews, L.; Liebov, B. Laser–Ablated U Atom Reactions with CN_2 to Form UNC, $U(NC)_2$, and $U(NC)_2$: Matrix Infrared Spectra and Quantum Chemical Calculations. *J. Phys. Chem. A* **2018**, *122*, 516–528.

102. Adeyiga, O.; Suleiman, O.; Dandu, N. K.; Odoh, S. O. Ground–State Actinide Chemistry with Scalar–Relativistic Multiconfiguration Pair–Density Functional Theory. *J. Chem. Phys.* **2019**, *151*, 134102.

103. Soto–Guerrero, J.; Gajdošová, D.; Havel, J. Uranium Oxide Clusters by Laser Desorption Ionization During MALDI–TOF MS Analysis of Uranium (VI). *J. Radianalyt. & Nucl. Chem.* **2001**, *249*, 139–143.

104. Qiu, J.; Burns, P. C. Clusters of Actinides with Oxide, Peroxide or Hydroxide Bridges. *Chem. Rev.* **2013**, *113*, 1097–1120.

105. Wang, X.; Qiu, R. Z.; Long, Z.; Lu, L; Hu, Y.; Liu, K. Z.; Zhang, P. C. Chemical State of U in U–N–O Ternary System from First–Principles Calculations. *J. Phys. Chem. C* **2019**, *123*, 17155–17162.

106. Denning, R. G. Electronic Structure and Bonding in Actinyl Ions and their Analogs. *J. Phys. Chem. A* **2007**, *111*, 4125– 4143.

107. Anderson, N. H.; Xie, J.; Ray, D.; Zeller, M.; Gagliardi, L.; Bart, S. C. Elucidating Bonding Preferences in Tetrakis(Imido)Uranate(VI) Dianions. *Nat. Chem.* **2017**, *9*, 850–855.

108. Peterson, K. A. Correlation Consistent Basis Sets for Actinides. I. The Thorium and Uranium Atoms. *J. Chem. Phys.* **2015**, *142*, 074105.

109. Dolg, M.; Cao, X. Accurate Relativistic Small–Core Pseudopotentials for Actinides. Energy Adjustment for Uranium and First Applications to Uranium Hydride. *J. Phys. Chem. A* **2009**, *113*, 12573–12581.

110. Duncan, M. A. Invited Review Article: Laser Vaporization Cluster Sources. *Rev. Sci. Inst.* **2012**, *83*, 041101.

111. Duncan, M. A. Reflectron Time–of–Flight Mass Spectrometer for Laser Photodissociation. *Rev. Sci. Instrum.* **1992**, *63*, 2177–2186.

112. Frisch, M. J. et al. *Gaussian 09 (Revision* D.01); Gaussian, Inc.: Wallingford CT, **2013**.

CHAPTER 5

CONCLUSION

The goal of the research presented in this dissertation is to develop a better understanding of the chemistry of uranium. This is motivated by the possibility of novel chemistry involving the f orbitals, and the implications such chemistry may have towards environmental remediation and new catalysts. The chemistry of two uranium bearing systems has been explored. In chapter 3 the stability of cluster cations of uranium oxides were examined with fixed–frequency photodissociation. In chapter 4 the structure of uranium complexes with molecular nitrogen was determined with tunable infrared photodissociation, and the bond energies were experimentally determined using fixed frequency photodissociation.

Clusters of $U_nO_m^+$ were mass selected no hyphen and photodissociated with 355 nm laser light. This invariably yielded fragment cations $UO_2^+(UO_3)_n$, which were determined to represent the most stable stoichiometry for cluster cations containing uranium oxides.[1] Photodissociation of $(UO_3)_n^+$ was found to produce additional fragment cations with the same 3:1 ratio of O:U. This is presumed to result from increased stability of $(UO_3)_n$ which is eliminated during photodissociation of $(UO_3)_n^+$. The structure of the complexes was investigated with computational quantum chemistry. B3LYP/cc–pVTZ–PP calculations predict that these $(UO_3)_n$ clusters are composed of repeating units of UO_2, which is linear and strongly resembles uranyl. These UO_2 units in the =6 oxidation state bind through oxygen atoms bonding to two uranium atoms simultaneously. Cluster cations contain charge which is highly localized to the f orbitals of one uranium, resulting in structures containing $(UO_3)_n$ with a UO^+ charge center in a =5

oxidation state. The consistent stability of $(UO_3)_n$ and the +6 oxidation state marks a sharp departure from the behavior of bulk uranium oxides. Naturally occurring uranium is found as pitchblende, UO_2, containing uranium in the +4 oxidation state. On exposure to air pitchblende oxidizes U_3O_8 containing uranium in both the +5 and +6 oxidation states. The apparent stability of multiple oxidation states of uranium is a characteristic of the bulk material, and as particle size approaches the size of clusters studied only the +6 oxidation state is stable in neutral clusters.

Complexes of $U^+(N_2)_n$ were studied with mass–selected infrared photodissociation spectroscopy. The mass spectrum shows $U^+(N_2)_8$ is intense relative to larger complexes, which indicates that it represents a fully coordinated complex. Fixed frequency photodissociation with 355 and 532 nm revealed a consistent ratio of photon energy to the number of N_2 eliminated. This allowed for a measurement of $U^+(N_2)$ bond energy of 12.1 ± 1.3 kcal/mol. Furthermore, photodissociation with an excess of photon energy and laser fluence resulted in elimination only of even numbers of nitrogen atoms. Had there been NUN^+ present loss of an odd number of nitrogen atoms should have been observed. Because the infrared photon energy is too low to reach the bond dissociation energy (BDE) of 12.1 ± 1.3 kcal/mol, the infrared spectra were likely obtained through multiphoton absorption. These spectra reveal that bonding to U^+ causes the N_2 stretch to become IR active and red shifts it by 100–130 cm^{-1}. $U^+(N_2)_n$ (n = 1–8) $NUN^+(N_2)_{n-1}$ (n = 1–3) were studied computationally with B3LYP/cc–pVTZ–PP. Side–on bonds allow U^+ to interact with the π system of N_2 but is not energetically favorable and was not observed spectroscopically. Insertion of U^+ into N_2 was also found to result in a rise in energy despite the stability of UN_2. End on bonding of N_2 to $^6U^+$ was found to result in the lowest energy isomer for all values of n. This is predicted to result in a coordination that first builds to a trigonal bipyramid for n = 5, then incorporation of additional N_2 results in a cubic coordination for n = 8.

The $U^+(N_2)$ BDE was predicted to be 11.3–12.2 kcal/mol for n = 1–8, which is in good agreement with experiment. The infrared spectra predicted by these calculations were found to agree with experiment well in fully coordinated complexes such as $U^+(N_2)_8$. Comparison to previously measured gas phase infrared spectra also revealed good agreement between predictions made by this level of theory and $U^+(CO)_8$ and $UO_2^+(CO)_5$. A systematic underprediction of vibrational frequencies of about 20 cm^{-1} was identified. However, in partially coordinated complexes these calculations failed to produce a satisfactory prediction of infrared spectra. Infrared absorption for partially coordinated complexes is consistently predicted over 100 cm^{-1} to the red of the observed peaks.

There is an urgent need for gas phase spectroscopy of uranium ion containing complexes, both so that it can be better understood and so that computational methods can be improved. The number of researchers working in this field is highly limited. Wang and coworkers have measured the photoelectron spectra to investigate the electronic structure of several important uranium containing ions.[2–7] This research is intended to study uranium oxides and halides, both of which are common in the mining and processing or uranium. Additional photoelectron spectra have been measured by Heaven and coworkers, and Bowen and coworkers.[8–21] Research using photoelectron and photoionization is limited in scope by the accuracy with which the complicated electronic structure of uranium can be treated computationally. Most research using gas phase electronic spectroscopy techniques on uranium is limited to diatomic and triatomic systems where expensive calculations can be implemented. Alternatively, the electronic spectroscopy of uranium hexahalides and dioxides generally contains uranium in the +6 oxidation state. Uranium in the +6 oxidation state is closed shell, having shared all valence electrons in ionic bonds, resulting in significant simplification to observed spectra.

Additional gas phase spectroscopy has been published by van Stipdonk, Oomens, Groenewald, Gibson, and coworkers in the infrared.[22–31] These spectra use the FELIX free electron laser, and generally have broad infrared transitions. Use of an electrospray source on this instrument results in ions which are substantially hotter than those produced in a supersonic expansion. Furthermore, electrospray ionization generally uses an aqueous sample which results in the exclusive formation of uranyl. While the ubiquity of uranyl complexes in aqueous chemistry means that the study of their spectroscopy is valuable, the study of uranium cation complexes has been neglected. Gas phase infrared spectra published by Duncan and coworkers are well resolved because of the narrower linewidth afforded by an OPO/OPA laser. [32,33] The use of supersonic expansion cools ions and reduces the number of occupied rovibrational states also aids in obtaining well resolved spectra. Future implementation of OPO lasers operating in the visible and ultraviolet open the possibility of electronic photodissociation spectroscopy of cold ions in the future.

To our knowledge, the publication of spectra of $U^+(N_2)_n$ marks the first publication of gas phase spectra of partially coordinated U^+ complexes. Computational treatment that can accurately predict infrared spectra of fully coordinated complexes produces unsatisfactory results in smaller complexes. This discrepancy may not result simply from the degree of coordination but may also result from any of the approximations employed. Inexpensive computational treatment of relatively large molecules like $U^+(N_2)_8$ requires the neglect of multireference electronic states, spin–orbit and spin–spin couplings, and relativistic effects on valence electrons. This is in addition to more commonly employed tools like scaling harmonic frequencies, frozen core approximation, and the Born–Oppenheimer approximation. Investigation into the source of this computational error is the next step in furthering the research on gas phase U^+ chemistry.

Quantum chemistry calculations employing various approximations need to be benchmarked against experimental spectra of gas phase uranium complexes with a variety of ligands and coordination numbers. There are not enough known infrared spectra to make the results of such a computational study meaningful, so more gas phase infrared spectra of other U^+ or Th^+ complexes need to be measured.

REFERENCES

1. Marks, J. H.; Khan, P.; Vasiliu, M.; Dixon, D. A.; Duncan, M. A. Photodissociation and Theory to Investigate Uranium Oxide Cluster Cations. *J. Phys. Chem. A* **2020**, *124*, 1940–1953.
2. Dau, P. D.; Su, J.; Liu, H.–T.; Huang, D.–L.; Wei, F.; Li, J.; Wang, L.–S. Photoelectron Spectroscopy and Theoretical Studies of UF_5^- and UF_6^-. *J. Chem. Phys.* **2012**, *136*, 194304–9.
3. Li, W.–L.; Su, J.; Jian, T.; Lopez, G. V.; Hu, H.–S.; Cao, G.–J.; Li, J.; Wang, L.–S. Strong Electron Correlation in UO_2^-: A Photoelectron and Relativistic Quantum Chemistry Study. *J. Chem. Phys.* **2014**, *140*, 094306–9.
4. Czekner, J.; Lopez, G. V.; Wang, L.–S. High Resolution Photoelectron Imaging of UO^- and UO_2^- and the Low–Lying Electronic States and Vibrational Frequencies of UO and UO_2. *J. Chem. Phys.* **2014**, *141*, 244302–8.
5. Su, J.; Dau, P. D.; Liu, H.–T.; Huang, D.–L.; Wei, F.; Schwarz, W. H. E.; Li, J.; Wang, L.–S. Photoelectron Spectroscopy and Theoretical Studies of Aqueous Uranium Hexachlorides in Different Oxidation States: UCl_6^{q-} (q = 0–2). *J. Chem. Phys.* **2015**, *142*, 134308–13.

6. Roy, S. K.; Jian, T.; Lopez, G. V.; Li, W.–L.; Su, J.; Bross, D. H.; Peterson, K. A.; Wang, L.–S.; Li. J. A Combined Photoelectron Spectroscopy and Relativistic Ab Initio Studies of the Electronic Structures of UFO and UFO^+. *J. Chem. Phys.* **2016**, *144*, 084309–11.

7. Su, J.; Li, W.–L.; Lopez, G. V.; Jian, T.; Cao, G. J.; Li, W.–L.; Schwarz, W. H. E.; Wang, L.–S.; Li. J. Probing the Electronic Structure and Chemical Bonding of Mono–Uranium Oxides with Different Oxidation States: UO_x^- and UO_x (x = 3–5). *J. Phys. Chem. A* **2016**, *120*, 1084–1096.

8. Han, J.; Kaledin, L. A.; Goncharov, V.; Komissarov, A. V.; Heaven, M. C. Accurate Ionization Potentials of UO and UO_2: A Rigorous Test of Relativistic Quantum Chemistry Calculations. *J. Am. Chem. Soc.* **2003**, *125*, 7176–7177.

9. Han, J.; Goncharov, V.; Kaledin, L. A.; Komissarov, A. V.; Heaven, M. C. Electronic Spectroscopy and Ionization Potential of UO_2 in the Gas Phase. *J. Chem. Phys*. **2004**, *120*, 5155–5163.

10. Goncharov, V.; Han, J.; Kaledin, L. A.; Heaven, M. C. Ionization Energy Measurements and Electronic Spectra for ThO. *J. Chem. Phys*. **2005**, *122*, 204311–6.

11. Gagliardi, L.; Heaven, M. C.; Krogh. J. W.; Roos, B. O. The Electronic Spectrum of the UO_2 Molecule. *J. Am. Chem. Soc.* **2005**, *127*, 86–91.

12. Goncharov, V.; Heaven, M. C. Spectroscopy of the Ground and Low–Lying Excited States of ThO^+. *J. Chem. Phys.* **2006**, *124*, 064312–7.

13. Goncharov, V.; Kaledin, L. A.; Heaven, M. C. Probing the Electronic Structure of UO^+ with High–Resolution Photoelectron Spectroscopy. *J. Chem. Phys.* **2006**, *125*, 133202–8.

14. Heaven, M. C. Probing Actinide Electronic Structure Using Fluorescence and Multiphoton Ionization Spectroscopy. *Phys. Chem. Chem. Phys.* **2006**, *8*, 4497–4509.

15. Merritt. J. M.; Han, J.; Heaven, M. C. Spectroscopy of the UO_2^+ Cation and the Delayed Ionization of UO_2. *J. Chem. Phys.* **2008**, *125*, 084304–8.

16. Barker, B. J.; Antonov, I. O.; Heaven, M. C.; Peterson, K. A. Spectroscopic Investigations of ThF and ThF^+. *J. Chem. Phys.* **2012**, *136*, 104305–9.

17. Heaven, M. C.; Barker, B. J.; Antonov, I. O. Spectroscopy and Structure of the Simplest Actinide Bonds. *J. Phys. Chem. A* **2014**, *118*, 10867–10881.

18. Steimle, T. C.; Zhang, R.; Heaven, M. C.; The Pure Rotational Spectrum of Thorium Monosulfide, ThS. *Chem. Phys. Lett.* **2015**, *639*, 304–306.

19. VanGundy, R. A.; Bartlett. J. H.; Heaven, M. C.; Battey, S. R.; Peterson, K. A. Spectroscopic and Theoretical Studies of ThCl and $ThCl^+$. *J. Chem. Phys.* **2017**, *146*, 054307–8.

20. Battey, S. R.; Bross, D. H.; Peterson, K. A.; Persinger, T. D.; VanGundy, R. A.; Heaven, M. C. Spectroscopic and Theoretical Studies of UN and UN^+. *J. Chem. Phys.* **2020**, *152*, 094302–10.

21. Liu, G.; Zhang, C.; Ciborowski, S. M.; Asthana, A.; Cheng, L.; Bowen, K. H. Mapping the Electronic Structure of the Uranium (VI) Dinitride. *J. Phys. Chem. A* **2020**, *124*, 6486–6492.

22. Groenewold, G. S.; Gianotto, A. K.; Cossel, K. C.; van Stipdonk, M. J.; Moore, D. T.; Polfer, N.; Oomens, J.; de Jong, W. A.; Visscher, L. Vibrational Spectroscopy of Mass–Selected $[UO_2(ligand)_n]^{2+}$ Complexes in the Gas Phase: Comparison with Theory. *J. Am. Chem. Soc.* **2006**, *128*, 4802–4813.

23. Groenewold, G. S.; Oomens, J.; de Jong, W. A.; Gresham, G. L.; McIlwain, M. E.; van Stipdonk, M. J.; Vibrational Spectroscopy of Anionic Nitrate Complexes of UO_2^{2+} and Eu^{3+} Isolated in the Gas Phase. *Phys. Chem. Chem. Phys.* **2008**, *10*, 1192–1202.

24. Groenewold, G. S.; van Stipdonk, M. J.; de Jong, W. A.; Oomens, J.; Gresham, G. L.; McIlwain, M. E.; Gao, D.; Siboulet, B.; Visscher, L.; Kullman, M.; Polfer, N. Infrared Spectroscopy of Dioxouranium(V) Complexes with Solvent Molecules: Effect of Reduction. *ChemPhysChem* **2008**, 9, 1278–1285.

25. Groenewold, G. S.; de Jong, W. A.; Oomens, J.; van Stipdonk, M. J.; Variable Denticity in Carboxylate Binding to the Uranyl Coordination Complexes. *J. Am. Soc. Mass Spectrom.* **2010**, *21*, 719–727.

26. Groenewold, G. S.; van Stipdonk, M.J.; Oomens, J.; de Jong, W. A.; McIlwain, M. E. Vibrational Spectra of Discrete UO_2^{2+} Halide Complexes in the Gas Phase. *Int. J. Mass Spectrom.* **2010**, *297*, 67–75.

27. Groenewold, G. S.; van Stipdonk, M. J.; Oomens, J.; de Jong, W. A.; McIlwain, M. E.; The Gas Phase *Bis*–Uranyl Nitrate Complex $[(UO_2)_2(NO_3)_5]^-$: Infrared Spectrum and Structure. *Int. J. Mass Spectrom.* **2011**, *308*, 175–180.

28. Gibson. J. K.; Hu, H.–S.; van Stipdonk, M. J.; Berden, G.; Oomens, J.; Li. J. Infrared Multiphoton Dissociation of Uranyl and 3–oxa–glutaramide: An Extreme Red–Shift of the $[O=U=O]^{2+}$ Asymmetric Stretch. *J. Phys. Chem. A* **2015**, *119*, 3366–3374.

29. Dau, P. D.; Rios, D.; Gong, Y.; Michelini, M. del C.; Marçalo, J.; Shuh, D. K.; Mogannam, M.; van Stipdonk, M. J.; Corcovilos, T. A.; Martens, J.; Berden, G. Oomens, J.; Redlich, B.; Gibson. J. K. Synthesis and Hydrolysis of Uranyl, Neptunyl, and Plutonyl

Gas–Phase Complexes Exhibiting Discrete Actinide–Carbon Bonds. *Organometallics* **2016**, *35*, 1228–1240.

30. Hu, S.–X.; Gibson. J. K.; Li, W.–L.; van Stipdonk, M. J.; Martens, J.; Berden, G.; Redlich, B.; Oomens, J.; Li. J. Electronic Structure and Characterization of a Uranyl di–15–crown–5 Complex with an Unprecedented Sandwich Structure. *Chem. Comm.* **2016**, *52*, 12761–12764.

31. de Jong, W. A.; Dau, P. D.; Wilson, R. E.; Marçalo, J.; Van Stipdonk, M. J.; Corcovilos, T. A.; Berden, G.; Martens, J.; Oomens, J.; Gibson. J. K. Revealing Disparate Chemistries of Protactinium and Uranium: Synthesis of the Molecular Uranium Tetroxide Anion, UO_4^-. *Inorg. Chem.* **2017**, *56*, 3686–3694.

32. Ricks, A. M.; Gagliardi, L.; Duncan, M. A. Infrared Spectroscopy of Extreme Coordination: The Carbonyls of U^+ and UO_2^+. *J. Am. Chem. Soc.* **2010**, *132*, 15905–15907.

33. Ricks, A. M.; Gagliardi, L.; Duncan, M. A. Oxides and Superoxides of Uranium Detected by IR Spectroscopy in the Gas Phase. *J. Phys. Chem. Lett.* **2011**, *2*,1662–1666.

APPENDIX A

EXAMPLE GAUSSIAN09 CALCULATION OF A URANIUM COMPLEX

An example of a Gaussian16 input file used to efficiently optimize $^{6}U^{+}(N_2)$ is shown below in italics. Notes on the function of each section of code are inserted above without italics. This input file contains five sections separated by "--link1--" which all use the same checkpoint file (*%Chk=U_N2_sextet.chk*), memory (*%mem=7GB*), and number of processors in parallel (*%nprocshared=4*). It is necessary to structure calculations like this to perform the wavefunction stability test, and to speed optimization by initially using a smaller basis set. The first section performs a wavefunction stability test at the B3LYP/cc–pVDZ–PP level. The *#p* keyword is required to include computational timing and SCF convergence data in the log file. The B3LYP functional and the manually input basis are called by *b3lyp/genecp*. The wavefunction stability test, *stable=opt*, must be run without symmetry, *nosymm*. Constrained symmetry imposed on the electronic structure (density matrix) and may lead to spurious results. The keyword line used in increase the integration grid resolution is *integral(grid=superfine,NoXCTest)*. The default integration grid size is inappropriate for most calculations and must be increased to *ultrafine* at a minimum. In the case of actinides, a *superfine* grid is usually appropriate. *NoXCTest* is included to prevent errors during slow SCF or DFT convergence common in actinides. The final keyword line is *scf(maxconventionalcycles=500,xqc,damp,ndamp=200,tight,maxcycles=10000)* which includes several options that aid in convergence on an electronic structure. *maxconventionalcycles=500* increases the number of SCF or DFT iterations before the quadratic convergence algorithm is

implemented by *xqc*. *damp* instructs Gaussian16 to limit changes in the electron density matrix and is on by default but only for the first 10 iterations. Extending this to 200 iterations with *ndamp=200* slows SCF and DFT convergence but reduces numerical error. This likely extends this calculation by a matter of seconds. *tight* SCF and DFT convergence is called for because structural optimization will later also specify *tight* convergence thresholds. *maxcycles=10000* prolongs the calculation in the common case of slow convergence. The *#p, b3lyp/genecp, integral*, and *scf,*keywords remain unchanged in all five sections of this input file. The line reading *insert text* is may be used for notes but cannot be left absent or blank. The charge, multiplicity, atomic numbers and Cartesian coordinates of nuclei are listed below.

%Chk=U_N2_sextet.chk
%mem=7GB
%nprocshared=4
#p b3lyp/genecp stable=opt nosymm integral(grid=superfine,NoXCTest)
scf(maxconventionalcycles=500,xqc,damp,ndamp=200,tight,maxcycles=10000)

insert text

1 6
92 0.000000000 0.000000000 0.000000000
6 3.000000000 0.000000000 0.000000000
6 4.200000000 0.000000000 0.000000000

The basis set input is below. The cc–pVDZ basis is specified for hydrogen and carbon without need to input numerical values. The valence basis set for uranium is copied from a database produced by Hill and coworkers. This repository of relativistic correlation includes the cc–pVnZ–PP basis sets of Peterson which are not available in the EMSL basis set exchange. Below this is the ECP input section. The ECP60MDF parameters and formatting are copied from the database produced by Dolg and coworkers. The 60–electron fully relativistic ECP is preferred for all calculations. It replaces fewer electrons than other available ECPs of similar

accuracy, and the fully relativistic calculation used to produce the parameters of the ECP is more accurate than other methods previously implemented.

H 0
cc–pvdz
*****
C 0
cc–pvdz
*****
U 0
S 14 1.00
3.212010E+04 3.9000000E–05
4.835380E+03 2.8200000E–04
1.107940E+03 1.2580000E–03
3.161190E+02 2.6430000E–03
5.609150E+01 4.0059000E–02
3.510380E+01 –2.4831200E–01
2.198910E+01 6.5642500E–01
1.030160E+01 –1.1390300E+00
2.739410E+00 1.0393670E+00
1.434630E+00 3.7145100E–01
6.106860E–01 4.3863000E–02
2.763810E–01 1.6592000E–02
5.705200E–02 1.7280000E–03
2.334200E–02 5.3800000E–04
S 14 1.00
3.212010E+04 –3.0000000E–05
4.835380E+03 –2.2800000E–04
1.107940E+03 –9.3000000E–04
3.161190E+02 –2.3320000E–03
5.609150E+01 –1.7449000E–02
3.510380E+01 1.1691900E–01
2.198910E+01 –3.4608200E–01
1.030160E+01 6.9333300E–01
2.739410E+00 –1.0201010E+00
1.434630E+00 –3.6711200E–01
6.106860E–01 8.5601400E–01
2.763810E–01 4.7827700E–01
5.705200E–02 1.3394900E–01
2.334200E–02 6.8713000E–02
S 14 1.00
3.212010E+04 1.5000000E–05
4.835380E+03 1.1200000E–04
1.107940E+03 4.5000000E–04
3.161190E+02 1.1550000E–03

5.609150E+01 7.6020000E–03
3.510380E+01 –5.1846000E–02
2.198910E+01 1.5714900E–01
1.030160E+01 –3.2307700E–01
2.739410E+00 5.1106000E–01
1.434630E+00 2.0099400E–01
6.106860E–01 –5.9232700E–01
2.763810E–01 –4.5856800E–01
5.705200E–02 7.4640800E–01
2.334200E–02 4.4966800E–01
S 14 1.00
3.212010E+04 –3.4000000E–05
4.835380E+03 –2.5900000E–04
1.107940E+03 –1.0610000E–03
3.161190E+02 –2.6570000E–03
5.609150E+01 –1.7361000E–02
3.510380E+01 1.1136300E–01
2.198910E+01 –3.3421600E–01
1.030160E+01 7.0871200E–01
2.739410E+00 –1.4845000E+00
1.434630E+00 4.9568000E–02
6.106860E–01 2.7876600E+00
2.763810E–01 –2.1349260E+00
5.705200E–02 –6.7740800E–01
2.334200E–02 1.0971260E+00
S 1 1.00
2.334200E–02 1.0000000E+00
P 13 1.00
4.549280E+02 2.4000000E–04
1.063200E+02 1.2790000E–03
2.584910E+01 –1.8383000E–02
1.616450E+01 1.9759000E–01
1.011100E+01 –4.9023300E–01
6.326010E+00 2.9013000E–02
3.093820E+00 6.7499700E–01
1.633020E+00 4.4001000E–01
7.914730E–01 7.7394000E–02
3.836060E–01 2.1638000E–02
1.778290E–01 9.6910000E–03
5.572800E–02 4.3700000E–04
2.121900E–02 –6.0000000E–06
P 13 1.00
4.549280E+02 –1.5500000E–04
1.063200E+02 –6.9000000E–04
2.584910E+01 6.7870000E–03
1.616450E+01 –1.0183900E–01

1.011100E+01 2.9290300E–01
6.326010E+00 –6.2231000E–02
3.093820E+00 –4.7373800E–01
1.633020E+00 –3.1240300E–01
7.914730E–01 3.6893300E–01
3.836060E–01 6.1737700E–01
1.778290E–01 2.5899200E–01
5.572800E–02 1.8542000E–02
2.121900E–02 –1.6990000E–03
P 13 1.00
4.549280E+02 4.1000000E–05
1.063200E+02 1.6000000E–04
2.584910E+01 –1.2250000E–03
1.616450E+01 2.3619000E–02
1.011100E+01 –7.0784000E–02
6.326010E+00 1.3779000E–02
3.093820E+00 1.2842400E–01
1.633020E+00 7.4143000E–02
7.914730E–01 –1.0889800E–01
3.836060E–01 –2.6085800E–01
1.778290E–01 –6.9155000E–02
5.572800E–02 6.0807000E–01
2.121900E–02 5.1786500E–01
P 13 1.00
4.549280E+02 1.3500000E–04
1.063200E+02 4.0700000E–04
2.584910E+01 –1.5300000E–03
1.616450E+01 6.4934000E–02
1.011100E+01 –2.0720100E–01
6.326010E+00 3.0385000E–02
3.093820E+00 4.4040200E–01
1.633020E+00 2.2929300E–01
7.914730E–01 –6.9741100E–01
3.836060E–01 –4.9874000E–01
1.778290E–01 6.8679700E–01
5.572800E–02 6.3386700E–01
2.121900E–02 –2.4468000E–02
P 1 1.00
2.121900E–02 1.0000000E+00
D 9 1.00
8.282420E+01 1.1800000E–03
1.765580E+01 2.4028000E–02
9.772590E+00 –1.0640700E–01
3.595110E+00 4.0578300E–01
1.873000E+00 5.0382400E–01
9.169040E–01 2.1535100E–01

3.847570E–01 2.2675000E–02
1.497800E–01 –6.2500000E–04
5.412200E–02 2.1200000E–04
D 9 1.00
8.282420E+01 –4.8800000E–04
1.765580E+01 –6.4480000E–03
9.772590E+00 3.1717000E–02
3.595110E+00 –1.5249400E–01
1.873000E+00 –1.7763700E–01
9.169040E–01 5.0268000E–02
3.847570E–01 4.2168600E–01
1.497800E–01 5.1077900E–01
5.412200E–02 2.2820900E–01
D 9 1.00
8.282420E+01 1.1890000E–03
1.765580E+01 8.2190000E–03
9.772590E+00 –5.3112000E–02
3.595110E+00 2.6981500E–01
1.873000E+00 5.5125300E–01
9.169040E–01 –7.3682500E–01
3.847570E–01 –6.2067800E–01
1.497800E–01 6.4165500E–01
5.412200E–02 3.2769500E–01
D 1 1.00
5.412200E–02 1.0000000E+00
F 8 1.00
4.514350E+01 2.7140000E–03
1.550220E+01 1.8290000E–02
5.859440E+00 7.7353000E–02
2.786150E+00 2.7005600E–01
1.341820E+00 3.7709600E–01
6.184540E–01 3.3401600E–01
2.661430E–01 2.0505900E–01
1.009820E–01 6.8957000E–02
F 8 1.00
4.514350E+01 –3.3120000E–03
1.550220E+01 –2.1223000E–02
5.859440E+00 –1.0010900E–01
2.786150E+00 –3.1128000E–01
1.341820E+00 –3.6669700E–01
6.184540E–01 2.2457700E–01
2.661430E–01 5.4064100E–01
1.009820E–01 3.0290800E–01
F 1 1.00
1.009820E–01 1.0000000E+00
G 1 1.00

9.610000E–01 1.0000000E+00
*****

U 0
ECP60MDF 5 60
H–Komponente
1
2 1.00000000 0.00000000
S–H
4
2 16.91870874 529.53526911
2 3.40970576 4.27018845
2 0.79302733 0.09998874
2 0.19378381 0.00626781
P–H
8
2 13.16953414 100.93359134
2 10.60784728 175.95423897
2 2.69049397 –0.00210787
2 2.08929800 –0.19041648
2 0.54050990 0.00494627
2 0.40482776 –0.01652483
2 0.11250285 0.00082033
2 0.09508873 –0.00100028
D–H
8
2 9.06784123 62.85927902
2 8.53362678 90.20882494
2 1.63646790 –0.08282418
2 1.54425719 –0.15307917
2 0.47961552 –0.00008720
2 0.41164502 0.00484078
2 0.13990510 –0.00006136
2 0.17494682 –0.00240839
F–H
8
2 5.14746012 15.68628229
2 5.29241394 22.32105345
2 1.05726701 –0.20689333
2 0.98063114 –0.08434451
2 0.48259555 0.06084446
2 0.55434882 0.00231264
2 0.23674544 –0.00204069
2 0.21559852 0.00348388
G–H
6

2 18.83643086 –44.41029420
2 18.74850924 –53.65339478
2 6.49279545 –2.55219343
2 6.57472519 –3.34380088
2 2.58151924 0.04527524
2 2.58690949 0.05637947

This is the second input section which instructs Gaussian16 to optimize the geometry of $U^{+}(N_2)$ at the B3LYP/cc–pVDZ–PP level. The *nosymm* and *stable=opt* commands are removed and *opt(maxcyc=1000)* is included. This allows the geometry optimization to continue not up to 1000 iterations, but to an internal maximum calculated by Gaussian16. The *guess=read*, *genchk* and *geom=allcheck* keywords call for the electronic structure, basis set and ecp, and geometry, respectively, from the checkpoint file.

—link1—
%Chk=U_N2_sextet.chk
%mem=7GB
%nprocshared=4
#p b3lyp/genecp opt(maxcyc=1000) integral(grid=superfine,NoXCTest)
scf(maxconventionalcycles=500,xqc,damp,ndamp=200,tight) guess=read genchk
geom=allcheck

This third section includes the *pop(full,nbo)* keyword which commands Gaussian 16 to perform a natural bond orbital (NBO) calculation. *full* indicates that the NBO analysis should include printed output from all orbitals and include data necessary to render images of molecular orbitals. The *gfinput* keyword results in the basis set being printed in the log file which is necessary to produce imaged of molecular orbitals. The NBO output also includes useful data such as the electron configuration, natural charge, natural spin, and covalency of each atom.

—link1—
%Chk=U_N2_sextet.chk
%mem=7GB
%nprocshared=4
#p b3lyp/genecp pop(full,nbo) gfinput integral(grid=superfine,NoXCTest)
scf(maxconventionalcycles=500,xqc,damp,ndamp=200,tight) guess=read genchk
geom=allcheck

The fourth section performs a second wavefunction stability analysis, but uses the previously optimized geometry and electronic state as a starting point. Large changes in geometry can result from optimization of guesses at the structure of a molecule. It is necessary to perform the wavefunction stability test after large geometry changes because there may be an accompanying change in electronic structure. This second stability test is performed with a larger basis set, cc–pVTZ–PP, to produce more accurate final results. The use of *guess=read* and *geom=allcheck* replaces the notes, charge, multiplicity, and geometry input sections. The basis set values for uranium have been replaced with the appropriate triple zeta values, but the ECP is the same.

—link1—
%Chk=U_N2_sextet.chk
%mem=7GB
%nprocshared=4
#p b3lyp/genecp nosymm stable=opt integral(grid=superfine,NoXCTest)
scf(maxconventionalcycles=500,xqc,damp,ndamp=200,tight,maxcycles=10000)
guess=read geom=allcheck

H 0
cc–pvtz
******
C 0
cc–pvtz
******
U 0
S 17 1.00
3.616890E+04 3.4000000E–05
5.356190E+03 2.5400000E–04
1.200140E+03 1.1660000E–03
3.279790E+02 2.8030000E–03
5.360230E+01 4.1117000E–02
3.350810E+01 –2.8217500E–01
2.095960E+01 8.8255400E–01
1.311150E+01 –7.8322900E–01
8.199450E+00 –6.2706700E–01
3.147330E+00 8.3919400E–01
1.817930E+00 5.6194800E–01

1.051480E+00 1.0237400E–01
5.048720E–01 3.4399000E–02
2.476910E–01 1.1568000E–02
7.653400E–02 1.4140000E–03
3.885000E–02 9.3000000E–04
1.843300E–02 4.8800000E–04
S 17 1.00
3.616890E+04 –2.6000000E–05
5.356190E+03 –2.0200000E–04
1.200140E+03 –8.9800000E–04
3.279790E+02 –2.3210000E–03
5.360230E+01 –2.2696000E–02
3.350810E+01 1.5505800E–01
2.095960E+01 –5.1725100E–01
1.311150E+01 5.2328700E–01
8.199450E+00 3.4592600E–01
3.147330E+00 –6.9974300E–01
1.817930E+00 –7.6672900E–01
1.051480E+00 2.3752700E–01
5.048720E–01 8.1309000E–01
2.476910E–01 3.1403300E–01
7.653400E–02 7.9023000E–02
3.885000E–02 1.0143700E–01
1.843300E–02 3.8387000E–02
S 17 1.00
3.616890E+04 1.3000000E–05
5.356190E+03 1.0100000E–04
1.200140E+03 4.4600000E–04
3.279790E+02 1.1670000E–03
5.360230E+01 1.0554000E–02
3.350810E+01 –7.2022000E–02
2.095960E+01 2.4308300E–01
1.311150E+01 –2.4965400E–01
8.199450E+00 –1.6519200E–01
3.147330E+00 3.5630000E–01
1.817930E+00 4.0770900E–01
1.051480E+00 –1.4490300E–01
5.048720E–01 –5.9395200E–01
2.476910E–01 –3.7252900E–01
7.653400E–02 3.8149500E–01
3.885000E–02 6.2074900E–01
1.843300E–02 2.2238400E–01
S 17 1.00
3.616890E+04 2.9000000E–05
5.356190E+03 2.2700000E–04
1.200140E+03 1.0010000E–03

3.279790E+02 2.6360000E–03
5.360230E+01 2.2035000E–02
3.350810E+01 –1.4747100E–01
2.095960E+01 5.0456500E–01
1.311150E+01 –5.4559600E–01
8.199450E+00 –3.1829000E–01
3.147330E+00 8.6033000E–01
1.817930E+00 1.2544620E+00
1.051480E+00 –1.6201240E+00
5.048720E–01 –1.5474120E+00
2.476910E–01 1.7222350E+00
7.653400E–02 1.0623700E+00
3.885000E–02 –9.5939700E–01
1.843300E–02 –3.7543100E–01
S 17 1.00
3.616890E+04 –4.4000000E–05
5.356190E+03 –3.3500000E–04
1.200140E+03 –1.5270000E–03
3.279790E+02 –3.8020000E–03
5.360230E+01 –3.8822000E–02
3.350810E+01 2.4222100E–01
2.095960E+01 –8.0587300E–01
1.311150E+01 9.7326400E–01
8.199450E+00 2.3758700E–01
3.147330E+00 –1.2238870E+00
1.817930E+00 –2.5904180E+00
1.051480E+00 5.7694510E+00
5.048720E–01 –2.4366040E+00
2.476910E–01 –1.5661670E+00
7.653400E–02 2.9085710E+00
3.885000E–02 –1.1697730E+00
1.843300E–02 –5.9743300E–01
S 1 1.00
1.843300E–02 1.0000000E+00
P 16 1.00
1.075000E+03 6.6000000E–05
2.486820E+02 4.3500000E–04
7.146260E+01 1.8520000E–03
2.677310E+01 –2.4209000E–02
1.673900E+01 1.9615700E–01
1.046780E+01 –4.2791900E–01
6.546410E+00 –7.6839000E–02
3.469440E+00 5.6237200E–01
1.947820E+00 5.1492200E–01
1.060150E+00 1.4650000E–01
5.558950E–01 2.8086000E–02

2.907100E–01 1.7113000E–02
1.492260E–01 4.5670000E–03
7.222100E–02 6.2500000E–04
3.418900E–02 –1.6000000E–05
1.558900E–02 1.7000000E–05
P 16 1.00
1.075000E+03 –3.7000000E–05
2.486820E+02 –2.8700000E–04
7.146260E+01 –9.2000000E–04
2.677310E+01 1.0431000E–02
1.673900E+01 –1.0419900E–01
1.046780E+01 2.6332900E–01
6.546410E+00 –3.4920000E–03
3.469440E+00 –3.7805300E–01
1.947820E+00 –4.0371000E–01
1.060150E+00 9.5407000E–02
5.558950E–01 5.2492500E–01
2.907100E–01 4.5008200E–01
1.492260E–01 1.4095400E–01
7.222100E–02 1.4852000E–02
3.418900E–02 1.6140000E–03
1.558900E–02 1.2000000E–05
P 16 1.00
1.075000E+03 9.0000000E–06
2.486820E+02 7.3000000E–05
7.146260E+01 2.2300000E–04
2.677310E+01 –2.4360000E–03
1.673900E+01 2.5549000E–02
1.046780E+01 –6.6316000E–02
6.546410E+00 2.8050000E–03
3.469440E+00 9.7253000E–02
1.947820E+00 1.0826100E–01
1.060150E+00 –3.7564000E–02
5.558950E–01 –1.7543900E–01
2.907100E–01 –2.0046600E–01
1.492260E–01 –4.1542000E–02
7.222100E–02 3.3476400E–01
3.418900E–02 5.7774500E–01
1.558900E–02 2.3752800E–01
P 16 1.00
1.075000E+03 3.0000000E–05
2.486820E+02 2.1800000E–04
7.146260E+01 7.9200000E–04
2.677310E+01 –9.0480000E–03
1.673900E+01 8.7386000E–02
1.046780E+01 –2.3034800E–01

6.546410E+00 4.1458000E–02
3.469440E+00 2.7483400E–01
1.947820E+00 4.6495700E–01
1.060150E+00 –4.0386700E–01
5.558950E–01 –7.1416900E–01
2.907100E–01 1.8213000E–02
1.492260E–01 4.8091000E–01
7.222100E–02 5.3233500E–01
3.418900E–02 1.0792500E–01
1.558900E–02 4.7870000E–03
P 16 1.00
1.075000E+03 –4.9000000E–05
2.486820E+02 –3.5800000E–04
7.146260E+01 –1.2380000E–03
2.677310E+01 1.4325000E–02
1.673900E+01 –1.4469200E–01
1.046780E+01 4.0168300E–01
6.546410E+00 –1.2170700E–01
3.469440E+00 –4.4915100E–01
1.947820E+00 –9.0042300E–01
1.060150E+00 1.5187770E+00
5.558950E–01 7.5757500E–01
2.907100E–01 –1.6040800E+00
1.492260E–01 –3.2845900E–01
7.222100E–02 8.4877900E–01
3.418900E–02 2.3592800E–01
1.558900E–02 5.1270000E–03
P 1 1.00
1.558900E–02 1.0000000E+00
D 11 1.00
1.982880E+02 2.3000000E–04
5.942420E+01 1.4760000E–03
1.621310E+01 2.9669000E–02
9.805410E+00 –1.1645900E–01
3.793560E+00 3.3957200E–01
2.111500E+00 4.7821600E–01
1.122010E+00 2.7211200E–01
5.600260E–01 5.8394000E–02
2.487660E–01 2.7160000E–03
1.049670E–01 1.7700000E–04
4.197000E–02 –7.4000000E–05
D 11 1.00
1.982880E+02 –6.1000000E–05
5.942420E+01 –6.3400000E–04
1.621310E+01 –8.1600000E–03
9.805410E+00 3.5449000E–02

3.793560E+00 –1.3086400E–01
2.111500E+00 –1.6495800E–01
1.122010E+00 –4.6287000E–02
5.600260E–01 2.4787700E–01
2.487660E–01 4.6031300E–01
1.049670E–01 3.8812000E–01
4.197000E–02 1.2798300E–01
D 11 1.00
1.982880E+02 –6.3000000E–05
5.942420E+01 –1.5140000E–03
1.621310E+01 –1.2458000E–02
9.805410E+00 6.3777000E–02
3.793560E+00 –2.3965000E–01
2.111500E+00 –4.5388900E–01
1.122010E+00 1.7052000E–01
5.600260E–01 9.5959200E–01
2.487660E–01 –1.2978100E–01
1.049670E–01 –5.7636000E–01
4.197000E–02 –1.7395500E–01
D 11 1.00
1.982880E+02 –1.0200000E–04
5.942420E+01 3.0750000E–03
1.621310E+01 3.2190000E–03
9.805410E+00 –6.1916000E–02
3.793560E+00 3.0476900E–01
2.111500E+00 9.3474900E–01
1.122010E+00 –1.7196620E+00
5.600260E–01 1.8429000E–01
2.487660E–01 1.2268660E+00
1.049670E–01 –7.1835800E–01
4.197000E–02 –2.6669600E–01
D 1 1.00
4.197000E–02 1.0000000E+00
F 10 1.00
1.532310E+02 1.6000000E–04
4.507950E+01 2.2620000E–03
1.777060E+01 1.2978000E–02
7.686250E+00 4.1634000E–02
3.592430E+00 1.8472900E–01
1.850530E+00 3.2161200E–01
9.300490E–01 3.4063900E–01
4.469020E–01 2.6385600E–01
2.013310E–01 1.4476300E–01
8.087300E–02 4.2347000E–02
F 10 1.00
1.532310E+02 –1.6000000E–04

4.507950E+01 –2.9620000E–03
1.777060E+01 –1.4234000E–02
7.686250E+00 –5.5943000E–02
3.592430E+00 –2.1728400E–01
1.850530E+00 –3.7186400E–01
9.300490E–01 –1.3045200E–01
4.469020E–01 4.0708600E–01
2.013310E–01 4.5062700E–01
8.087300E–02 2.0063800E–01
F 10 1.00
1.532310E+02 –2.2000000E–04
4.507950E+01 –3.6980000E–03
1.777060E+01 –1.8660000E–02
7.686250E+00 –6.7935000E–02
3.592430E+00 –3.2452500E–01
1.850530E+00 –5.5503100E–01
9.300490E–01 8.4790900E–01
4.469020E–01 3.5909700E–01
2.013310E–01 –5.3815300E–01
8.087300E–02 –3.2024900E–01
F 1 1.00
8.087300E–02 1.0000000E+00
G 1 1.00
2.558900E+00 1.0000000E+00
G 1 1.00
8.106000E–01 1.0000000E+00
G 1 1.00
1.999000E–01 1.0000000E+00
H 1 1.00
1.104200E+00 1.0000000E+00
******

U 0
ECP60MDF 5 60
H–Komponente
1
2 1.00000000 0.00000000
S–H
4
2 16.91870874 529.53526911
2 3.40970576 4.27018845
2 0.79302733 0.09998874
2 0.19378381 0.00626781
P–H
8
2 13.16953414 100.93359134

2 10.60784728 175.95423897
2 2.69049397 –0.00210787
2 2.08929800 –0.19041648
2 0.54050990 0.00494627
2 0.40482776 –0.01652483
2 0.11250285 0.00082033
2 0.09508873 –0.00100028
D–H
8
2 9.06784123 62.85927902
2 8.53362678 90.20882494
2 1.63646790 –0.08282418
2 1.54425719 –0.15307917
2 0.47961552 –0.00008720
2 0.41164502 0.00484078
2 0.13990510 –0.00006136
2 0.17494682 –0.00240839
F–H
8
2 5.14746012 15.68628229
2 5.29241394 22.32105345
2 1.05726701 –0.20689333
2 0.98063114 –0.08434451
2 0.48259555 0.06084446
2 0.55434882 0.00231264
2 0.23674544 –0.00204069
2 0.21559852 0.00348388
G–H
6
2 18.83643086 –44.41029420
2 18.74850924 –53.65339478
2 6.49279545 –2.55219343
2 6.57472519 –3.34380088
2 2.58151924 0.04527524
2 2.58690949 0.05637947

This fifth and final section is similar to the second with substitution of the double zeta basis set with one of triple zeta quality. The electronic state, Cartesian coordinates, and basis set are loaded from the checkpoint file. The structure of the molecule is optimized with o*pt(maxcyc=1000,tight)* to *tight* convergence thresholds. After the structure is optimized a vibrational analysis is performed by *freq*.

—link1—
%Chk=U_N2_sextet.chk
%mem=7GB
%nprocshared=4
#p b3lyp/genecp opt(maxcyc=1000,tight) freq integral(grid=superfine,NoXCTest) scf(maxconventionalcycles=500,xqc,damp,ndamp=200,tight) guess=read genchk geom=allcheck

This input file cannot produce a final structure or vibrational frequencies in the log file if the molecule has failed the wavefunction stability test with either the double or triple zeta quality basis seta. The *stable=opt* job automatically corrects any error identified. However, this calculation tends to identify fewer error in larger molecules. It is not clear if this is a result of such errors becoming less likely to occur in larger molecules, or are present but are less likely to be identified. Furthermore, the wavefunction stability test is only as accurate as the method in which it is implemented.

The many keywords used throughout this input file to control convergence are effective at producing optimized ground electronic states. However, there are several reasons a calculation may fail. Large changes in geometry such as a change in symmetry commonly cause errors. The internal coordinate system employed by Gaussian16 cannot represent a non–linear molecule as it approaches a linear structure. If any three atoms approach linearity the error will cause the calculation to cease. Imaginary or negative frequencies are not common but if they are predicted the molecule is manually deformed along the imaginary coordinate and the calculation is restarted. It is also common for calculation including actinides to require longer than the provided time, and they may need to be restarted. Regardless of the cause, calculations are restarted with the newest Cartesian coordinates, and the keyword *guess=read* added to the first section. If an electronic structure has already been produced this keyword will load it from the

checkpoint file. This saves a substantial amount of time spent reproducing earlier work when calculations need to be restarted.